Advancing Human Lower-limb Kinematic Estimation Using Inertial Measurement Units

by

Michael V. Potter

A dissertation submitted in partial fulfillment
of the requirements for the degree of
Doctor of Philosophy
(Mechanical Engineering)
in The University of Michigan
2021

Doctoral Committee:

Associate Research Scientist Lauro V. Ojeda, Co-Chair
Professor Noel C. Perkins, Co-Chair
Research Professor James A. Ashton-Miller
Assistant Research Scientist Stephen M. Cain
Professor Jessy W. Grizzle

Michael V. Potter

mvpotter@umich.edu

OCID iD: 0000-0002-3793-5657

Acknowledgements

This dissertation has been shaped by many people in many ways. In including acknowledgements, I fear both leaving people out and my weakness in adequately describing my gratitude for those I include in text. However, I will do my best and I hope that my weaknesses in both these regards will be forgiven. I am truly grateful for all you have done.

I want to start by thanking my co-advisor, Noel Perkins. His caring guidance and support for my professional development throughout this process has been an immense blessing. I appreciate his continued patience in developing my research and communication skills. Beyond professional development, he has shown great kindness and thoughtfulness towards me and my family. Thank you.

I also want to thank my other co-advisor, Lauro Ojeda for his continued support. I have greatly benefited from his guidance and experience with IMUs and particularly foot IMU methods.

Thank you to Stephen Cain for his immense mentorship throughout my time at Michigan. I have greatly benefited from many conversations about IMUs, biomechanics, and many more professional and personal topics.

Thank you to Professor James Ashton-Miller for his guidance relating to biomechanics, and particularly soft tissue effects.

Thank you to Professor Jessy Grizzle for his Math for Robotics class and his additional guidance relating to estimation methods.

Beyond my doctoral committee, thank you to my long-time office mate Rachel Vitali. I benefited in many ways from her experience with IMUs and navigating the Department of Mechanical Engineering. I also appreciate the many (often long) discussions we had about IMU methods, professional development, and life.

Thank you to Professor Maani Ghaffari for his insightful Mobile Robotics class and for introducing me to the error-state Kalman filter which I incorporate as the fundamental framework for the seven-body method developed in this dissertation.

Thank you to Professor Leia Stirling for her support in my career development and her frequent feedback and insights that helped shape my work.

I also want to thank my many other colleagues whose efforts, insights, and expertise have supported various aspects of my work including Alyssa Mendoza, Steven Davidson, and Antonia Zaferiou.

I also want to acknowledge the National Science Foundation Graduate Research Fellowship Program, the U.S. Army's CCDC Soldier Center, and the University of Michigan Department of Mechanical Engineering for their tremendous financial support of various aspects of this work. I am extremely grateful.

Below, I want to highlight some individuals who deserve recognition for their contributions with specific aspects of each of my studies.

Chapter 2: I thank all my coauthors on the resulting publication (Lauro Ojeda, Noel Perkins, and Stephen Cain) for their guidance on the methodology and analysis of this work. Stephen also gave additional help in conducting the experiments and collecting data for this study. I also want to thank Corey Powell for his significant help and insights on the statistical analyses presented in this chapter. Finally, thanks is also to due to our study participants.

Chapter 3: Thank you to Professor Ryan McGinnis and his M-Sense Research group at the University of Vermont for their guidance on the experimental design and for offering their motion capture laboratory to conduct the experimental parts of this chapter. A special thanks also goes to his student, Reed Gurchiek, for his additional guidance on optical motion capture and for helping me collect the experimental data.

Chapter 4: Another big thank you is deserved for Professor Ryan McGinnis and his research group for conducting the experimental study, labeling all motion capture files, and offering use of their data set for validating the error-state Kalman filter method in this chapter.

I also recognize that my professional development started long before my PhD program. Thank you to the many teachers, professors, coaches, managers, mentors, leaders, etc. who have influenced me throughout my life.

I also could not have completed this dissertation without support from many outside the workplace. Thank you to my church family, gaming friends, ONU cross country team family, fellow soccer referees, Saturday morning basketball group, fellow Rackham Student Government representatives, and other friends for all the support, memories, and fun.

I also want to thank my family for their continued support of me in my goals. I wish I could thank all my extended family individually for their various support. I have been truly blessed with parents who have loved, supported, and sacrificed for me in all areas of my life. I am also grateful for the support of my siblings, two of which followed me to Michigan. Particular thanks to Brianna for all her support while living with me here and to Hannah for many meaningful chats over shared meals. I also thank my wife's family for their continued support of my family and my career goals.

Importantly, I thank my wife and kids. Thank you for your support and your sacrifices throughout this process.

Finally, thanks be to my God and my Savior, to whom I owe all that I have, am, and can be.

Table of Contents

List of Tables

List of Figures

List of Appendices

Abstract

The study of human biomechanics has broad applications in human health, worker safety, warfighter performance, athlete performance, injury prevention, and related fields. Historically, research in all of these fields is frequently limited by measurements of human kinematics being restricted to laboratory environments. Wearable sensors, in the form of body-worn inertial measurement units (IMUs), show great promise in extending the validity of research conclusions by enabling measurements in non-laboratory environments such as the workplace, home, clinic, and training facility. However, to accurately estimate human kinematics from body-worn IMUs, advancements must be made in signal processing methods to correct integration drift errors caused by the integration of noisy sensor data. This dissertation addresses this need by contributing a novel error-state Kalman filter (ErKF) method for estimating the kinematics of the human lower limbs in broad contexts. The lower limbs are chosen due to their paramount importance in the applications articulated above. This research achievement follows the systematic progression of three studies that advance IMU-based kinematic estimation for: 1) a single foot-mounted IMU, 2) an array of three body-worn IMUs in a mechanical "walker" (an approximation to the human lower limbs), and 3) an array of seven body-worn IMUs in a full representation of the human lower limbs. The major findings and contributions of each study are summarized below.

The first study lays a critical foundation for the full lower-limb model by exploring the limiting case of deploying a single foot-mounted IMU to estimate foot trajectories. This study contributes criteria for selecting IMU sensor hardware to achieve accurate estimates of stride parameters (e.g., stride length, stride angle) and reveals that prior zero-velocity drift corrections developed for normal walking remain applicable for highly dynamic gaits, including fast walking and running.

The second study builds from the first by considering three IMUs attached to the three segments of a mechanical “walker” (composed of a pelvis and two straight legs) which serves as an approximation to the human lower limbs. The study contributes a novel ErKF method to estimate the kinematics of the coupled, three-body walker model. Importantly, the method uses kinematic constraints to reduce integration drift errors without reliance on magnetometers or common assumptions (e.g., level-ground). The method successfully estimates the kinematics of a mechanical walker which replicate closely those obtained via simulation and experimental motion capture (MOCAP). For instance, the (hip) joint angles achieve RMS differences below 1.5 degrees compared to MOCAP.

The success of the ErKF method on the three-body walker model motivates its extension to a full, seven-body model of the human lower limbs in the third study. This study contributes novel joint axis corrections within the ErKF for the hip and knee to reduce joint angle drift errors and to account for the additional complexities of human anatomy (e.g., soft tissue, biological joints). The resulting full model is evaluated on human subjects performing six different types of gait and compared to results from MOCAP. This comparison reveals RMS differences in joint angle estimates generally below 5 degrees when compared to MOCAP employing reflective markers attached to the IMUs. Similarly, small differences in the estimated joint angle ranges of motion, stride length, and step width confirm the significant promise of this novel ErKF method as a research strategy for non-laboratory based biomechanical studies of the human lower limbs and in broad contexts.

Chapter 1

Introduction

1.1 Background and Motivation

The study of human biomechanics has broad applications including in human health, worker safety, warfighter performance, athlete performance, and injury prevention. Much of the research in these contexts considers measuring and analyzing human dynamics during tasks restricted to the laboratory. A major disadvantage of lab-based biomechanical analyses is the limited capture volumes associated with such spaces. Another disadvantage is that humans may perform tasks differently in laboratory environments than in natural settings. For example, multiple studies demonstrate that even for a task as simple as walking, certain gait metrics differ between treadmill versus overground walking [1, 2]. Additionally, laboratory-based analyses do not allow for continual monitoring of humans to support, for example, fall risk detection in the elderly [3, 4], worker safety [5], and athlete performance [6]. These limitations provide strong motivation to monitor human motion outside of laboratory environments using wearable sensors [7].

With advances in microelectromechanical system (MEMS) technology, miniature inertial measurement units (IMUs) are increasingly becoming an attractive option as a wearable sensor for measuring human movement both inside and outside traditional laboratory environments. These IMUs typically contain at a minimum three-axis accelerometers and angular rate gyroscopes, but in some designs also include magnetometers, barometers, and global positioning systems (GPS), among other sensors. For measuring human movement, inertial motion capture offers many advantages over traditional types of motion capture like optical marker-based motion capture (MOCAP) including the relative low cost, portability to any environment, ease of setup and use, and unlimited capture volume [8].

When comparing IMU to MOCAP measures, it is important to recognize that these two technologies measure different (though related) kinematical variables for describing human movement as shown in Figure 1.1. In particular, traditional MOCAP has a strength in measuring positions of markers, from which segment orientations (and thus joint angles) may also be estimated. Subsequent analyses of velocities and accelerations (both linear and angular) requires differentiation starting from the original positional data. In contrast, IMUs directly measure linear accelerations and angular velocities and thus have a strength in measuring those kinematical variables. Estimating positions from IMU data requires integration. Specifically, angular rate data is integrated to obtain estimates of orientations in a lab-fixed frame. These orientations are required to resolve sensor-fixed acceleration data from the IMU into the lab-fixed frame before integrating once for linear velocity and twice for position. If IMUs were noiseless, this integration would cause no errors in the calculated position of the IMU. However, state-of-the-art MEMS-based IMUs (suitable for biomechanics studies) possess noisy signals and integration of these noisy signals creates unavoidable integration drift errors [9].

Note that even error-less IMU position data would not directly yield perfect kinematic estimates of the bone positions and orientations. Accurate kinematic estimates based on IMU positions and orientations critically rely on accurate sensor to (body) segment calibration (i.e., determination of the relative location and orientation of the corresponding sensor and anatomical frames) which is a challenging problem itself. Additionally, soft tissue movement yields relative motion between IMUs and underlying bones which results

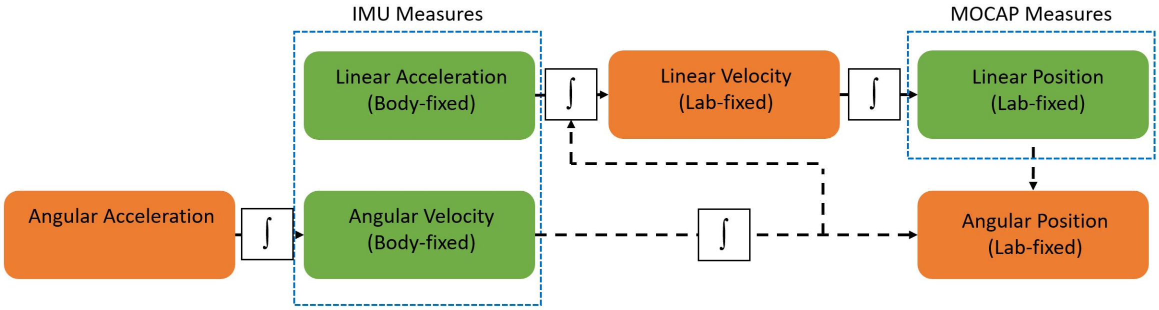

Figure 1.1: Relationship between kinematic data obtained from IMU versus MOCAP. Integrations required to relate body-fixed IMU data to lab-fixed MOCAP data and derivatives required for the opposite relations. Green indicates measured quantities while orange indicates quantities estimated from those measures.

in non-constant sensor to segment alignment parameters. Thus, errors in bone kinematic estimates from perfect IMU data may still arise from errors in sensor to segment calibration and soft tissue artefacts. However, traditional marker-based MOCAP suffers from the same type of errors due to precision limits in the placement of markers on bony landmarks and relative movements between markers and bone [10, 11]. Markerless motion capture methods which mitigate these errors include stereo radiography [12, 13], real-time MRI [14], and markerless video motion capture [15]. However, these methods also suffer obvious disadvantages with laboratory-restricted testing.

Because of the differing strengths in IMU versus MOCAP measures above, there are two broad approaches to using IMUs for biomechanical analyses. One approach is to develop methods for traditional biomechanical metrics using IMUs. Because much of the work historically in biomechanics has relied on MOCAP methods, many of the traditional metrics relate to linear and angular positions (i.e., the strengths of MOCAP). Unfortunately, replicating these positional metrics starting with IMU measures (acceleration and angular rate) requires significant attention to reduce the aforementioned integration drift errors. Despite this challenge, this first approach remains valuable because traditional metrics leverage the wealth of historical work in biomechanics. While there has been significant progress towards replicating traditional metrics from IMU data (see, for example [11, 16]), there remain both challenges and opportunities to advance this approach as detailed in subsequent chapters. A second approach showing great promise is to develop and use non-traditional biomechanical metrics based on the measurement strengths of IMUs (e.g., closer to the IMU measures in Fig. 1.1); see, for example [17]. This second approach capitalizes on the strengths of IMU technology. While this dissertation primarily focuses on the former approach, it may also support the development of non-traditional metrics once we successfully replicate traditional metrics; thus, we recognize that these approaches are synergistic.

1.2 Research Objective and Scope

The primary objective of this dissertation is to estimate the lower-limb kinematics of human subjects using arrays of wearable inertial sensors. We focus on the lower-limb kinematics, especially joint angles and stride parameters, because they are critical for understanding a wide range of tasks including clinical gait analysis[18], running[19, 20], fall risk in the elderly[21], and prosthetic design[22], to name a few. Accomplishing this research objective involves understanding state-of-the-art methods, noting their limitations, and then developing new methods that advance the state-of-the-art. The research objective is achieved by completing three primary tasks; namely, 1) understanding the sensor hardware requirements needed to obtain accurate kinematic estimates of the lower limbs and the applicability of zero-velocity drift corrections for dynamic movement, 2) developing and validating methods for estimating kinematics on a simplified (three-body) lower-limb model (i.e., reduced body segments and degrees of freedom), and 3) developing and validating methods for estimating kinematics for a complete (seven-body) human lower-limb model (using an array of seven IMUs). Synopses of these studies are provided next which also provide an outline for the remainder of this dissertation.

1.2.1 Chapter 2: Effect of IMU Design on IMU-Derived Stride Metrics for Running

To understand the sensor requirements needed to obtain accurate kinematic estimates of the lower limbs, we focus on the task of running because it involves significant dynamics of the lower-limb segments relative to other types of human locomotion. Furthermore, during running, the feet experience the greatest range of dynamical states. Consequently, by focusing on kinematic estimates of the feet during running, one can reveal key challenges for IMU hardware and the associated computational algorithms.

State-of-the-art methods for estimating foot kinematics with shoe-worn IMUs primarily rely on variations of an approach known as the zero-velocity update point (ZUPT) method [8, 23–27]. This method takes advantage of the fact that, during human locomotion, the foot achieves nearly zero-velocity during some point of the stance phase, and uses that zero velocity to correct for integration drift errors in velocity and positional estimates. While this method has been well-validated for walking and for running at slow speeds, it had not been previously validated for faster running speeds such as those observed in elite distance running and sprinting.

The purpose of this first study is to test the limits of what can be achieved with state-of-the-art estimation methods and to understand the sensor hardware requirements that are necessary for accurate kinematic estimation. The ZUPT method is a strong candidate for this purpose because the feet are important starting points for the lower-limb kinematic chain and because the IMU data at the feet are particularly susceptible to hardware limitations including saturation during impact and high frequency content. Thus, this first study has two primary aims: 1) to determine if the ZUPT method remains accurate at higher running speeds (e.g., elite middle-distance running), and 2) to determine the sensor hardware requirements necessary for accurate estimates of foot kinematics. Results demonstrate that the ZUPT method is indeed well-suited for the aforementioned applications provided the IMU hardware is judiciously selected. Additionally, we show that foot position and velocity estimates are negatively impacted by inappropriate IMU hardware selection. In particular, the accuracy of estimated stride metrics generally degrades with increased speed, decreased accelerometer range, decreased gyro range, and decreased sampling rate. Additionally, we identify the root causes of inaccurate stride estimates using the ZUPT method and provide important engineering considerations and recommendations for proper hardware selection to achieve accurate kinematic estimates. The contents of this chapter are also published in [28].

1.2.2 Chapter 3: Error-state Kalman Filter for Lower-limb Kinematic Estimation: Evaluation on a Three-body Model

The second task, focuses on transitioning from methods that rely on a single IMU (as in the first study) to those using an array of IMUs across multiple body segments. We begin with a simplified lower-limb model with reduced body segments and degrees of freedom. We consider a mechanical three-body ”walker” with a pelvis and two legs (made from PVC pipe) connected with pure hinge joints. This simplified lower-limb model allows us to gradually build up the complexity of the lower-limb model and to isolate core challenges in the process. This chapter contributes a novel error-state Kalman filter (ErKF) [29, 30] method to estimate the states of the three lower-limb segments. In this formulation, drift errors are corrected through measurement updates to the estimated state within the ErKF framework including leveraging kinematic constraints of the lower-limb system. In particular, these constraints include zero-velocity updates for the ”feet” and joint center location and axes constraints for the two ”hip” joints.

As highlighted in the first study, real hardware often creates challenges in realizing accurate kinematic estimates even if the estimation methods themselves are sound. Thus, we first address the quality of the new ErKF estimation method in the presence of ”ideal” sensor data (i.e., well-described noise parameters and biases) prior to using this method with real sensor data. To first address the quality of the method using ”ideal” IMU data, the multi-body dynamics software OpenSim [31, 32] is used to simulate the walker and to generate noise-free and bias-free simulated IMU data. We then add controlled noise and biases to the simulated IMU data to validate the new estimation method. Doing so enables us to establish the effects produced by hardware (noise and bias) limitations. The results of this study reveal that this new ErKF method accurately estimates joint angles and stride metrics in the presence of "ideal" IMU data.

Second, we collect experimental IMU data while walking the mechanical walker in a MOCAP environment and compare the kinematic estimates arising from the estimation method versus those obtained from MOCAP. The results reveal only small differences between ErKF and MOCAP estimates of joint angles and stride metrics in the presence of real IMU data when the kinematic constraints (i.e., joint center locations, joint axes, and IMU still times) are well-characterized.

Finally, we collect experimental data for a human attempting to walk with stiff legs (approximation to three-body model). Low RMS differences between ErKF and MOCAP estimates of stride length and step width suggest great promise in extending the ErKF method to a full seven-body model of the human lower limbs. The contents of this chapter have been submitted for journal publication.

1.2.3 Chapter 4: Evaluation of Error-state Kalman Filter Method for Estimating Human Lower-limb Kinematics during Various Walking Gaits

Extending from the second study, the third study tackles kinematic estimation on a full human lower-limb model composed of seven segments (pelvis, two thighs, two shanks, two feet) with an IMU attached to each segment. While the previous study (Ch. 3) validates the method that utilizes kinematic constraints to correct for errors, the present study (Ch. 4) extends this method to a human body which requires careful application of the kinematic constraints (via the measurement model) due to the complexity of human joints and soft tissue. For example, for the walker examined in Ch. 3, both ”hip” joints always act as hinges, which is leveraged to correct for errors in the state estimates. In contrast, the human hip and knee are not purely hinge joints and thus this kinematic constraint cannot be strictly employed at all times. However, recognizing that healthy joints are limited in their range of motion, a method is proposed in the form of ”soft” joint axis constraints that recognizes these limitations for the hip and knee while still allowing three degree of freedom angular rotation.

Additionally, for the method to be applicable across a wide variety of biomechanical contexts (e.g., where abnormal gait develops due to injury or disease), the method must be validated against a variety of gait types that exercise various degrees of freedom of the joints. To this end, the seven-body method is validated on twenty human subjects walking with six different types of gait comprising forward walking at three speeds, backward walking, and lateral walking (to both left and right). Estimated joint angles, ranges of motion, stride length, and step width are compared to those obtained from MOCAP data (processed using two different methods). Results reveal only small differences between the estimates from the new ErKF method and those from the MOCAP methods across all six types of gait studied. Thus, the ErKF method demonstrates great promise for providing kinematic estimates across multiple gait types that are comparable to traditional MOCAP, but without traditional laboratory restrictions and constraints on human movement. The contents of this chapter are in preparation for journal submission.

Chapter 2

Effect of IMU Design on IMU-Derived Stride Metrics for Running

The contents of this chapter are published in [28].

2.1 Introduction

Studies of running biomechanics suggest that measured kinematic parameters (e.g., joint angles, stride frequency, stride length) may lead to the insight necessary to improve running performance and reduce injury risk [19, 20]. As highlighted in Chapter 1, miniature inertial measurement units (IMUs) are an attractive option for analyzing human performance outside of traditional laboratory environments due to their relatively low cost, simple setup, and portability [7]. In one application, foot-mounted IMUs provide three-dimensional foot accelerations and angular rotational velocities from which foot trajectories (and associated gait parameters) are derived during walking/running [8, 23–27, 33]. Doing so requires minimizing the accumulated drift error in the estimated foot velocity and position using the so-called "zero-velocity update" (ZUPT) method [23, 25, 34]. The ZUPT method exploits the fact that the foot is nearly stationary at some time during the stance phase and uses that condition to estimate the foot velocity drift error for each gait cycle.

Prior studies confirm that the ZUPT method yields accurate foot trajectory estimates for walking gait [24, 35, 36] and running gait with modest speeds (up to 4.36 m/s) [37]. However, little research addresses the requirements that ensure accurate trajectory estimates, particularly at faster running speeds, such as those observed in competitive middle- and long-distance running (up to 6.5 m/s) [38–40]. One limitation is that the sensor never achieves exactly zero-velocity, even in walking [41], and this assumption becomes increasingly suspect for faster running speeds. Another limitation lies with the range and sampling frequency of the inertial sensors themselves. Bailey and Harle [42] investigate the effect of IMU sampling frequency and accelerometer range on foot trajectory estimates and find that errors increase with increased running speed and decreased sampling frequency. While the errors observed in [42] are relatively small, the study considers modest running speeds (2.3–3.4 m/s) that are well below those of typical competitive middle- and long-distance running (up to 6.5 m/s). Additionally, the experiments in [42] are conducted on a treadmill rather than running overground which may also influence the conclusions. For example, significant differences may arise in gait kinematics when comparing walking on a treadmill versus overground [2]. Additionally, in a pilot study [43], the authors evaluate estimates of IMU-derived running speed using a treadmill. They observe that fluctuations in the treadmill belt speed, especially at higher running speeds with accompanying larger ground reaction forces, generate significant discrepancies between the reported belt speed and IMU-derived estimates of running speed. The speed fluctuations (i.e., accelerations) of the treadmill belt render it a non-inertial frame; thus, IMU-measured accelerations and angular velocities cannot be directly integrated to yield accurate estimates of foot velocity and position relative to the belt (as assumed using the ZUPT method). These treadmill-based limitations are a primary factor in modifying the pilot study protocol to the overground-based protocol of the study presented in this chapter. Recently, Mitschke et al. [44] examine the impact of accelerometer range on IMU-derived estimates of stride length, velocity, and tibial acceleration for overground running. They find no significant degradation in stride parameter estimates when the accelerometer range is ±32 g or greater, but significant degradation with smaller accelerometer ranges. Similar to [42], the study [44] considers only modest running speeds (up to 3.6 m/s) and does not disclose the fundamental reasons for the inaccurate estimates within the ZUPT method. In addition to the limitations imposed by accelerometer range and sampling frequency considered in these prior studies, we hypothesize that gyro range may also impose limitations on achieving accurate foot trajectory estimates for running. The effect of gyro range on stride estimates has likely not been studied previously because many commercial IMUs are unlikely to experience gyro saturation at the modest speeds observed in past studies. However, we hypothesize that the effects of gyro range on these estimates will become increasingly important at higher running speeds.

The objective of this study is to reveal the impact of an IMU's accelerometer range, gyro range, and sampling frequency on estimated stride parameters (i.e., stride length, stride angle, and total distance traveled) during overground walking and running up to competitive distance running speeds (up to 6.4 m/s) and over a wide range of sensor ranges and sampling frequencies typically found in commercially-available IMUs. This study also addresses the impact of gait speed on the estimated distance traveled in the presence of no saturation of the IMU signals. The novelty and contribution of this work are that it: (1) quantifies these effects at mean speeds commensurate with competitive distance running (up to 6.4 m/s); (2) identifies the root causes of inaccurate foot trajectory estimates obtained from the ZUPT method; and (3) offers important engineering recommendations for selecting accurate IMUs for studying human running. The results of this study will aid coaches and researchers in selecting appropriate IMUs to study stride parameters in outdoor environments and at speeds up to 6.4 m/s using the ZUPT method.

(A) (B) (C)

Figure 2.1: Two inertial measurement unit (IMU) designs and the means of attachment to a foot. (A) IMU 1 (Opal, APDM, left) and IMU 2 (custom design, Insight Sports, Ltd., right); (B and C) Side and front views of attachment of both IMUs to the instep via a Velcro strap. Sensor axes are denoted by X, Y, and Z (X and Z largely lie in foot sagittal plane and Y largely points to subject's left). Note that these axes are illustrated to aid interpretation of the raw data signals presented in Figures 2.4 and 2.8, and that the zero-velocity update (ZUPT) method herein does not require specific sensor alignment to anatomical axes.

2.2 Materials and Methods

2.2.1 Subjects and Experimental Protocol

Six healthy subjects (3 female, 3 male; mean (standard deviation) age 24.2 (±6.0) years, height 1.71 (±0.12) m, mass 68.4 (±15.2) kg) were recruited for this study. All subjects verified that they felt capable of completing the experimental protocol. Informed consent was obtained from all subjects and the study was approved by the University of Michigan IRB. Two IMU designs are employed. The first (IMU 1) provides a high accelerometer range and the second (IMU 2) provides a high sampling frequency as reported by the IMU specifications in Table 2.1. Each subject wears both IMUs strapped together and placed on the bridge of both feet as shown in Figure 2.1 (only right foot shown) and secured with a strap and tape to limit their movement with respect to each other and to the foot.

We employ a method similar to [23] to assess the accuracy of ZUPT-based foot trajectory estimates outside of laboratory environments as follows. Each subject completes ten straight 100-meter trials on (level) asphalt. The subjects complete the first two trials at a perceived slow walk and fast walk, respectively. For the third through to the tenth

Table 2.1: Specifications for IMU 1 and IMU 2.

	IMU 1	**IMU 2**
Model	Opal	Custom Design
Manufacturer	APDM	Insight Sports, Ltd.
Sampling Frequency (Hz)	128	1000
Accelerometer Range (g)	±200	±32
Angular Gyro Range (deg/s)	±2000	±4000

trial, subjects run at increasing speeds from a perceived slow jog (third trial) up to maximal sprint (tenth trial). For each trial, the subjects start at rest with the front of both shoes aligned with the start line. The subjects then walk/run 100 meters and stop with the front of both shoes aligned with the finish line. Rest between trials is self-selected by the subjects.

Since all trials start and end with the subject at rest, the time to complete each trial is readily identified from the start and end of significant acceleration (magnitude). The known 100-meter distance traveled is divided by the trial time to yield the mean speed for each trial. We employ the mean speed as an independent variable in the analyses below.

2.2.2 Overview of the ZUPT Method

While the ZUPT method is generally known, we provide an overview for the reader's benefit in following the discussions offered later in this chapter. The ZUPT method used here draws largely from [23, 24]. The method begins with estimating the instantaneous orientation of the IMU relative to an inertial frame as further detailed in [45]. The orientation is described by the rotation matrix, R, that defines the orientation of the sensor's three orthogonal axes $[\hat{\imath}_s, \hat{\jmath}_s, \hat{k}_s]$ (corresponding to x, y, and z sensor axes, respectively) relative to the orthogonal axes $[\hat{\imath}_w, \hat{\jmath}_w, \hat{k}_w]$ of a world (i.e., inertial) frame (corresponding to x, y, and z world axes, respectively, with z pointing in the direction of gravity) per

$$\begin{bmatrix} \hat{i}_w \\ \hat{j}_w \\ \hat{k}_w \end{bmatrix} = R \begin{bmatrix} \hat{i}_s \\ \hat{j}_s \\ \hat{k}_s \end{bmatrix}. \tag{2.1}$$

Following [45], the angular velocity is integrated to estimate R at each time step with a Kalman filter used to correct drift error in the tilt angle. The three components of IMU-measured acceleration (a_{xs}, a_{ys}, a_{zs}) yield the acceleration components in the world frame (a_{xw}, a_{yw}, a_{zw}) through

$$\begin{bmatrix} a_{xw} \\ a_{yw} \\ a_{zw} \end{bmatrix} = R \begin{bmatrix} a_{xs} \\ a_{ys} \\ a_{zs} \end{bmatrix} - \begin{bmatrix} 0 \\ 0 \\ g \end{bmatrix} \tag{2.2}$$

where g is the acceleration of gravity. These acceleration components in the inertial frame are used to estimate velocity in the inertial frame using the fact that the foot-mounted IMU returns to zero-velocity during the stance phase as described below.

First, zero-velocity times are identified as times of minimum angular velocity magnitude during the stance phase. A stride is defined by the time interval between two successive zero-velocity times $t_{n-1} < t < t_n$. Thus, the stride time is

$$t_s = t_n - t_{n-1} \tag{2.3}$$

and the number of data samples, l, in each stride is

$$l = t_s \times F_s + 1 \tag{2.4}$$

where F_s is the sampling frequency of the IMU. For each stride, the initial velocity is set to zero at t_{n-1} and the acceleration components in the inertial frame (Eqn. 2.2) are integrated to estimate the velocity components in the inertial frame $(\acute{v}_{xw}, \acute{v}_{yw}, \acute{v}_{zw})$. Because it is assumed

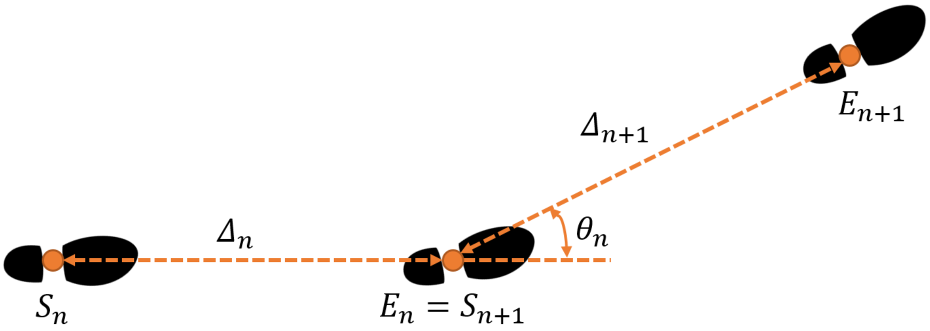

Figure 2.2: Illustration of stride length,Δ, and stride angle, θ. Orange dots on footprints represent consecutive zero-velocity times.

that the velocity at t_n returns to zero, the estimated velocity error (per sample) in the stride is

$$\vec{V}_{error} = \begin{bmatrix} \acute{v}_{xw} \\ \acute{v}_{yw} \\ \acute{v}_{zw} \end{bmatrix} (t = t_n) \times \frac{1}{l-1} \tag{2.5}$$

assuming linear drift. For each sample number, $k \in (1, l)$, within the stride (e.g., $k = 3$ for third sample in stride), a linear velocity drift error correction is applied to each of the three world frame velocity components per

$$\begin{bmatrix} v_{xcorr} \\ v_{ycorr} \\ v_{zcorr} \end{bmatrix} = \begin{bmatrix} \acute{v}_{xw} \\ \acute{v}_{yw} \\ \acute{v}_{zw} \end{bmatrix} - \vec{V}_{error} \times (k-1). \tag{2.6}$$

The corrected velocity for the whole trial is integrated to estimate the foot position throughout the trial. The position estimates are segmented by zero-velocity times and used to estimate the stride length and stride angle as follows. Figure 2.2 gives a two-dimensional illustration of the stride length and angle.

Identified zero-velocity times define the start position, $\vec{S}_n$, and end position, $\vec{E}_n$, of the n^{th} stride as given by

$$\vec{S}_n = \begin{bmatrix} S_{xw,n} \\ S_{yw,n} \\ S_{zw,n} \end{bmatrix} \tag{2.7}$$

$$\vec{E}_n = \begin{bmatrix} E_{xw,n} \\ E_{yw,n} \\ E_{zw,n} \end{bmatrix} \tag{2.8}$$

which denote the X, Y, and Z components of the start and end positions in the world frame for the n^{th} stride. The stride length, Δ, is calculated as the total three-dimensional displacement of the IMU (and thus the foot) between the start and end of the stride. We note that in many biomechanical studies, stride length often refers to only the anterior–posterior component of the foot displacement; however, in using this technology for biomechanical analyses, there is a precedent to use alternative definitions of stride length, such as the total horizontal displacement of the foot, such as in [37]. Other studies make assumptions about the sensor/foot orientation, such as assuming a particular sensor axis is perfectly aligned with the medial–lateral axis of the subject [44] or impose a level ground assumption to constrain vertical drift [46]. While such assumptions may be useful in simplifying calculations or in interpreting some of the other foot parameters obtainable using similar ZUPT method applications (e.g., if interested in the foot roll and pitch angles, precise alignment of sensor and anatomical axes may be helpful or even necessary), we do not impose such restrictions in our method (e.g., our method can be used for non-level walking/running and our method does not require any alignment between the sensor and anatomical axes). In particular, the stride length (as defined for this study) for the n^{th} stride is

$$\Delta_n = \sqrt{(E_{xw,n} - S_{xw,n})^2 + (E_{yw,n} - S_{yw,n})^2 + (E_{zw,n} - S_{zw,n})^2}. \tag{2.9}$$

The stride angle, θ, is calculated as the three-dimensional angle between successive strides' vectors. First, we define the stride vector for the n^{th} stride as

$$\vec{D}_n = \begin{bmatrix} E_{xw,n} - S_{xw,n} \\ E_{yw,n} - S_{yw,n} \\ E_{zw,n} - S_{zw,n} \end{bmatrix}. \tag{2.10}$$

The n^{th} stride angle is thus computed as

$$\theta_n = \arctan\left(\frac{\|\vec{D}_n \times \vec{D}_{n+1}\|}{\vec{D}_n \bullet \vec{D}_{n+1}}\right) \tag{2.11}$$

with × and • being the standard vector cross and dot products, respectively. We again note that the estimated stride parameters used in this study (stride length and stride angle) do not require any assumptions of a particular alignment of the sensor axes on the foot.

2.2.3 Data Processing and Analysis

Each IMU's acceleration and angular velocity data are used to estimate the foot's three-dimensional trajectory throughout each trial using the ZUPT method described above. The stride lengths are added (for both the left and right foot and then averaged) to yield the estimated total distance traveled (D_{calc}) during each trial. The cumulative distance error

$$D_{err} = (D_{calc}/D_{truth} - 1) \times 100\% \tag{2.12}$$

is reported for each trial, where D_{truth} is the known distance traveled (100 meters in this study).

To investigate the effect of accelerometer range, the raw accelerometer data from IMU 1, that possesses an acceleration range ±200 g, are numerically truncated to seven smaller ranges; namely 100, 75, 50, 24, 16, 10, and 6 g. For example, to investigate the effect of a 16 g accelerometer, any acceleration outside the range of -16 g $< a <$ 16 g is set to the corresponding limit (-16 g or 16 g) to simulate sensor saturation at that limit. These seven ranges are chosen because they are typical of commercial IMU designs. Note that the acceleration data never exceeds ±100 g in any trial and thus we use the data with the ±100 g accelerometer range as the baseline for this analysis. After the raw accelerometer data are modified in this manner, the ZUPT method is used (with the modified accelerometer data and raw angular velocity data as input) to estimate the foot trajectories. The cumulative distance error (2.12) is computed as a function of the mean speeds for each accelerometer range. These data are then fit to a linear mixed-effects model [47] to test the statistical significance of the following: (1) the effect of mean gait speed on the cumulative distance error with no accelerometer saturation (i.e., using the 100 g range accelerometer), and (2) the effect of smaller accelerometer ranges on these estimates (i.e., using the 75, 50, 24, 16, 10, and 6 g range accelerometers). The statistical model and its full results are detailed in Appendix A. Similarly, to investigate the effect of gyro range, the raw angular velocity data from IMU 1, which possesses an angular velocity range of ±2000 deg/s, are also numerically truncated to four smaller ranges; namely 1500, 1000, 750, and 500 deg/s (i.e., ranges common in commercially available IMU designs). For this analysis, we use the data with the ±2000 deg/s gyro range as the baseline. After the raw angular velocity data are modified in this manner, the ZUPT method is used (with the modified angular velocity data and raw accelerometer data as input) to estimate the foot trajectories and cumulative distance error as described above. An analogous statistical model to the one described above is also employed, but investigating gyro range instead of accelerometer range.

Additionally, for both accelerometer and gyro range effects, the amount of data that is lost due to truncation is quantified. To accomplish this, we compare the integrated area under the truncated signal and that of the non-truncated signal. In particular, to quantify the data lost due to accelerometer saturation, we define the percent data loss as

$$L_{data} = \left(1 - \frac{\int \|\vec{a}_{trun}\| dt}{\int \|\vec{a}_{non}\| dt}\right) \times 100\% \tag{2.13}$$

where $\|\vec{a}_{trun}\|$ is the acceleration magnitude of the truncated signal over a trial, $\|\vec{a}_{non}\|$ is the corresponding acceleration magnitude of the non-truncated signal, and dt is the time per sample. The integration is over the length of the trial. The percent data loss due to angular velocity saturation is defined analogously.

Note that IMU 1 is specifically chosen for studying the effects of accelerometer and gyro ranges and we verify that all data are within the design ranges (±200 g and ±2000 deg/s) for IMU 1 in all trials. By contrast, accelerometer saturation arises in IMU 2 (±32 g) at higher running speeds. However, IMU 2 is specifically chosen to study the effect of sampling frequency due to the sampling frequency limitations of IMU 1 (128 Hz). IMU 2 possesses a sampling frequency of 1000 Hz, far beyond the minimum 250 Hz rate recommended in [42] for obtaining accurate foot position and velocity estimates using the ZUPT method in running at speeds up to 3.4 m/s. For the purpose of studying the effect of sampling frequency, the accelerometer and gyro data from IMU 2 (1000 Hz) are also down-sampled to four smaller sampling frequencies (500, 250, 125, and 62.5 Hz) typical of commercial IMU designs. To that end, we employ two down-sampling methods as further described in the Results section. For these analyses, we use the data with the 1000 Hz sampling frequency as the baseline.

In addition to studying the cumulative distance error, we also report stride-to-stride variations in the differences of individual stride length and stride angle estimates as defined above (e.g., the standard deviation of the stride length difference over a trial) as these data also reveal important conclusions. To this end, the stride length difference for a particular stride and trial (e.g., stride 2 for subject 1 and trial 1) is defined as

$$\Delta_{dif} = \Delta_{base} - \Delta_{est} \tag{2.14}$$

where the Δ_{base} is the estimated stride length using the baseline (non-saturated/non-downsampled) IMU data and Δ_{est} is the estimated stride length using the truncated or downsampled data generated as discussed above. Stride angle differences are defined analogously.

2.3 Results

2.3.1 Effect of Accelerometer Range

The statistical anaysis (Tab. A.1 of Appendix A) reveals a significant effect of speed on cumulative distance error ($p < 0.01$) with the 100 g accelerometer range despite no observed accelerometer or gyro signal saturation in any of the trials with this range. Additionally, the statistical analysis reveals that using an accelerometer range of 24 g or below leads to significantly greater degradation of the estimated distance traveled with speed ($p < 0.01$ for 24 g, $p < 0.001$ for 16 g, 10 g, and 6 g) relative to the 100 g range. The accelerometer ranges of 75 g and 50 g reveal no statistically significant effects compared to 100 g. These findings are observable in Figure 2.3 which illustrates the cumulative distance error versus mean running speed for the original (100 g) accelerometer range and for each of the six truncated accelerometer ranges utilizing data from IMU 1. As illustrated, subjects achieve mean speeds up to 6.4 m/s, with the upper end of this range similar to speeds observed in elite distance running [38]. Because the peak accelerations rarely exceed 50 g, the cumulative distance errors for the 100, 75, and 50 g accelerometer ranges are visually indistinguishable on this scale as expected from the statistical results. Additionally, note that the cumulative distance error results converge across accelerometer ranges with decreased running speeds because these speeds generally yield lower accelerations (e.g., for the slowest trial, accelerations never exceed 6 g, yielding identical cumulative distance errors for all accelerometer ranges considered).

For walking and low running speeds (i.e., < 2.2 m/s), the illustrated results largely confirm the cumulative distance errors reported by others for walking [23, 24]. Additionally, for these low speeds, the IMU-estimated cumulative stride distances are nearly independent of accelerometer range. This is expected since the peak accelerations rarely exceeded 6 g for walking and low running speeds. However, for high running speeds, significant portions of each stride cycle generate accelerations larger than 6 g, leading to

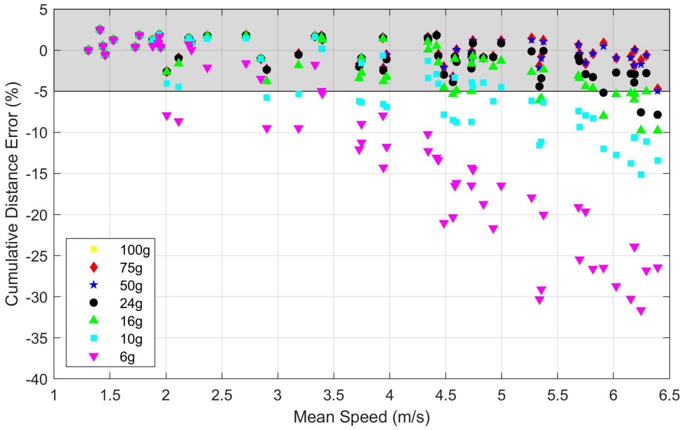

Figure 2.3: Effect of accelerometer range and mean running speed on the cumulative distance error. Note that errors arising from the 100, 75, and 50 g accelerometers are indistinguishable on this scale. The shaded region indicates estimates within ±5% error.

the large observable degradations in the estimated cumulative distance at the higher running speeds with decreased accelerometer range. Importantly, Figure 2.3 shows that accelerometers with ranges exceeding 50 g yield cumulative distance errors no greater than 5% for all mean speeds observed in this study (up to 6.4 m/s). Thus, depending on the accuracy needs for a particular use of these estimates, the ZUPT method may yield acceptable results (i.e., errors of 5% or less) even at the highest speeds observed in this study, provided no saturation arises in the accelerometer (and gyro) signals. By contrast, at the opposite extreme, errors exceeding 30% are observable for the 6 g accelerometer where significant saturation occurs.

The degradation of estimates of the cumulative distance traveled with increased speed and decreased accelerometer range traces to saturation in the accelerometer signals. Figure 2.4 illustrates the effect of truncating the accelerometer range for sample walking (Fig. 2.4A) and running (Fig. 2.4B) trials. In the sample walking trial, the three acceleration components never exceed 6 g and therefore distance estimates based on any of the accelerometer ranges considered (6 g through 100 g) yield essentially identical results. However, in the sample running trial, the acceleration components often exceed 6 g and for significant portions of the gait cycle. The data loss leads to significant foot trajectory errors largely due to how

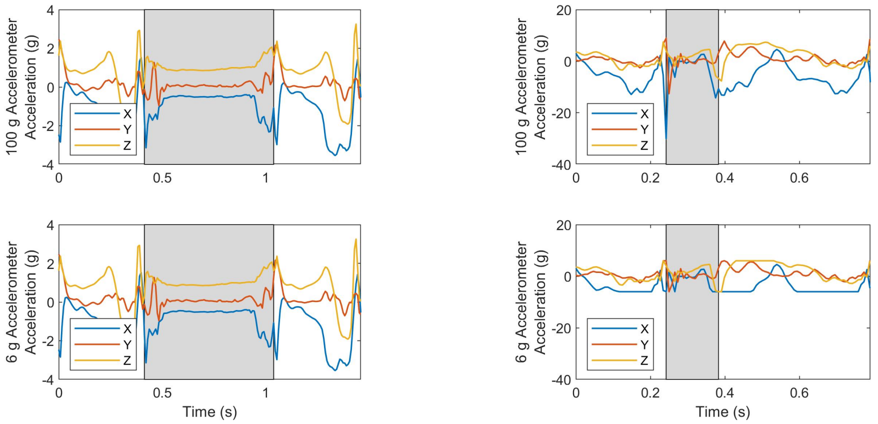

(A) (B)

Figure 2.4: Effect of accelerometer range limits on acceleration data for a sample (A) walking trial (mean speed 1.4 m/s) and a sample (B) running trial (mean speed 5.8 m/s). Acceleration data is saturated when the slope is zero as is most apparent for the X-axis acceleration of the 6 g accelerometer for the running trial. Shaded areas indicate stance phase.

the ZUPT method corrects for velocity drift error as described in detail in the Discussion.

We note that the presence of saturation does not necessarily lead to poor estimates. In particular, acceptable results may still be obtainable if the amount of data that is lost due to saturation remains small. To illustrate what might be "acceptable" levels of saturation for the accelerometer range, we further quantify the amount of data that is lost due to saturation for each trial and accelerometer range and present the relationship of the cumulative distance error and amount of data lost due to saturation in Figure 2.5. These results show that the cumulative distance errors remain below 5% when the percentage of acceleration data lost due to saturation is below 1.5%, irrespective of the accelerometer range.

Beyond studying errors in the cumulative distance traveled, we also consider differences in stride length and stride angle estimates on a stride by stride basis. To this end, we compare the estimated length and angle of each stride (where stride angle refers to the angle between successive strides as defined in the Methods) using truncated accelerometer data to the same quantities estimated from untruncated accelerometer data, employing the 100 g accelerometer as the benchmark. Figure 2.6 illustrates the standard deviation of the resulting differences in the individual stride length (Fig. 2.6A) and stride angle (Fig. 2.6B) estimates.

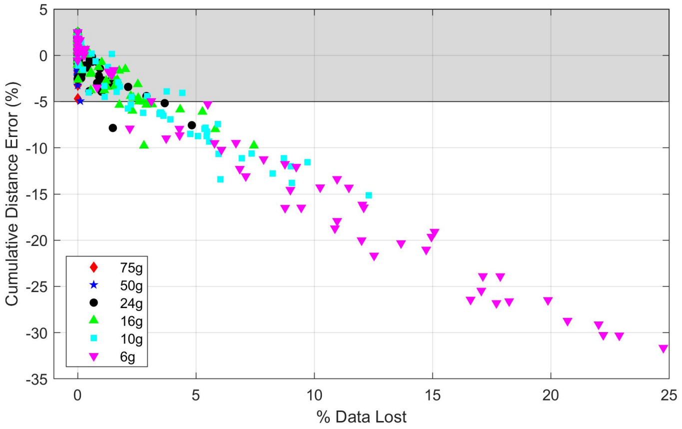

Figure 2.5: Cumulative distance error versus percentage of acceleration data lost due to saturation for all trials and for each accelerometer range. The shaded region indicates estimates within ±5% error.

When the variation is large, the agreement between truncated and baseline estimates of the given parameter for individual strides is small. These variations increase strongly with mean speed and decreased accelerometer range. As both mean speed and accelerometer range contribute to accelerometer saturation, they also significantly impact the estimates of these metrics on an individual stride basis.

2.3.2 Effect of Gyro Range

The statistical analysis (Tab. A.2 of Appendix A) reveals a significant effect of speed on cumulative distance error ($p < 0.01$) with the 2000 deg/s gyroscope range despite no observed accelerometer or gyro signal saturation in any of the trials with this range. Additionally, the statistical analysis reveals that using a gyro range of 750 deg/s or below leads to significantly greater degradation of the estimated distance traveled with speed ($p < 0.05$ for 750 deg/s, $p < 0.001$ for 500 deg/s) versus the 2000 deg/s range. Gyro ranges of 1500 deg/s and 1000 deg/s reveal no statistically significant effects compared to 2000 deg/s. These findings are observable in Figure 2.7 which illustrates the cumulative distance error versus mean running speed for the five gyro ranges considered utilizing data from IMU 1. Because the angular velocities rarely exceed 1000 deg/s, the distance error is nearly the same for the 2000, 1500,

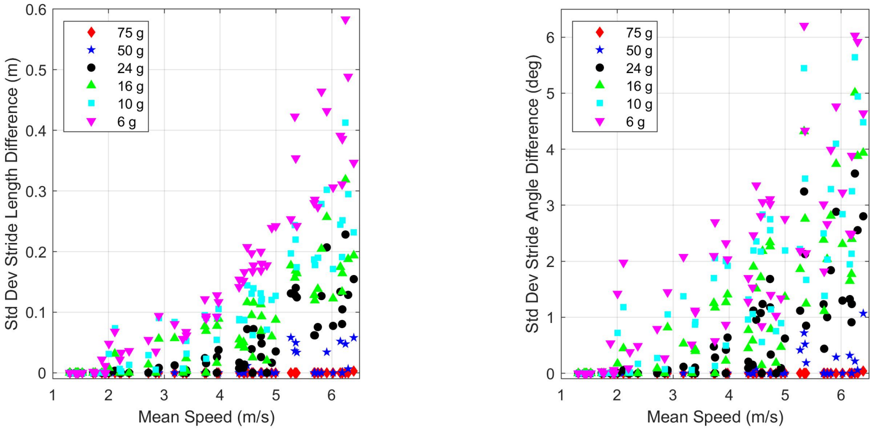

(A) (B)

Figure 2.6: Dependence of the standard deviation of difference in (A) stride length and (B) stride angle estimates with mean speed and accelerometer range. The differences are computed with respect to the results of the 100 g accelerometer as the benchmark.

and 1000 deg/s range gyros. The distance errors remain within 5% for all gyro ranges of at least 1000 deg/s for the entire range of mean speeds studied herein (up to 6.4 m/s).

As in Figure 2.3, the cumulative distance traveled is underestimated at faster (running) speeds and this underestimation increases with speed and decreased gyro range. However, the cumulative distance traveled is often overestimated at slower (walking) speeds and this overestimation increases with decreased gyro range; observe the slower (walking) trials with a 500 deg/s range gyro. The underestimation versus overestimation traces to saturation in distinct portions of the stride cycle as revealed in Figure 2.8 for sample walking (Fig. 2.8A) and running (Fig. 2.8B) trials. Observe in Figure 2.8A that the Y-axis angular velocity for the 500 deg/s gyro exhibits saturation during a modest fraction of the stance phase near toe-off (end of the stance phase) for walking. By contrast, Figure 2.8B reveals that for maximal sprinting, the same angular velocity component saturates during toe-off, heel-strike (beginning of the stance phase), and for a significant portion of the swing phase. The portion of the stride cycle in which data is lost leads to overestimation versus underestimation because of how it impacts the ZUPT algorithm as described in detail in the Discussion.

As with the accelerometer, we note that the presence of saturation in the gyro does not

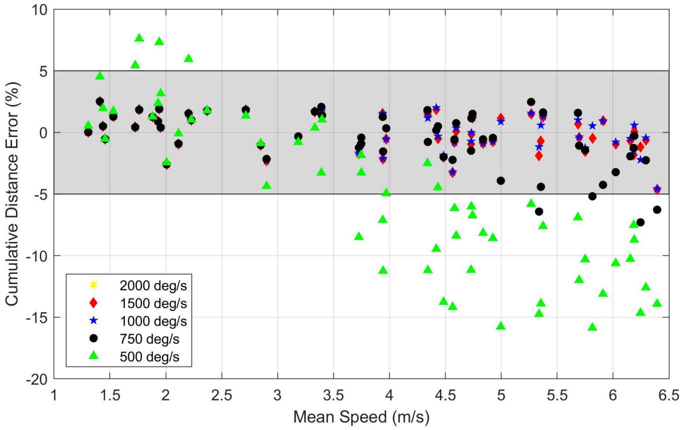

Figure 2.7: Effect of gyro range and mean running speed on the cumulative distance error. Note that distance errors arising from the 2000 and 1500 deg/s gyros are indistinguishable on this scale. The shaded region indicates estimates within ±5% error.

necessarily lead to poor estimates; in particular, acceptable results may still be obtainable if the amount of data that is lost due to saturation remains small. To illustrate what might be "acceptable" levels of saturation for gyro signals, we further quantify the amount of data that is lost due to saturation for each trial and gyro range and present the relationship of cumulative distance error and amount of data lost due to saturation in Figure 2.9. These results show that cumulative distance errors remain below 5% when the percentage of angular velocity data lost due to saturation is below 2.6%, regardless of the gyro range.

As in the previous section, we also consider differences in stride length and stride angle estimates on a stride by stride basis. To this end, we compare the estimated length and angle of each stride (where stride angle refers to the angle between successive strides as defined in the Methods) using truncated gyro data to the same quantities estimated from untruncated gyro data, employing the 2000 deg/s gyro as the benchmark. Figure 2.10 illustrates the standard deviation of the resulting differences in the individual stride length (Fig. 2.10A) and stride angle (Fig. 2.10B) estimates. When the variation is large, the agreement between the truncated and baseline estimates of the given parameter for individual strides is small. These variations increase strongly with mean speed and decreased gyro range. As both mean speed and gyro range contribute to gyro saturation, they also significantly impact the

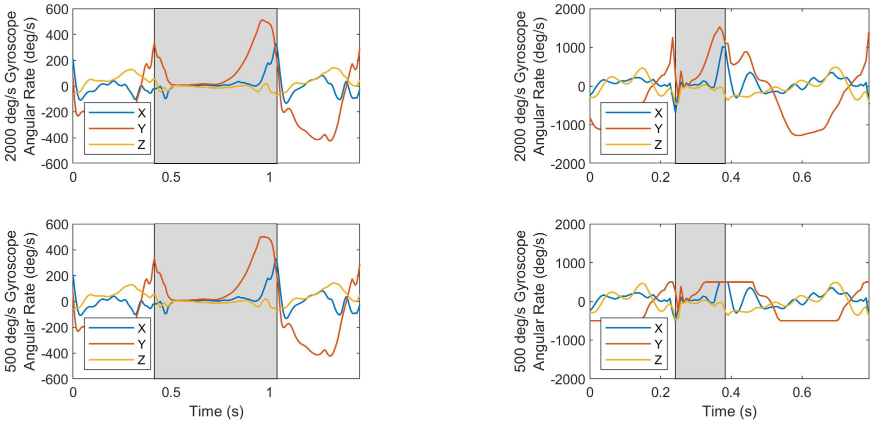

(A) (B)

Figure 2.8: Effect of gyro range limits on angular velocity data for a sample (A) walking trial (mean speed 1.4 m/s) and a sample (B) running trial (mean speed 5.8 m/s). Angular velocity data is saturated when the slope is zero as is most apparent for the Y-axis angular velocity of the 500 deg/s gyro for the running trial. Shaded areas indicate stance phase.

estimates of these metrics on an individual stride basis.

2.3.3 Effect of Sampling Frequency

Sampling methods can vary widely in commercial IMUs. In particular, one or more filters are commonly employed within the IMU hardware and/or software before data is output at the IMUs specified sampling frequency. Therefore, an IMU having a higher sampling frequency (specification) does not necessarily imply it will lead to superior estimates of stride parameters in the context of this study. Because the filters and sampling methods are generally hidden to the user and vary between manufacturers, we consider the effect of sampling frequency by studying two simple sampling methods, including both an extreme method (no filtering before down-sampling) and a common method (low pass filter before down-sampling). For both methods, data from IMU 2 are utilized as that IMU design yields data at a high (1000 Hz) sampling frequency. Neither sampling method demonstrates a statistically significant effect for the interaction of speed and sampling frequency on the cumulative distance error except for the most extreme down-sampling used in this study (Method 1 at the lowest sampling frequency). See Appendix A for full

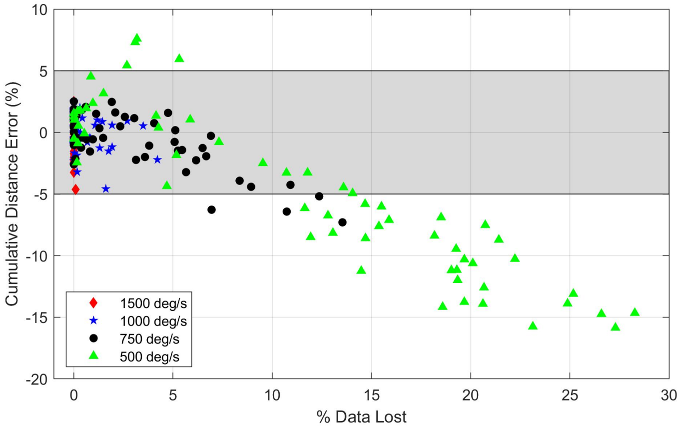

Figure 2.9: Cumulative distance error versus percentage of angular velocity data lost due to saturation for all trials and for each gyro range. The shaded region indicates estimates within ±5% error.

statistical results. Because this one exception represents a most unrealistic scenario and because no other sampling method and sampling frequency combinations studied herein reveal statistically significant effects for this interaction, we offer no further results for this effect. However, significant differences do arise in the estimated stride lengths and stride angles of the individual strides as reported below.

Method 1 constitutes simple down-sampling performed without filtering (e.g., when down-sampling from 1000 to 500 Hz, every other sample is retained). This overly simplistic approach introduces aliasing effects and hence sub-optimal results [48, 49]. Figure 2.11 illustrates the standard deviation of differences in stride length (Fig. 2.11A) and stride angle (Fig. 2.11B) estimates using Method 1 as functions of both mean speed and sampling frequency. The differences are with respect to the same quantities computed using the original data (i.e., data sampled at 1000 Hz). The standard deviation of the difference from simple down-sampling quickly grows (i.e., increasing variation) with increasing mean speed and decreasing sampling frequency. For example, at the lowest sampling frequency (62.5 Hz), the standard deviation in stride length difference becomes a significant fraction of the stride length at higher mean speeds. Thus, the reliability of these measures is significantly impacted by both mean speed and sampling frequency.

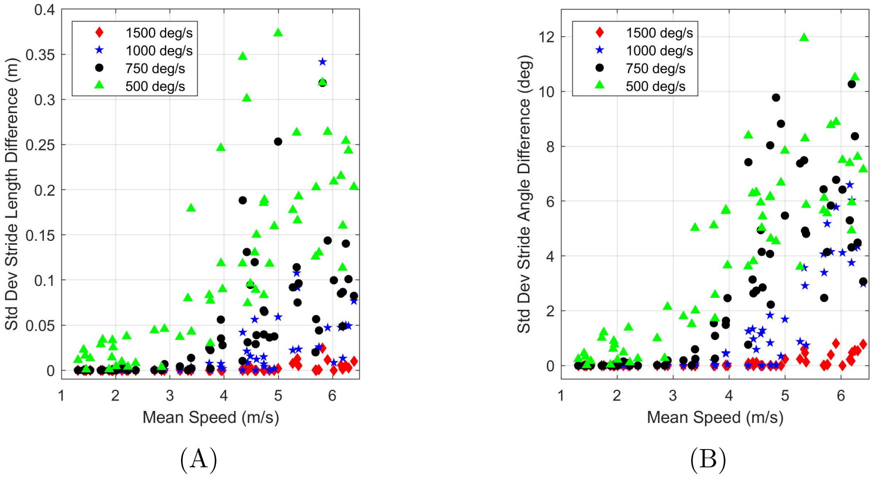

Figure 2.10: Dependence of the standard deviation of difference in (A) stride length and (B) stride angle estimates with mean speed and gyro range. The differences are computed with respect to the results of the 2000 deg/s gyro as the benchmark.

Method 2 follows a more common strategy known as decimation [50, 51], which consists of low pass filtering prior to down-sampling. We use the decimate function in MATLAB™ [52] which utilizes a low pass Chebyshev Type I filter (infinite impulse response, order 8) before down-sampling the data. Figure 2.12 illustrates the results from Method 2, analogous to those of Method 1. The results still illustrate increased differences in estimates with increased speed and decreased sampling frequency, but significantly less than that observed using Method 1 (Fig. 2.11). For example, the variation of the stride length difference is reduced by nearly a factor of five (compare scales of Fig. 2.11A and Fig. 2.12A). These results suggest that sensor hardware that employs well-designed filters can significantly mitigate the adverse impact of limited sampling frequencies.

2.4 Discussion

Overall, this study highlights the importance of proper sensor selection in order to estimate accurate gait parameters from foot-mounted IMUs using the ZUPT method. Accurate estimates of the cumulative distance traveled are possible upon limiting acceleration and angular velocity saturation. Importantly, we observe that the cumulative distance error

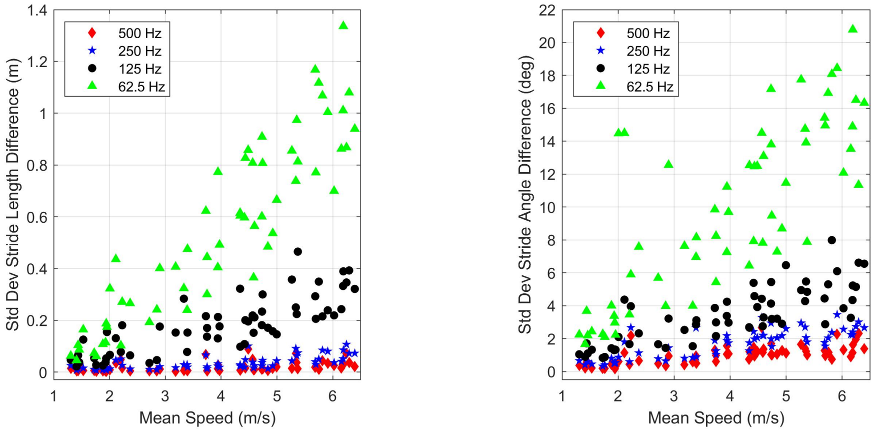

(A) (B)

Figure 2.11: Dependence of the standard deviation of difference in (A) stride length and (B) stride angle estimates with mean speed and sampling frequency. Method 1: down-sampling without filtering. The differences are computed with respect to the results of the 1000 Hz sampling frequency as the benchmark.

using the ZUPT method remains below 5% when acceleration saturation is limited to 1.5% and when angular velocity saturation is limited to 2.6%; refer to Figures 2.5 and 2.9.

We also observe that gait parameter estimates degrade with higher mean speeds even without sensor saturation ($p < 0.01$); refer to Appendix A. However, the results confirm that ZUPT-based algorithms yield accurate estimates for some applications (i.e., less than 5% cumulative distance error) over the entire range of mean speeds studied herein (up to 6.4 m/s) contingent on the IMU design. Importantly, lower range inertial sensors yield significant errors in gait parameter estimates at higher mean speeds due to (increasingly larger) data saturation. Interestingly, saturation may produce both overestimates and underestimates of the cumulative distance traveled depending on which signal (acceleration or angular velocity) is saturated, in which part of the stride cycle most of the saturation occurs, and the mean speed. These errors arise from error sources within the ZUPT method (detailed in the Methods) as follows. The gyro data is employed to estimate the orientation of the IMU (via integrating angular velocity) and this is critical to accurately resolving the acceleration into the world frame. The orientation estimates are corrected for drift error using a Kalman filter based on the core assumption of zero-mean Gaussian gyro noise. However, this assumption is

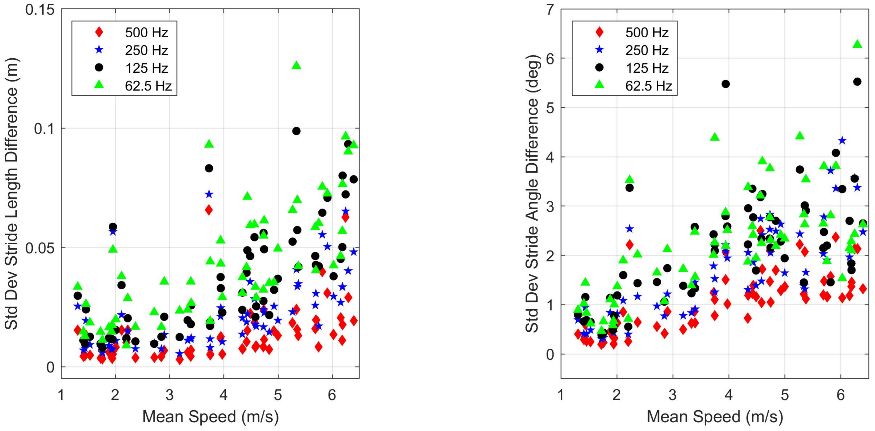

(A) (B)

Figure 2.12: Dependence of the standard deviation of difference in (A) stride length and (B) stride angle estimates with mean speed and sampling frequency. Method 2: low pass filtering before down-sampling (using MATLAB$^{\text{TM}}$ decimate function). The differences are computed with respect to the results of the 1000 Hz sampling frequency as the benchmark. Note the differences in the y-axis scales compared to Figure 2.11

violated when the angular velocity saturates, leading to inaccurate estimates of orientation and thus improper resolution of acceleration in the world frame. Subsequent integration of poorly resolved (and even possibly saturated) acceleration yields inaccurate estimates of velocity and position. Additionally, even with proper IMU orientation estimates, saturation of accelerometer signals creates velocity drift errors that do not increase linearly in time between the zero-velocity update times as assumed in the ZUPT method.

These error sources suggest an intuitive explanation for why the estimated total distance traveled is increasingly underestimated with increased speed and decreased accelerometer range. In this study, the majority of acceleration data lost due to saturation is acceleration directed opposite to the direction of travel (i.e., deceleration). Consequently, the uncorrected velocity in the direction of travel is overestimated at the end of a stride. However, when the (linear) velocity-drift correction is then applied, it consistently leads to underestimated velocity in the direction of travel and corresponding underestimated stride length. By contrast, there is no parallel explanation for why saturated gyro data may lead to both over and under estimates of the stride length. In particular, note that saturation of gyro data creates errors farther upstream in the ZUPT algorithm and specifically in the orientation estimation. Errors in the orientation estimation may yield both over and under estimates of the stride length. Despite these several error sources, accurate velocity and position estimates are still obtained if either the percentage of the missing sensor data remains small (as described above) or if the saturation occurs along a sensor axis that does not contribute significantly to the estimate.

A naïve user may be tempted to conclude that it is always best to select an IMU with the largest ranges for acceleration and angular velocity to always avoid saturation. However, increased range often comes with the tandem penalty of reduced resolution (e.g., if range is increased, but bit resolution is not) as well as increased sensor noise, which may both defeat the apparent advantage of higher range sensors. Consequently, there could well be instances where an IMU possessing an accelerometer that admits minor saturation yields superior stride parameter estimates relative to one possessing a higher range accelerometer that admits no saturation. Of course, a superior concept is to employ multiple accelerometers and/or rate gyros with increasing (and even slightly overlapping) ranges, a concept not studied herein.

We note that in estimating the total distance traveled, symmetrically distributed stride length errors (i.e., some overestimated and some underestimated) may cancel, leading to accurate estimates of total distance traveled. Therefore, it is important to understand how individual stride length and angle estimates are affected by sensor parameters. We study these effects using the reported standard deviation of the stride length (and stride angle) differences, where these differences are compared to the baseline estimates (using the maximal sensor parameters). By using both the cumulative error in the distance traveled and the standard deviations of stride length and stride angle differences, we are able to reach sound conclusions of how IMU parameters affect individual stride length estimates as reported herein despite not explicitly having stride by stride ground truth data. In particular, we note that standard deviations of stride length and stride angle differences appear to converge as sensor parameters (ranges and sampling frequency) approach the nominal parameters for that sensor (Figs. 2.6 and 2.10–2.12). This apparent convergence suggests that (as one would expect) the baseline estimates are likely the best available estimates and thus the differences likely correspond to degradations in the estimates. However, we also acknowledge that independent ground truth estimates of individual stride lengths and angles are required to confirm this conclusion and those data are not available in the present study. The convergence in standard deviations also suggests that improvements in estimates of individual stride parameters when going beyond the ranges and sampling frequencies utilized by the sensor in this study will be minor compared to the degradation effects due to sensor limitations demonstrated in this study.

For these experiments, sampling frequency shows no significant impact on estimates of the total distance traveled (except in one limited condition); however, it significantly impacts estimates of the individual stride parameters (stride length and stride angle). In particular, the variance of the individual stride parameters is significantly influenced by the filtering/sampling method employed. This effect is demonstrated using two simple down-sampling methods. While this analysis demonstrates differences in stride parameter estimates with a reduction of the sampling frequency on a single IMU, caution must be exercised when comparing sampling frequencies between IMU designs. Many factors of IMU design in addition to sampling frequency (e.g., sensor hardware, sensor placement) impact stride parameter estimates. Thus, it remains possible for an IMU with a modest sampling frequency (e.g., 128 Hz) to yield superior stride parameter estimates to another IMU design with a higher sampling frequency (e.g., 1000 Hz).

Finally, we describe several limitations of this study which we also believe do not alter the core conclusions. First, we acknowledge that the sensors available for this study both had limitations (in range and sampling frequency) that may affect the accuracy of the calculated stride metrics presented herein. Despite these limitations, we demonstrate important conclusions about the effects of the sensor parameters on the selected stride parameters. We duly note additional factors not studied herein that may impact the accuracy of stride estimates (e.g., sensor noise, sensor bandwidth, sensor resolution, Kalman filter tuning, etc.) that motivate future studies. Second, these experiments are conducted over a relatively short (100 m) distance. However, the results for the cumulative distance error are expected to hold for any (i.e., longer) distance because the cumulative distance error is equivalent to a percent error in the mean stride length estimates. Third, in the statistical analyses detailed in Appendix A, we do not evaluate subject-specific effects (i.e., we removed the effect of subjects on our results by treating subject as a random effect). Future studies could investigate the effect of subject demographics (e.g., weight, height, etc.) on estimates of gait parameters using the ZUPT method. Fourth, we note that our study is not well suited for traditional statistical power analyses. Thus, we remind the reader that caution should be employed when interpreting the effects that are not found to be significant in the statistical analyses as they may be subject to type-II statistical errors (i.e., an effect not found to be significant does not guarantee that there is no effect). However, we also note that the potential presence of type-II errors (for the effects not observed to be significant) in no way diminishes the importance of the effects that were observed to be significant and their associated conclusions. Fifth, we suggest that future studies investigate the impact of sensor properties on other stride parameters obtainable from the ZUPT method (e.g., foot clearance, foot roll angle, etc.).

2.5 Conclusions

Appropriate selection of the ranges and sampling frequencies of the inertial sensors embedded in IMUs is crucial for accurately estimating foot trajectories (hence gait parameters) from foot-mounted IMUs, and particularly for the speeds associated with competitive distance running. In this study, we investigate the effects of mean gait speed and sensor parameters on estimates of stride parameters. The novelty and contribution of this work are that it: (1) quantifies these effects at mean speeds commensurate with competitive distance running (up to 6.4 m/s); (2) identifies the root causes of inaccurate foot trajectory estimates obtained from the ZUPT method; and (3) offers important engineering recommendations for selecting accurate IMUs for studying human running. Estimates of the cumulative distance traveled (from the individual stride length estimates) degrade with speed; however, across the range of mean speeds studied here, estimates remain within 5% of ground truth if there is no or minor saturation of the accelerometer (1.5% or less) or gyro (2.6% or less) signals as defined herein. In particular, the reported experiments require accelerometer ranges of at least 50 g and gyro ranges of at least 1000 deg/s to avoid significant errors in estimates of the cumulative distance traveled for mean running speeds up to 6.4 m/s. Errors that arise due to sensor saturation trace to core assumptions that are violated in the underlying estimation procedure based on the ZUPT method (i.e., zero-mean Gaussian noise, zero-velocity, and linear velocity drift assumptions). For applications similar to the ones described in this chapter, accurate results remain possible even with modest sampling frequencies (e.g., 128 Hz), provided well-designed filters are employed.

Chapter 3

Error-state Kalman Filter for Lower-limb Kinematic Estimation: Evaluation on a Three-body Model

3.1 Introduction

With the foundation set in Chapter 2, we transition from methods that estimate single-segment kinematics (i.e., kinematics of a single foot) to methods that estimate relationships between lower-limb segments (e.g., joint angles, step width). We begin by reminding the reader of both the importance of IMU-based approaches for estimating lower-limb kinematics in many biomechanical contexts and the challenges such approaches must overcome (also highlighted in Ch. 1).

Human lower-limb kinematic measurements are critical for many applications including gait analysis, athletic performance, injury risk, warfighter performance, and elderly fall risk, among others [17, 19, 53–55]. Historically, most research studies are constrained to laboratory environments where camera-based motion capture systems (MOCAP) are used to measure body segment kinematics. A major disadvantage of lab-based studies is that experimental constraints (e.g., limited capture volume, artificial environment, and observers) may alter how subjects perform tasks, making it difficult to extrapolate results to unconstrained (real-life) environments [2, 56]. Some research studies require continuous monitoring of human kinematics, rendering lab-based methods ineffective [57–59]. In addition, camera-based systems are relatively expensive, require long setup times, and require trained researchers [53, 56]. Collectively, the above realities of lab-based experiments may significantly limit the findings and benefits of the research. Thus, there remains a strong motivation to advance the use of wearable sensors to measure human kinematics outside of the lab environment.

The most utilized sensors for mobile kinematic measurements are inertial measurement units (IMUs) which contain three-axis accelerometers and angular rate gyroscopes (with some designs also including magnetometers, GPS, barometers, or other sensors). The resulting measurements can be integrated and/or differentiated to estimate the kinematics of the body segments to which they are attached [9]. However, because of measurement noise and finite sampling rates, kinematic variables estimated via numerical integration are subject to integration drift errors. Consequently, accurate estimates of kinematics from (noisy) IMU measurements must also correct for drift errors [9, 23, 30, 59, 60]

In the context of estimating lower-limb human kinematics with IMUs, approaches that leverage known kinematic conditions and relationships demonstrate success in correcting integration drift errors in certain applications [61]. One well-known example is the zero-velocity update (ZUPT) method for computing three-dimensional trajectories of the feet [23, 25]. As emphasized in Chapter 2, this method uses the fact that, during human walking, the foot (and attached IMU) must be nearly still (zero-velocity) at some point during each stance phase to correct for drift in the estimated foot velocity. Other methods successfully estimate joint angles for single joints. For example, IMU-based knee joint angle algorithms capitalize on the fact that the knee often acts as a hinge joint [11, 62]. In addition to single-segment or single-joint methods highlighted above, recent work for multi-segment or multi-joint systems shows progress towards describing the human lower limbs. While proprietary products for such analyses exist (e.g., Xsens, Noraxon), they incorporate unspecified assumptions (hence, unspecified limitations) which is especially pertinent because accuracy of IMU-based methods are often task-specific [61]. Independent validation studies of these systems confirm such task dependence and also reveal that accuracy varies significantly between specific joint angles [63–65]. These proprietary products also have significant cost and rely on product-specific IMU hardware or even specialized wearable suits. Thus, a significant need exists for validated and well-documented methods to advance future research and applications.

Several methods exist for estimating the kinematics of the human lower limbs using a seven-body representations of the human lower limbs constituting the feet, shanks, thighs and pelvis. Ahmadi et al. [66] utilize a ZUPT method to estimate ankle position trajectories and combine those with individual segment orientation estimates to yield estimated lower-limb kinematics for straight walking on level ground and stairs. Optimization ensures the joint angles conform to assumed ranges of motion. Results are validated via comparison with MOCAP measurements for short trials (six passes through a MOCAP volume) that may not fully expose the accumulation of (long-term) drift error. The results demonstrate strong correlations ($R > 0.94$) for joint angles, but only those restricted to the sagittal plane. Teufl et al. [16] employ an iterated extended Kalman filter to estimate lower-limb kinematics and with root-mean-square (RMS) joint angle differences (all three axes) below 6 degrees relative to MOCAP measures. Additionally, their method estimates RMS stride length and step width differences of 0.04 and 0.03 meters, respectively, compared to MOCAP [67]. However, their algorithm assumes level-ground (to correct vertical drift and to identify zero-velocity update times), which renders it unsuitable for quantifying gait on general (unconstrained) terrain as often encountered outdoors. Collectively, the limitations of the studies reviewed above point to the need for a general algorithm that accurately estimates lower-limb kinematics over long trials (i.e., greater than five minutes) and without assumptions of terrain morphology.

This chapter contributes a novel error-state Kalman filter (ErKF) method for estimating lower-limb kinematics using data from wearable IMUs. We use this method to estimate three degree-of-freedom (DOF) joint angles, stride length and step width. The method presented here extends Sola's formulation of the ErKF for a single IMU [30] to a multi-IMU formulation and also incorporates biomechanical measurement models to correct integration drift errors. In contrast to [66], the method is effective for long integration times (i.e., long trials). In contrast to [16], the method does not embed a level-ground assumption. As a first step towards developing a complete (seven-body) model of the human lower limbs, we first consider herein an approximate three-body model. Doing so enables careful formulation and study of all key modeling steps but within the context of a simpler model. Additionally, evaluation on a well-characterized mechanical model permits direct evaluation of the ErKF method without the confounding error sources associated with human subjects including uncertainties in joint center locations, joint axes, sensor-to-segment alignment parameters, increased joint complexity, and soft tissue artefacts. Thus, evaluation of this novel ErKF method on a well-characterized three-body mechanical model (a "walker") is a critical step towards extension to a full (seven-body) model of the human lower limbs. We demonstrate the success of the method by comparison to three reference data sets. In the first comparison, estimated kinematic variables are compared to ground truth obtained by simulation. In the second and third comparisons, estimated kinematic variables are compared to those measured by MOCAP using an engineered three-body walker, and a human subject attempting to walk with "stiff" legs (minimal knee and ankle rotations), respectively.

3.2 Methods

3.2.1 Three-body Lower-limb Model

As a step towards estimating the lower-limb kinematics of a human (i.e., a seven-body model), we employ a novel ErKF method on a simplified (three-body) model of the lower-limbs for walking (i.e., a "walker"). We utilize the ErKF to estimate the poses (positions and orientations) of each IMU attached to each segment of the model. This simplified model

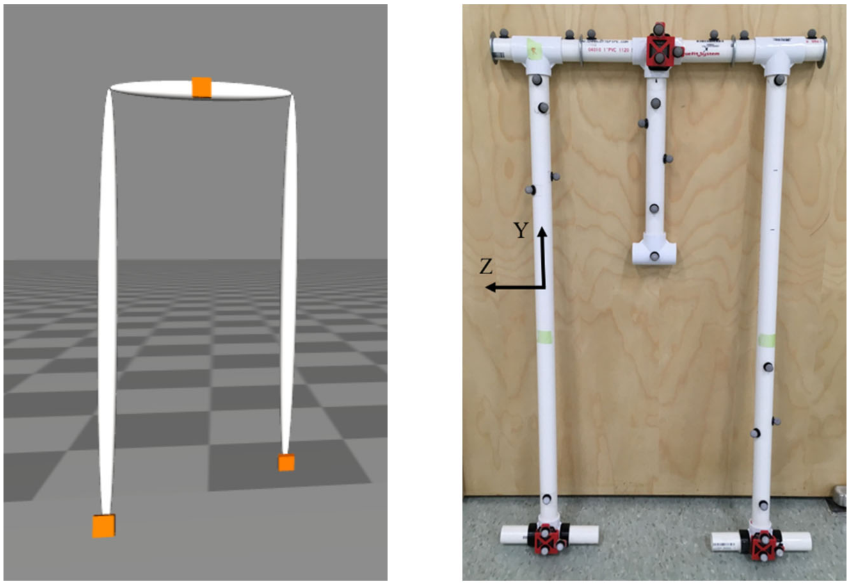

(A) (B)

Figure 3.1: Three-body model of the lower limbs for (A) simulation and (B) experiment including IMU and reflective marker placement. Body-fixed axes defined such that the x-axis points anteriorly (not shown), the y-axis superiorly, and the z-axis to the right (aligned with hinge joint axis) when the model is in a neutral upright pose (as in (b)) for all limbs.

embeds the key challenge to accurate lower-limb kinematic estimation from body-worn IMU data; namely, utilizing well-conceived measurement models to correct integration drift errors. The simplified model consists of a pelvis and two legs attached to the pelvis by hinge joints. The leg lengths and pelvic width are comparable to human anthropometrics (0.92 m and 0.39 m respectively). This model is simulated in OpenSim [32] (Fig. 3.1A) and also fabricated for experiments (Fig. 3.1B). The OpenSim model is modified from OpenSim's "Dynamic Walking Challenge" example [68].

The model includes three IMUs with one near the center of mass of the pelvis (i.e., a sacrum-mounted IMU) and one at the distal end of each leg (i.e., foot-mounted IMUs). The IMUs are attached via a weld joint in the OpenSim model and via athletic tape in the experiment.

3.2.2 Error-state Kalman Filter Method (ErKF)

While traditional extended Kalman filter equations are written with respect to the states of the system directly, the ErKF equations are written with respect to the errors in these states which then correct the estimated states. The ErKF demonstrates superior performance over a traditional extended Kalman filter for similar applications for aircrafts and robots due to key advantages including linearity, singularity avoidance, and simplicity [29, 30, 69, 70]. Recent work also shows great promise for using ErKF formulations to improve the accuracy of joint angle estimates for biomechanical applications [71].

In this formulation, each segment is treated as a free body (i.e., possesses six DOF) which yields superior estimates of joint angles versus a minimal DOF kinematic chain, as previously illustrated for the human arm [72]. This algorithm requires knowledge of the positions of the joint centers and the directions of the anatomical axes for each segment in the attached IMU's reference frame. We refer to these relationships as the sensor to segment alignment and assume they remain constant throughout a trial. Through the process model of the ErKF, IMU data from each body segment is integrated to estimate the time-dependent pose of the IMU (thus the time-dependent pose of the segment). Errors are corrected through known kinematic constraints (e.g., the joints between segments) and kinematic states (e.g., if a segment is momentarily at rest) that are incorporated in the measurement model. We describe the filter below.

3.2.2.1. States and Error-states

This multi-IMU formulation for the ErKF draws from and extends Sola's formulation for a single IMU [30] which also provides detailed derivations of relations used below. To reduce the size of the state, we do not estimate sensor biases or the gravitational acceleration. Instead, we assume sensor biases and the gravitational acceleration are well characterized (and constant) and these are estimated using IMU data during an intentional still period at the start of a trial. Therefore, the state for the j^{th} IMU, x_j, is the (10 × 1) vector

$$x_j = \begin{bmatrix} p_j \\ v_j \\ q_j \end{bmatrix} \tag{3.1}$$

where p_j is the (3 × 1) position vector of the accelerometer within the IMU in a world (i.e. lab-fixed) frame, v_j is the (3 × 1) velocity vector of the same point, and q_j is the (4 × 1) quaternion rotation vector (using Hamiltonian convention) that relates the IMU sense axis frame (hereafter called the IMU frame) to the world frame. In particular, we define q as the rotation quaternion that transforms a vector in the body-fixed frame (y^b) to its components in the world frame (y^w) per

$$\begin{bmatrix} 0 \\ y^w \end{bmatrix} = q \otimes \begin{bmatrix} 0 \\ y^b \end{bmatrix} \otimes q^* \tag{3.2}$$

where $\otimes$ denotes quaternion multiplication and q^* denotes the quaternion inverse. The error state for the j^{th} IMU, δx_j, is the (9 × 1) vector

$$\delta x_j = \begin{bmatrix} \delta p_j \\ \delta v_j \\ \delta \theta_j \end{bmatrix} \tag{3.3}$$

where δp_j and δv_j denote errors in the position and velocity, respectively, and $\delta\theta_j$ is the (three-component) attitude error vector (assumed to be small) defined such that the quaternion error δq_j obeys

$$\delta q_j = \begin{bmatrix} \cos(\frac{\|\delta\theta_j\|}{2}) \\ b\sin(\frac{\|\delta\theta_j\|}{2}) \end{bmatrix} \approx \begin{bmatrix} 1 \\ \frac{\delta\theta_j}{2} \end{bmatrix} \tag{3.4}$$

where b is the unit vector in the direction of $\delta\theta_j$ (i.e., the axis of rotation) and $\|\cdot\|$ is the Euclidean vector magnitude. The full state x is the concatenation of the states of all n IMUs in the system, namely

$$x = \begin{bmatrix} x_1 \\ x_2 \\ \vdots \\ x_n \end{bmatrix} \tag{3.5}$$

Similarly, the full error state, δx is

$$\delta x = \begin{bmatrix} \delta x_1 \\ \delta x_2 \\ \vdots \\ \delta x_n \end{bmatrix} \tag{3.6}$$

The error-state covariance matrix (associated with the full error state) is denoted by P.

3.2.2.2. Process Model

The prediction step of the ErKF uses the process model

$$\hat{x}_{j,k+1} = f(x_{j,k}, u_{j,k}) \tag{3.7}$$

for each IMU where $\hat{x}_j$ denotes the prediction of x_j, the additional subscript k denotes the k^{th} time-step, and u_j denotes the IMU data (acceleration and angular velocity). The state of each IMU at time-step $k+1$ is then predicted from the state and IMU data at the previous time-step k per

$$\hat{x}_{j,k+1} = \begin{bmatrix} p_{j,k} + v_{j,k}\Delta t + \frac{1}{2}(R_{j,k}a_{j,k} + g)\Delta t^2 \\ v_{j,k} + (R_{j,k}a_{j,k} + g)\Delta t \\ q_{j,k} \otimes \begin{bmatrix} \cos(\|\omega_{j,k}\|\frac{\Delta t}{2}) \\ \frac{\omega_{j,k}}{\|\omega_{j,k}\|}\sin(\|\omega_{j,k}\|\frac{\Delta t}{2}) \end{bmatrix} \end{bmatrix} \tag{3.8}$$

where Δt is the sampling period of the IMU, R is the rotation matrix corresponding to q, g is the gravitational acceleration vector (in the world frame), a_j is the acceleration measured by the j^{th} IMU, and ω_j is the angular rate measured by the j^{th} IMU. Note that the predicted state for each IMU is independent of the other IMUs (each IMU is treated as an independent six DOF rigid body).

During the prediction step, the covariance matrix P is also estimated as follows. The Jacobian of the process model for the j^{th} IMU at time-step k with respect to its error state vector, $F_{xj,k}$, follows from

$$F_{xj,k} = \begin{bmatrix} I_{3\times3} & \Delta t I_{3\times3} & 0_{3\times3} \\ 0_{3\times3} & I_{3\times3} & -R_{j,k}[a_{j,k}]_x \Delta t \\ 0_{3\times3} & 0_{3\times3} & (S\{\omega_{j,k}\Delta t\})^T \end{bmatrix} \tag{3.9}$$

where $I_{m\times m}$ represents an $m \times m$ identity matrix, $0_{m\times m}$ represents an $m \times m$ matrix of zeros, M^T denotes the transpose of a matrix, $[y]_x$ corresponds to the skew-symmetric form of y

$$\begin{bmatrix} y_1 \\ y_2 \\ y_3 \end{bmatrix}_x = \begin{bmatrix} 0 & -y_3 & y_2 \\ y_3 & 0 & -y_1 \\ -y_2 & y_1 & 0 \end{bmatrix} \tag{3.10}$$

and $S\{w\}$ applies the Rodrigues' rotation formula on the vector w

$$S\{w\} = S\{\phi s\} = I_{3\times3}\cos(\phi) + \sin(\phi)[s]_x + ss^T(1 - \cos(\phi)). \tag{3.11}$$

Here, ϕ is the scalar magnitude of w and s is the unit vector in the direction of w. Due to the independence of the IMUs in the prediction step, the Jacobian of the full system process model relative to the error state at time-step k, $F_{x,k}$, is

$$F_{x,k} = blkdiag(F_{x1,k}, F_{x2,k}, \cdots, F_{xn,k}) \tag{3.12}$$

where $blkdiag$ denotes the block diagonal matrix composition. The process noise covariance for the j^{th} IMU, Q_j, is

$$Q_j = \begin{bmatrix} 0_{3\times3} & 0_{3\times3} & 0_{3\times3} \\ 0_{3\times3} & \sigma_a^2 \Delta t^2 I_{3\times3} & 0_{3\times3} \\ 0_{3\times3} & 0_{3\times3} & \sigma_\omega^2 \Delta t^2 I_{3\times3} \end{bmatrix} \tag{3.13}$$

where σ_a^2 and σ_ω^2 are the noise variances for the acceleration and angular rate signals, respectively, with the values being obtained from the manufacturer or through experiment. Note that this matrix is assumed constant for each IMU and thus we do not denote a time step. Again, due to the independence of the IMUs in the prediction step, these matrices can be concatenated to form the full system process noise covariance matrix, Q, per

$$Q = blkdiag(Q_1, Q_2, \cdots, Q_n) \tag{3.14}$$

Thus, the prediction update for P is

$$\hat{P}_{k+1} = F_{x,k} P_k F_{x,k}^T + Q. \tag{3.15}$$

The process model equations above detail predictions for the state and the error-state covariance. Note that the estimated error-state mean is not calculated because it is always zero throughout the process model because the error-state mean is initialized to zero and is reset to zero following any measurement update.

3.2.2.3. Measurement Model

In the absence of any measurement during this time step we use the predicted state and error-state covariance as the best estimates at time-step $k+1$, namely

$$x_{k+1} = \hat{x}_{k+1} \tag{3.16}$$

$$P_{k+1} = \hat{P}_{k+1}. \tag{3.17}$$

However, when measurements are available during this time step, we apply corrections using the measurement model to improve the estimates as follows. The measurement model takes the functional form

$$z = h(x) + c \tag{3.18}$$

where z is the observed measurement, $h(x)$ is the expected measurement represented as a function of the state x, and c is Gaussian white noise with covariance C. Specific measurement models follow below. For each, we linearize the measurement equation by defining the Jacobian H evaluated at x

$$H = \left.\frac{\partial h}{\partial \delta x}\right|_x . \tag{3.19}$$

Consistent with [30], we use the chain rule to decompose H as

$$H = \left.\frac{\partial h}{\partial x}\right|_x \left.\frac{\partial x}{\partial \delta x}\right|_x = H_x X_{\delta x} \tag{3.20}$$

where H_x depends on the measurement model and $X_{\delta x}$ depends only on the estimated orientation. Next, the Kalman gain, K, and error-state mean, $\hat{\delta x}$, are updated per

$$K_k = \hat{P}_{k+1} H_k^T (H_k \hat{P}_{k+1} H_k^T + C_k)^{-1} \tag{3.21}$$

$$\hat{\delta x}_{k+1} = K_k (z_k - h(\hat{x}_{k+1})). \tag{3.22}$$

The error-state mean for each IMU, $\hat{\delta x}_j$, updates its respective nominal state per

$$x_{j,k+1} = \begin{bmatrix} \hat{p}_{j,k+1} + \hat{\delta p}_{j,k+1} \\ \hat{v}_{j,k+1} + \hat{\delta v}_{j,k+1} \\ \hat{q}_{j,k+1} \otimes \begin{bmatrix} \cos(\|\hat{\delta \theta}_{j,k+1}\|)/2 \\ \frac{\hat{\delta \theta}_{j,k+1}}{\|\hat{\delta \theta}_{j,k+1}\|} \sin(\|\hat{\delta \theta}_{j,k+1}\|/2) \end{bmatrix} \end{bmatrix} \tag{3.23}$$

where

$$\hat{\delta x}_j = \begin{bmatrix} \hat{\delta p}_j \\ \hat{\delta v}_j \\ \hat{\delta \theta}_j \end{bmatrix} \tag{3.24}$$

After the nominal state mean is updated, the error-state mean is reset to zero and the error-state covariance is updated per

$$P_{k+1} = G_k(I_{9n \times 9n} - KH)\hat{P}_{k+1}G_k^T \tag{3.25}$$

where G_k is the Jacobian of the error-state reset operation with respect to the error state at time-step k, defined as

$$G_k = blkdiag(G_{1,k}, G_{2,k}, \cdots, G_{n,k}) \tag{3.26}$$

where

$$G_{j,k} = \begin{bmatrix} I_{3\times3} & 0_{3\times3} & 0_{3\times3} \\ 0_{3\times3} & I_{3\times3} & 0_{3\times3} \\ 0_{3\times3} & 0_{3\times3} & I_{3\times3} - [\frac{1}{2}\hat{\delta\theta}_{j,k+1}]_x \end{bmatrix}. \tag{3.27}$$

We note that the addition of the G terms in Eqn. 3.25 in the present formulation differs from the covariance measurement update in a traditional extended Kalman filter formulation to account for the error-state mean reset (to zero) after each measurement update. The above process of prediction and measurement updates (when available) repeats each time step.

Next, we present four measurement models. The first two pertain to known kinematic states of the body segments (e.g., when the IMU is still) and the second two pertain to known kinematic constraints (e.g., constraints imposed by the two joints). Note that in the case of multiple measurements during a time step, a batch measurement update is used (i.e., all measurements are stacked and processed together).

3.2.2.3.1. Measurement Model 1: ZUPT Correction

We leverage the fact that a foot will be momentarily at rest sometime during the stance phase during gaits that do not induce significant slipping. Thus, we employ a zero-velocity update (ZUPT) correction for estimating foot trajectories which accurately describes gaits at normal walking [23, 25] through fast walking and running speeds (see Chapter 2). Within our framework, the associated measurement equation becomes

$$h_{ZUPT}(x) = v_{IMU} \tag{3.28}$$

where $h_{ZUPT}(x)$ is the expected measurement for the ZUPT correction and v_{IMU} is the (3×1) velocity vector for a foot-mounted IMU. This expected foot velocity is compared to the (virtual) observed measurement of the foot velocity

$$z_{ZUPT} = \begin{bmatrix} 0 \\ 0 \\ 0 \end{bmatrix} \tag{3.29}$$

when the IMU (foot) is (momentarily) still.

3.2.2.3.2. Measurement Model 2: Gravitational Tilt Correction

We also leverage the fact that when an IMU is still, the accelerometer in the IMU measures only gravitational acceleration and therefore functions as an inclinometer, thus enabling a gravitational (tilt) correction for IMU orientation. This correction yields the measurement model

$$h_{tilt}(x) = R^T \begin{bmatrix} 0 \\ 0 \\ 1 \end{bmatrix} \tag{3.30}$$

where $h_{tilt}(x)$ is the expected measurement for the gravitational correction and R is the rotation matrix for the still IMU. Note that in Eqn. 3.30, it is assumed that gravity acts opposite the third world-frame component (i.e., in the "–z" direction); however, this equation can be easily modified to accommodate other world-frame definitions. This expected measurement is compared to the observed measurement of tilt

$$z_{tilt} = \frac{a}{\|a\|} \tag{3.31}$$

with a being the IMU acceleration. Note that we compare the direction of unit vectors (h_{tilt} and z_{tilt}) rather than the full acceleration vector to mitigate the effects of discrepancies in magnitude caused by the IMU not being exactly still or the effects of sensor noise and bias.

3.2.2.3.3. Measurement Model 3: Joint Center Correction

Next, the joint center between two adjacent limbs must be approximately at the same position as deduced from the positions and orientations of those limbs [72]. For IMUs on adjacent limbs 1 and 2, the measurement equation becomes

$$h_{JC}(x) = p_1 + R_1 r_1 - (p_2 + R_2 r_2) \tag{3.32}$$

where $h_{JC}(x)$ is the expected measurement for the joint center correction, , the subscript $i = 1, 2$ denotes IMU_i, r_i denotes the known position of the joint center from IMU_i (and resolved in the IMU frame), and R_i denotes the rotation matrix for IMU_i. The (virtual) observed measurement for the joint center correction is

$$z_{JC} = \begin{bmatrix} 0 \\ 0 \\ 0 \end{bmatrix}. \tag{3.33}$$

3.2.2.3.4. Measurement Model 4: Joint Axis Correction

Similar to the joint center correction above, at times the joint axis must be the same as deduced from the orientations of the adjacent limbs (IMUs). An example of this correction arises when the knee is predominantly acting like a hinge [11, 62] and the flexion/extension axes of the thigh and shank must be aligned in the world frame. This can be generalized for any pair of adjacent limbs 1 and 2 per

$$h_{JA}(x) = R_1 e_1 - R_2 e_2 \tag{3.34}$$

where $h_{JA}(x)$ is the expected measurement for the joint axis correction and e_i is the aligned joint axis (unit vector) deduced from IMU_i in the frame of IMU_i. The (virtual) observed measurement for the joint axis correction is

$$z_{JA} = \begin{bmatrix} 0 \\ 0 \\ 0 \end{bmatrix}. \tag{3.35}$$

3.2.3 Evaluation of ErKF Method Using Three Reference Data Sets

We evaluate the performance of the ErKF method using three sets of reference data, namely: 1) simulated IMU data for the simulated walker with associated simulated ground truth results, 2) experimental IMU data for the physical walker with associated MOCAP results, and 3) experimental IMU data from a human subject attempting to walk stiff-legged with associated MOCAP results. These three data sets allow us to evaluate the performance of the method with increasing levels of model complexity and uncertainty (e.g., knowledge of sensor noise characteristics, sensor to segment alignment). To this end, we compare estimated and reference hip joint angles, stride length, and step width for the walker simulation and experiment (i.e., reference data sets 1 and 2 above). The reported hip joint angles mirror the International Society of Biomechanics convention for human subjects [73] with body axes defined such that the x-axis points anteriorly, the y-axis superiorly, and the z-axis to the right (aligned with hinge joint axis) when the model is in a neutral upright pose (as in Fig. 3.1B). Because there are unavoidable knee and ankle rotations during the attempted stiff-legged walking experiment, we do not report hip joint angles for reference data set 3 as they would not be representative of those measured by MOCAP. Instead, for data set 3, we compare estimated stride lengths and step widths as they would be expected to be representative of those measured by MOCAP. The definitions of these stride parameters are consistent with [67] with the following minor modifications: 1) identified footfall instances are used in place of initial contact times, and 2) the IMU position is used in place of the heel position for the three-body model (heel still used for stiff-legged walk). Appendix B details the methods for detecting footfalls and still periods. Further details for each reference data set are provided next.

3.2.3.1. Reference Data Set 1: Model Estimates for Walker Compared to Simulation

We first evaluate the performance of the ErKF method via simulation because simulation enables assessment of the ErKF method independent of many confounding factors associated with experimental data. For example, in the simulation we specify the 1) sensor error (e.g., bias, noise) parameters, 2) sensor to segment alignment parameters, 3) measurement times (e.g. when a foot is stationary, when a joint acts as a hinge), and 4) ground truth data for comparison. We first compute generalized coordinate trajectories for a straight-line walk for the three body segments. The gait consists of 200 identical strides with a mean speed and stride length of 0.33 m/s and 0.73 m, respectively. Stance and swing angular trajectories were chosen to have a waveform similar to the simplest walking model [74]. The gait also contains (0.1 second) still periods following each ground contact, permitting clear identification of times of zero-velocity of the "feet". The OpenSim model is then driven with these computed trajectories and the BodyKinematics analysis tool in OpenSim computes

Table 3.1: IMU and measurement noise values used for simulating data and for ErKF method. Noise values for the process model and the simulated IMU data are for the accelerometer (σ_a) and gyroscope (σ_ω). Measurement noise values are for the zero-velocity (σ_{ZV}), gravitational tilt (σ_{tilt}), joint center (σ_{JC}), and joint axis (σ_{JA}) measurements.

Noise Parameter	σ_a (m/s^2)	σ_ω (deg/s)	σ_{ZV} (m/s)	σ_{tilt} (deg)	σ_{JC} (m)	σ_{JA} (deg)
Value	0.027	5.66	0.01	5.73	0.01	1.15

the virtual IMU poses with respect to a fixed lab-frame. Simulated IMU data (accelerations and angular rates) that are free of noise and bias are calculated by differentiating these poses at a sampling rate of 512 Hz (sampling rate of the IMUs used for Reference Data Set 2). Finally, real (i.e., noisy) IMU data is simulated by adding prescribed zero-mean Gaussian noise to this data. The accelerometer noise value is taken from the specification sheet for the commercial IMU (Opal, APDM, ± 16 g and ± 200g accelerometers, ± 2000 deg/s gyro) used in the experiments. The gyro noise is that from the same specification sheet plus additional noise (10 deg/hr drift) to account for both bias instability and angular random walk. The joint center measurement noise comes from [16]. All noise values are summarized in Table 3.1.

Poses of each segment throughout the walk are estimated by employing the ErKF method with the simulated IMU data. Because the joints are constrained to be pure flexion/extension, the joint axis and joint center measurement corrections are applied at each time step with constant joint centers and joint axes. The segment poses follow directly from the IMU poses because the sensor to segment alignment is constant throughout the trial. Additionally, for this simulation, the sensor to segment alignment is known exactly.

Zero-velocity measurements are applied at identified footfalls while gravitational correction measurements are applied at each still period while using the measurement noise reported in Table 3.1. The accuracy of ErKF estimated hip joint angles, stride lengths, and step widths are compared to prescribed values from the original gait trajectories.

3.2.3.2. Reference Data Set 2: Model IMU Estimates for Walker Compared to MOCAP

Next, we evaluate the performance of the method on the walker during overground walking gait. A marker-based motion-capture (MOCAP) system (Vicon, 18 Vero V2.2 cameras) tracks positions of reflective markers on the model at 100 Hz. Seven reflective markers are attached to each segment (four to define the primary axes and three additional markers, see Fig. 3.1B). Positional estimates of the markers are filtered with a 4th order low-pass Butterworth filter at 20 Hz. Additionally, the attached IMUs yield sampled acceleration and angular rate data at 512 Hz. IMU poses on the segment (for sensor to segment alignment) are defined by three reflective markers attached to each IMU (Fig. 3.1B). Body frame axes for the three segments are determined as described in Section 3.2.3.1. Joint center locations are estimated at the center of the T-joints at the hips using the known dimensions of the model. A single still frame at the beginning of the trial is used to determine the positions of joint centers, IMUs, and reflective markers in the body-fixed frames and are assumed constant. MOCAP estimates of segment orientations are determined as follows using a published optimization method [75]. For each segment and time step, we record all pairwise positions between the markers on the segment and compare them to the same from the still frame. A MATLAB™ implementation of the aforementioned optimization method [76] is used to estimate segment orientation. Segment orientation estimates that yield (mean residual) marker positional errors exceeding 0.01 meters are eliminated as they indicate misidentified markers or significant marker positional error. Short time gaps (<0.05 seconds) in the orientation estimates are filled using linear interpolation for the resulting Euler angles ("unwrapped" to account for discontinuities) following which a 4th order low-pass Butterworth filter (20 Hz cut-off) is applied for data smoothing. Rotational alignment between segment axes and their associated IMU sense axes is computed using a singular value decomposition procedure [77] comparing body-fixed IMU (from gyro measurement) to segment (from MOCAP segment orientation estimate) angular velocity vectors. During the trial, a researcher manually operates (walks) the model back and forth through the 4.5-

Table 3.2: IMU and measurement noise values used for ErKF method. Noise values for the process model are for the accelerometer (σ_a) and gyroscope (σ_ω). Measurement noise values are for the zero-velocity (σ_{ZV}), gravitational tilt (σ_{tilt}), joint center (σ_{JC}), and joint axis (σ_{JA}) measurements.

Noise Parameter	σ_a (m/s^2)	σ_ω (deg/s)	σ_{ZV} (m/s)	σ_{tilt} (deg)	σ_{JC} (m)	σ_{JA} (deg)
Value	0.027	5.66	0.01	5.73	0.01	1.15

meter capture volume for ten minutes. The average sacrum velocity during straight walking is 0.44 m/s. Because the model is restricted to pure flexion/extension of the hip, joint center measurements are applied at every time step. Additionally, joint axis measurements are applied at every time step recognizing that the body-fixed z-axes (flexion/extension axes) of the pelvis and legs are aligned. As with the simulation, zero-velocity measurements are applied at all footfall instances and gravitational tilt measurements applied at all still periods. Measurement noise parameters used in the ErKF are summarized in Table 3.2.

3.2.3.3. Reference Data Set 3: Model Estimates for Human Stiff-legged Walk Compared to MOCAP

Finally, we evaluate our algorithm on a single human subject attempting to walk with stiff legs. The same MOCAP system and IMUs were used as described immediately above, only with the IMUs sampled at 128 Hz. Markers and IMUs are placed as described in [78] (See Fig. 3.2) to support additional studies; however, only data from the sacrum and feet IMUs are needed for this study. The subject is instructed to walk back and forth on a 4.5-meter walkway for ten minutes while attempting to keep each knee and ankle as rigid as possible.

IMU poses are estimated from attached reflective markers. The locations of the hip centers in the sacrum IMU's coordinate system are deduced following Hara et al. [79] using the first still MOCAP frame and are assumed constant. Additionally, the location of each heel marker in its respective foot IMU's coordinate system is estimated from this still frame (used to estimate the heel location from IMU pose estimates). Because the subject exhibits some ankle and knee rotation, the location of the hip joint center in the feet IMU coordinate systems is not constant throughout the trial. Therefore, we use IMU data to identify a

Figure 3.2: IMU and reflective marker placement for the stiff-legged walking experiment.

point near the beginning of the terminal swing stage, where the knee and ankle joint angles are likely to be consistent across strides (referred to as straight-leg instances as detailed in Appendix B). The location of the hip center in the foot IMU coordinate system during straight-legged instances (for the joint center measurement correction) is determined by averaging MOCAP-based estimates of this parameter over all straight-legged instances on the first pass through the capture volume (~ 4 instances each leg). Missing heel marker data is filled using cubic spline interpolation and then filtered with a 4th order low pass Butterworth filter at 20 Hz. Zero-velocity measurements are applied to each identified footfall instance and gravitational orientation measurements are applied to all still periods. Joint center measurements are applied at each identified straight-leg instance. Because the hip does not have a reliable joint axis alignment during this trial, no joint axis measurement was applied. Measurement noise parameters used in the ErKF are summarized in Table 3.3.

Table 3.3: IMU and measurement noise values used for ErKF method. Noise values for the process model are for the accelerometer (σ_a) and gyroscope (σ_ω). Measurement noise values are for the zero-velocity (σ_{ZV}), gravitational tilt (σ_{tilt}), and joint center (σ_{JC}) measurements.

Noise Parameter	σ_a (m/s^2)	σ_ω (deg/s)	σ_{ZV} (m/s)	σ_{tilt} (deg)	σ_{JC} (m)
Value	0.013	2.83	0.01	5.73	0.01

Table 3.4: Mean ± one standard deviation (SD) and root-mean-square (RMS) differences (IMU-true) in estimated hip joint angles and ranges of motion (ROM). Hip joint angles are flexion/extension (FE), internal/external rotation (IE), and abduction/adduction (AbAd). Values reported across both hips (NR denotes not reported).

	Mean Diff. ±SD (deg)	RMS Diff. (deg)	Mean ROM Diff. ±SD (deg)	ROM RMS Diff. (deg)
FE	-0.01 ± 0.17	0.17	0.18 ± 0.23	0.29
IE	0.00 ± 0.09	0.09	NR	NR
AbAd	0.00 ± 0.08	0.08	NR	NR

3.3 Results

3.3.1 Reference Data Set 1: Model Estimates for Walker Compared to Simulation

We open by comparing estimated outputs from the walker model (using simulated IMU data) to ground truth from the OpenSim simulation. Comparisons are made for all full strides excluding the first (transition) stride for each leg (198 strides for the right leg, 199 strides for the left leg). Joint angle estimates from the model are compared to ground truth values at each sample throughout the trial. Mean, standard deviation (SD), and root-mean-square (RMS) differences for the three joint angles are summarized in Table 3.4. RMS differences are specifically included for comparisons to results from [16, 67]. Additionally, range of motion (ROM) is estimated and compared for each stride. Summary statistics for ROM differences are also reported in Table 3.4 for flexion/extension (FE) but not for internal/external rotation (IE) or abduction/adduction (AbAd) as their true values are constantly zero for this model.

Figure 3.3 shows the differences in the three joint angles as functions of time for the right hip joint over this exemplary long (7 minute) trial (results similar for left hip). Importantly,

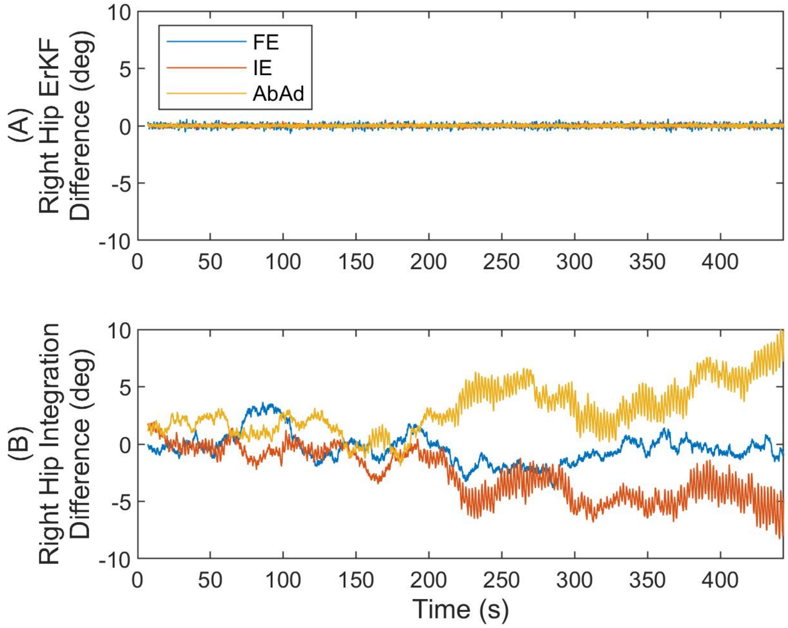

Figure 3.3: Right hip joint angle differences versus time (A) with the ErKF corrections and (B) without any filtering corrections (raw integration). Results reveal no observable drift error despite the long trial with ErKF method. Hip joint angles are flexion/extension (FE), internal/external rotation (IE), and abduction/adduction (AbAd).

the results reveal no observable drift in the joint angle differences with time (slopes of linear fits of the joint angle differences versus time remain below 0.1 deg/hr across all joint angles). By contrast, without any filter corrections, the differences can grow to up to 10 degrees due to drift over this same time interval.

Figure 3.4 illustrates the estimated FE angle compared to ground truth during the gait cycle where time is normalized by gait cycle time (which begins and ends with the instances of identified footfalls). Shown are the average (solid line) and one standard deviation (shaded region) across all strides.

We also report the accuracy of the estimated stride length and step width as summarized in Table 3.5. The mean differences are less than 1% of the average values for both stride length (0.73 m) and step width (0.39 m), while the RMS differences remain within 1% and 4% respectively.

Finally, we report the accuracy of the estimated foot IMU trajectories for each leg

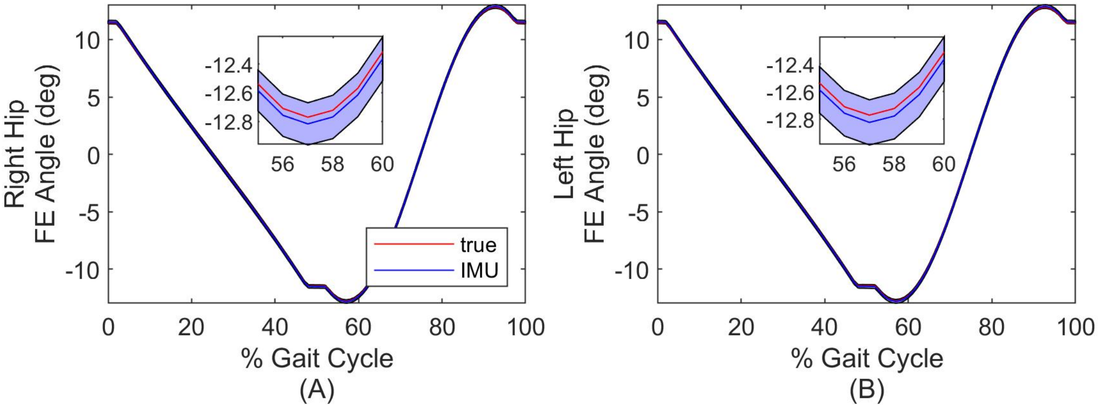

Figure 3.4: Mean and standard deviation of the estimated hip flexion/extension (FE) angle for the right (A) and left (B) hip. Solid lines denote mean and shaded regions denote ± one standard deviation. Time is normalized by gait cycle time. Insets provide zoomed images where small differences are apparent.

Table 3.5: Mean ± one standard deviation (SD) and root-mean-square (RMS) differences (IMU-true) in estimated stride length and step width for simulation.

	Mean Diff. ±SD (m)	RMS Diff. (m)
Stride Length	0.01 ± 0.01	0.01
Step Width	0.00 ± 0.01	0.01

for the duration of the stride cycle. Figure 3.5 compares the forward, lateral and vertical coordinates of the right (Fig. 3.5A) and left (Fig. 3.5B) foot IMU to ground truth. Both mean (solid line) and one standard deviation (shaded region) are illustrated as functions of time (normalized by gait cycle). Note significantly enlarged scales for lateral and vertical displacements. Additionally, note that these trajectories show the relative displacement of the IMU center and not the ground contact point itself (refer to Fig. 3.1A); thus, negative vertical displacement (Fig. 3.5) does not necessarily represent penetrations of the ground.

3.3.2 Reference Data Set 2: Model IMU Estimates for Walker Compared to MOCAP

Next, we compare estimated outputs from the model using measured IMU data to those measured by MOCAP. The results below report the differences in estimated kinematical

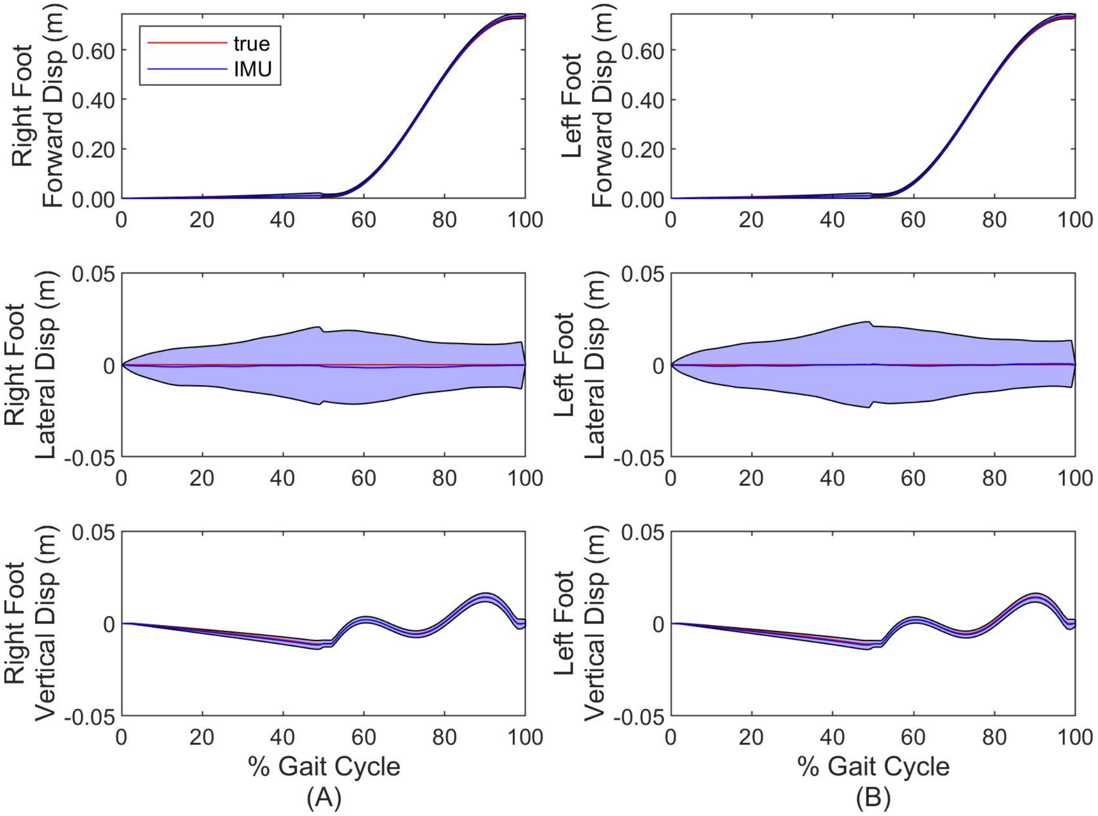

Figure 3.5: Forward, lateral and vertical coordinates of right (A) foot and left (B) foot compared to ground truth. Solid lines denote the mean and shaded regions denote ± one standard deviation. Note significantly enlarged scales of lateral and vertical displacements.

quantities obtained by the two measurement modalities. Recall that the experimental procedure requires repeated walking through the MOCAP capture volume and thus consists of straight walks through the capture volume separated by sharp turns. Since the sharp turns do not represent human-like gait, we focus our evaluation only on the "straight walking strides". A straight walking stride is defined as one where the total displacement of the foot during the stride is no more than fifteen degrees from the primary direction of travel and the stride length is greater than 0.2 meters. We also exclude from analysis the transition stride following a turn for each leg.

Consider first the differences in joint angle estimates from the IMU-based and MOCAP-based methods using data from the straight walking strides (239 strides for the right leg, 215 strides for the left leg). Bland-Altman plots of Figure 3.6 [80] illustrate the

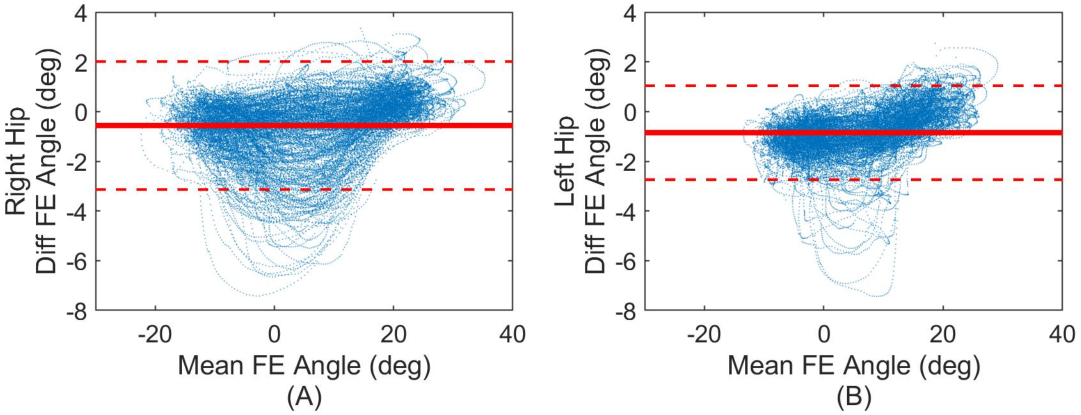

Figure 3.6: Bland-Altman plots of flexion/extension (FE) angle between IMU and MOCAP estimates for right (A) and left (B) hips. Blue points denote all samples, solid red line denotes the mean difference (IMU-MOCAP), and the red dashed lines denote 95% limits of agreement (LoA).

Table 3.6: Mean ± one standard deviation (SD) and root-mean-square (RMS) differences (IMU-MOCAP) in estimated hip joint angles and ranges of motion (ROM). Hip joint angles are flexion/extension (FE), internal/external rotation (IE), and abduction/adduction (AbAd). Values reported across both hips (NR denotes not reported).

	Mean Diff. ±SD (deg)	RMS Diff. (deg)	Mean ROM Diff. ±SD (deg)	ROM RMS Diff. (deg)
FE	-0.70 ± 1.17	1.36	0.85 ± 1.06	1.36
IE	-0.39 ± 0.29	0.48	NR	NR
AbAd	0.14 ± 0.56	0.58	NR	NR

95% limits of agreement (mean difference ± 1.96 times the standard deviation) between the two measurement modalities for the hip FE angle. Since the motion induces pure FE, we do not report results for IE and AbAd as they are nominally zero. The mean differences for FE remain less than 1 degree for both hips with limits of agreement less than 3.2 degrees across both hips.

The mean, SD, and RMS differences for all three joint angles and the ROM difference for FE are reported in Table 3.6.

Next, we evaluate how the differences in estimated joint angles vary with time over the entire ten-minute trial. Figure 3.7 illustrates the right hip joint angle differences versus time for all straight walking strides (similar results for left hip). While very small biases between the two joint angle estimates exist, the results reveal no observable drift in the differences

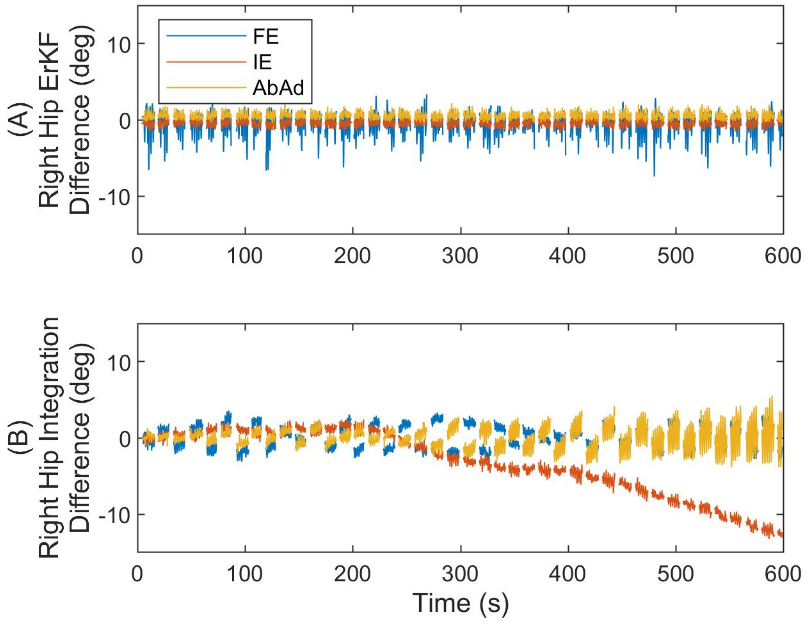

Figure 3.7: Right hip joint angle differences versus time for all straight walking strides (A) with the ErKF corrections and (B) without any filtering corrections (raw integration). Results reveal no observable drift error despite the long trial with ErKF method. Hip joint angles are flexion/extension (FE), internal/external rotation (IE), and abduction/adduction (AbAd).

over the ten-minute trial (slopes of linear fits of the joint angle errors versus time remain below 1.8 deg/hr across all joint angles). By contrast, without any filter corrections, the differences can grow to up to 13 degrees due to drift over the 10-minute trial.

Consider next a comparison of the FE estimates through the gait cycle as reported in Figure 3.8, following the same procedure described above in the context of Figure 3.4. Illustrated are the mean (solid curves) and one standard deviation from the mean (shaded regions) for both measurement modalities. The largest differences in the means arise during the stance phase. However, the measured stride-to-stride variability in FE angle (the average width of the shaded regions) is only 0.2 degrees larger for the IMU-based estimates versus MOCAP estimates.

Finally, we assess the differences in estimated stride length, step width and the trajectories of both feet for all straight walking strides. The differences in estimated stride length and step width over all strides are reported in Table 3.7. The mean differences

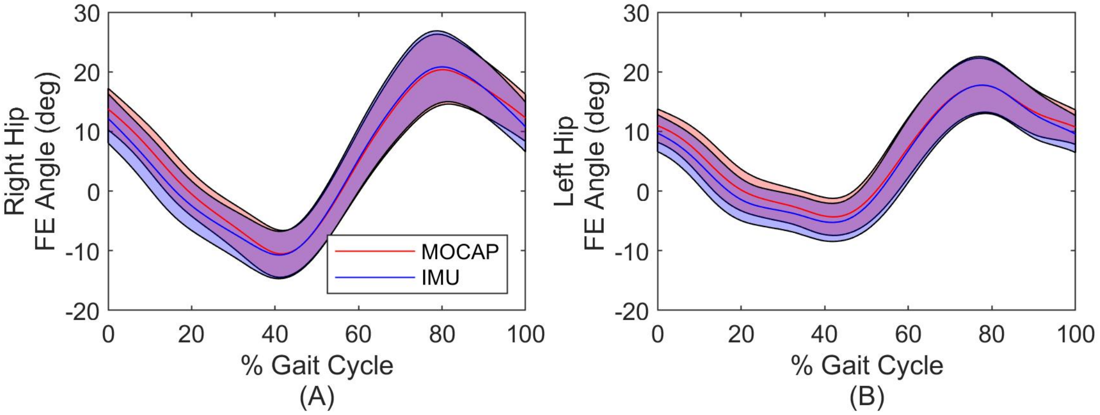

Figure 3.8: Mean and standard deviation of the estimated hip flexion/extension (FE) angle for the right (A) and left (B) hip. Solid lines denote mean and shaded regions denote ± one standard deviation. Time is normalized by gait cycle time.

Table 3.7: Mean ± one standard deviation (SD) and root-mean-square (RMS) differences (IMU-MOCAP) in estimated stride length and step width for experimental model comparison.

	Mean Diff. ±SD (m)	RMS Diff. (m)
Stride Length	0.01 ± 0.05	0.05
Step Width	0.01 ± 0.02	0.02

remain below 2% of the average value for both stride length (0.77 m) and step width (0.38 m), while the RMS differences remain below 7% and 5%, respectively.

Figure 3.9 compares the forward, lateral and vertical coordinates of the right (Fig. 3.9A) and left (Fig. 3.9B) foot IMU to those measured by MOCAP. Both mean (solid line) and one standard deviation (shaded region) are illustrated as functions of time (normalized by gait cycle). Note significantly enlarged scales for lateral and vertical displacements. Additionally, note that these trajectories show the relative displacement of the IMU center and not the ground contact point itself (refer to Fig. 3.1B); thus, negative vertical displacement (Fig. 3.9) does not necessarily represent penetrations of the ground.

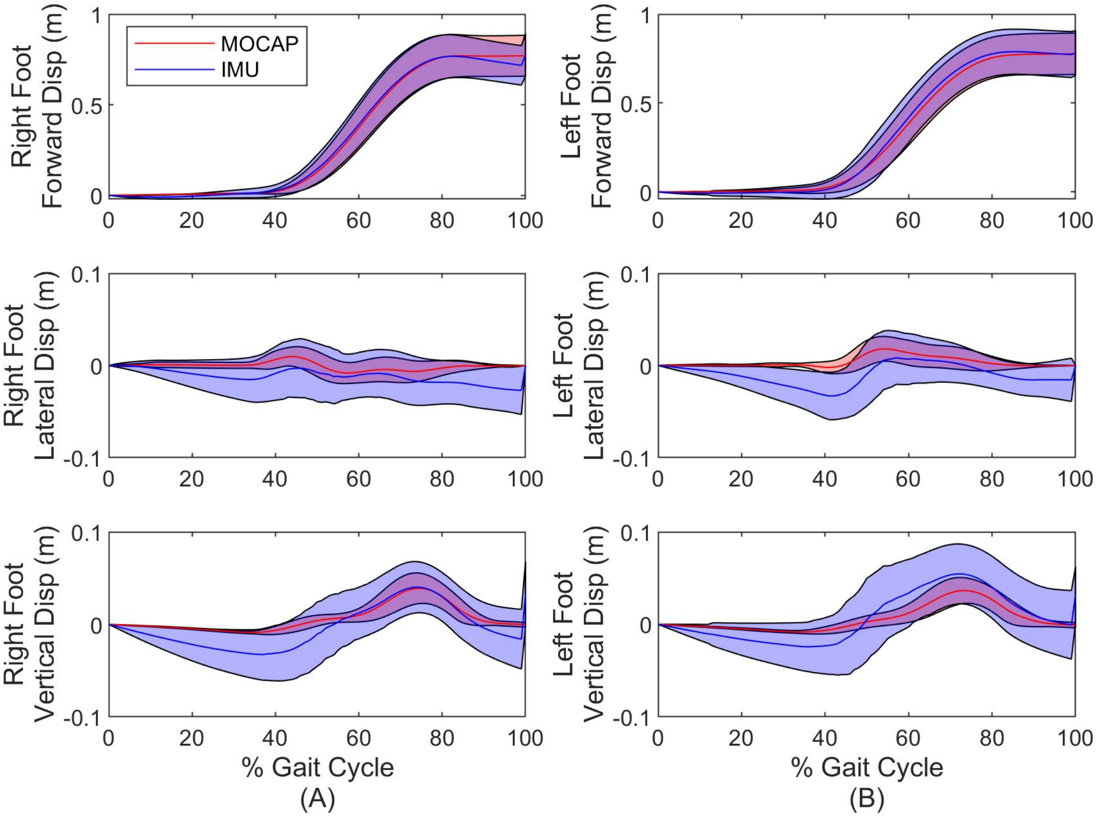

Figure 3.9: Forward, lateral and vertical coordinates of right (A) foot and left (B) foot compared to MOCAP. Solid lines denote the mean and shaded regions denote ± one standard deviation. Note significantly enlarged scales of lateral and vertical displacements.

3.3.3 Reference Data Set 3: Model Estimates for Human Stiff-legged Walk Compared to MOCAP

Finally, we consider the results for a human attempting to walk with stiff legs, which approximates the motion of the three-body walker model. We focus on the estimated stride length and step width deduced from IMU and MOCAP measurements. As in Reference Data Set 2, we evaluate only straight walking strides. Additionally, we do not evaluate differences in estimated hip joint angles due to the unavoidable (small but confounding) knee and ankle rotations that arise while attempting to walk with stiff legs. Table 3.8 reports the mean, SD, and RMS differences in the stride length and step width over all strides for the two measurement modalities. The mean differences remain below 1% and

Table 3.8: Mean ± one standard deviation (SD) and root-mean-square (RMS) differences (IMU-MOCAP) in estimated stride length and step width for a human attempting to walk with stiff legs.

	Mean Diff. ±SD (m)	RMS Diff. (m)
Stride Length	0.00 ± 0.03	0.03
Step Width	-0.06 ± 0.04	0.07

20% with RMS differences of 4% and 24% when compared to the average stride length (0.85 m) and step width (0.30 m), respectively.

3.4 Discussion

This chapter contributes an IMU-based method that accurately estimates the kinematics of a simplified three-body model of the human lower limbs for overground walking. The estimation method, developed using an error-state Kalman filter, fuses acceleration and angular rate data from three independent IMUs (one per rigid body) using four kinematic constraints. The kinematic constraints capture 1) foot zero-velocity updates, 2) gravitational tilt corrections, 3) joint center corrections and 4) joint axis corrections. The model is tested using three sets of comparison data, namely: 1) simulated IMU data from a simulated walker that yields ground truth results, 2) experimental IMU data from a physical walker with associated MOCAP results, and 3) experimental IMU data from a human subject attempting stiff-legged walking with associated MOCAP results.

Results using simulated IMU comparison data demonstrate the success of the underlying IMU-based estimation model when all required inputs (e.g., noise parameters, sensor to segment alignments) are known and when critical measurement times (e.g., zero-velocity times) are also known. Under these conditions, the hip angle estimates remain highly accurate (RMS difference below 0.2 degrees) and without detectable drift error despite long-duration trials (~7 min). Additionally, stride length and step width estimates exhibit very small differences (RMS less than 1% and 4% respectively) when compared to ground truth values.

The experimental results for the second comparison data set with an experimental walker demonstrate excellent agreement between the IMU and MOCAP-based estimates for the hip joint angles, stride length, step width, and foot trajectories. In particular, the IMU and MOCAP-based estimates of the hip joint angles exhibit limits of agreement less than 3.2 degrees for FE with RMS differences less than 1.4 degrees across all three hip angle axes. Additionally, RMS differences for stride length and step width remain below 7% and 5% respectively, compared to nominal values. Importantly, the differences in all kinematic variables did not appear to drift despite longer duration trials (~10 minutes). Because the differences neither drift nor increase with time, there is every reason to anticipate similarly tight error bounds over even longer time periods. Moreover, the IMU-based estimates exhibit similar variation in FE compared to MOCAP estimates; refer to the similar spread of the shaded regions in Figure 3.8. In the absence of a prior study like ours (i.e., evaluating IMU-based lower-limb kinematic estimation methods on a mechanical walker), there exist prior work evaluating IMU-based methods on humans that we can use as a basis for comparison (albeit imperfect). Recall that Teufl et al. [16] estimate the joint angles of the human lower-limbs from IMU data (via an iterated extended Kalman filter) during a 6-minute walking test for comparison to MOCAP results [16]. Consequently, results from this study might be compared to those of [16] by focusing on the knee joint in [16] as it acts predominantly like a hinge during walking (as does the hip joint in the three-body model herein). Doing so reveals that the RMS differences (relative to MOCAP) reported in [16] (~1.5 degrees) is remarkably similar to that reported herein (1.37 degrees), although also acknowledging that this comparison is limited due to obvious differences between the three-body model for a walker and a seven-body model for a human. Importantly though, the model herein removes limitations in [16] including the assumption of level ground. Consequently, the method herein may hold great promise in extending to a seven-body model for a human and particularly for applications where the level ground assumption does not hold, including during activities of daily living and for outdoor sports and exercise. Accurate results for this second comparison data set may also be affected by uncertainties in model inputs such as sensor to segment alignment and footfall and still period detection. We mitigate these uncertainties by using MOCAP data to establish sensor to segment alignment and to manually correct misidentified footfalls. While this yields a method that is not truly ”MOCAP-free”, these topics (sensor to segment alignment and still period detection from IMU data alone) are themselves active areas of research for human applications [81–83].

The experimental results for the third comparison data set from a human subject attempting to walk with stiff legs also demonstrate promise. In particular, the stride length and step width estimates using IMU data are remarkably consistent with those estimated by MOCAP data. For instance, the mean IMU-based stride length estimates remain within 1% of the MOCAP estimates, which is consistent with past studies employing a single foot-mounted IMU [23]. However, one cannot estimate step width while employing a single foot-mounted IMU as accomplished in this study by fusing data from three IMUs. We also note the remarkable similarity in RMS stride length and step width differences for a human subject presented here (0.03 and 0.07 m, respectively) compared to Teufl et al. [67] (0.04 and 0.03 m, respectively) and despite the simplicity of the present model (3-segment compared to 7-segment model of the lower limbs). However, we also acknowledge differences in the present study versus [67] including the number of subjects (1 versus 24 subjects, respectively) and the type of gait (stiff-legged versus normal walking, respectively). The mean and SD differences for IMU-based step width estimates in the present method remain within 20% and 13%, respectively, of the MOCAP estimates. The lower SD difference (compared to the mean) indicates that the estimates are likely affected by systematic errors (e.g., in sensor to segment alignment or knee and ankle motion). Thus, improved calibration procedures or appropriate compensation methods may significantly improve mean differences in step width. Alternatively, for research primarily concerned with variations in step width rather than the nominal value (e.g., [21, 84]), IMU methods yielding low SD differences in stride parameters compared to a gold standard (i.e., high precision) may be sufficient despite higher mean differences. Importantly, the stride metric estimates remain converged over the long duration (10 minutes) trials. Additionally, this convergence follows from the relatively infrequent (once per stride) positional updates for the joint centers. Overall, these latter results are particularly important because they foretell future success in advancing this approach to a seven-body model of the human lower limbs composed of the pelvis, thighs, shanks, and feet.

3.5 Conclusions

This study contributes a novel ErKF kinematic estimation method for the lower limbs and evaluates the method for a (simplified) three-body model. This method relies on kinematic constraints to reduce or eliminate relative integration drift errors between segments. In contrast to most other IMU-based methods for estimating full lower-limb kinematics, this new method does not rely on data from magnetometers (and is thus immune to magnetic field disturbances) nor does it rely on the assumption of level ground. Estimates of key kinematic variables are validated through simulation and through experiments on a mechanical ”walker” and on a human subject (trying to walk with stiff legs). The results of this study reveal that the ErKF method accurately estimates joint angles and stride metrics when the kinematic constraints (i.e., joint center locations, joint axes, and IMU still times) are well-characterized. For example, experimental RMS differences (between ErKF and MOCAP estimates) of the hip joint angles remain below 1.5 deg for the mechanical walker across all three angular degrees of freedom for the joints, and with RMS differences in estimated stride length and step width of 0.03 and 0.07 meters, respectively. The success of the ErKF method for the three-body model foretells success in extending the method to the full seven-body model of the lower limbs for human subjects.

Chapter 4

Evaluation of Error-state Kalman Filter Method for Estimating Human Lower-limb Kinematics during Various Walking Gaits

4.1 Introduction

With the demonstrated success of the ErKF method for a simplified three-body model of the human lower limbs in Chapter 3, the model is now extended to a full seven-body model, representing the feet, shanks, thighs, and pelvis. As discussed in the previous chapter, a variety of IMU-based methods for human lower-limb kinematic estimation exist; however, many of them rely on specialized assumptions (e.g., level ground, knee acting as pure hinge) and/or their accuracy is only evaluated against normal walking gait. For a kinematic estimation method to be applicable to a wide variety of biomechanical studies, other types of movements, which offer greater challenges to these methods (see for example Ch. 2), must be evaluated. Some studies have begun to address the need to validate IMU-based methods against non-normal walking movements including for short dynamic movements [64, 85], calibration movements [78, 86], military movements [87], and skiing [88]. However, few (if any) studies address this need for walking gaits other than normal speed, straight line walking. Studying the kinematics of a wide range of gait types is critical to many uses including in clinical applications where gait analysis is utilized in identifying injury risk, quantitatively assessing level of gait pathology, and informing and assessing treatment plans [21, 89, 90]. Motivated by these needs, the present study contributes a new ErKF method applicable to a wide variety of walking gait types.

Extension of the work in Chapter 3 on a constructed walker to a seven-body model of human subjects introduces many additional complexities. For example, biological joints are far more complex than mechanical joints in both their translational and rotational degrees of freedom. Additionally, due to soft tissue, it is more difficult to accurately identify joint centers and joint axes on human subjects. As a result, the ErKF method must handle greater errors in characterizing the joint centers and axes and thus greater errors in the calculated sensor to segment alignment parameters (i.e. joint center locations and rotations between sensor and anatomical frames). Additionally, soft tissue effects can cause both systematic and ”random” (i.e., from vibrations) movement of the IMUs relative to the underlying skeleton, which can further impact the quality of estimates. However, it is important to recognize that these complexities also affect traditional marker-based MOCAP estimation methods on human subjects; hence, neither method can be expected to yield ground truth data.

In this chapter, the ErKF method is extended to a full seven-body model of the human lower limbs and evaluated for a variety of walking gait types. Importantly, a novel application of the joint axis measurement is utilized on the hip and knee to reduce orientation drift errors without assumptions based on gait type or independent estimates of how the hip and knee behave (e.g., not strictly enforcing hinge-like behavior). Joint angles, joint angle ranges of motion, stride length, and step width estimates are compared to reference MOCAP data that is processed using two different methods. The present study demonstrates that the ErKF method estimates these kinematic measures comparably to MOCAP estimates over

Table 4.1: IMU and measurement noise values used for ErKF method. Noise values for the process model are for the accelerometer (σ_a) and gyroscope (σ_ω). Measurement noise values are for the zero-velocity (σ_{ZV}), gravitational tilt (σ_{tilt}), joint center (σ_{JC}), knee joint axis ($\sigma_{JA,Knee}$), and hip joint axis ($\sigma_{JA,Hip}$) measurements.

Noise Parameter	σ_a (m/s^2)	σ_ω (deg/s)	σ_{ZV} (m/s)	σ_{tilt} (deg)	σ_{JC} (m)	$\sigma_{JA,Knee}$ (deg)	$\sigma_{JA,Hip}$ (deg)
Value	0.013	2.83	0.01	5.73	0.01	1.15	57.3

the six types of gait included in companion experiments.

4.2 Methods

4.2.1 ErKF Method for Seven-body Lower-limb Model

The novel ErKF method uses an array of body-worn IMUs to estimate the lower-limb kinematics on a human and particularly the joint angles for the hip, knee, and ankle, and the stride length and step width. For this purpose, a seven-body model of the human lower-limbs, consisting of the feet, shanks, thighs, and pelvis is utilized; refer to Figure 4.1. The underlying formulation of this seven-body model largely follows and extends the same formulation detailed in Chapter 3 for the three-body model. As with the three-body model, zero-velocity update measurements are applied to the foot-mounted IMUs at detected footfall instances; refer to Section 3.2.2.3.1. Gravitational tilt correction measurements are applied to any IMU that is detected to be still; refer to Section 3.2.2.3.2. Joint center correction measurements are also applied at all time steps for all six joints (same noise parameter used for all joints); refer to Section 3.2.2.3.3. Measurement noise parameters used in the ErKF are summarized in Table 4.1. The noise parameters are the same as used for the human attempting to walk with stiff legs in Chapter 3, but with additional noise parameters for joint axis measurements.

In contrast to the three-body model in Chapter 3 for a mechanical walker, the joints of the human lower limbs are not single degree of freedom joints, necessitating a modified approach for the joint axis correction measurements for the seven-body model. Similar to

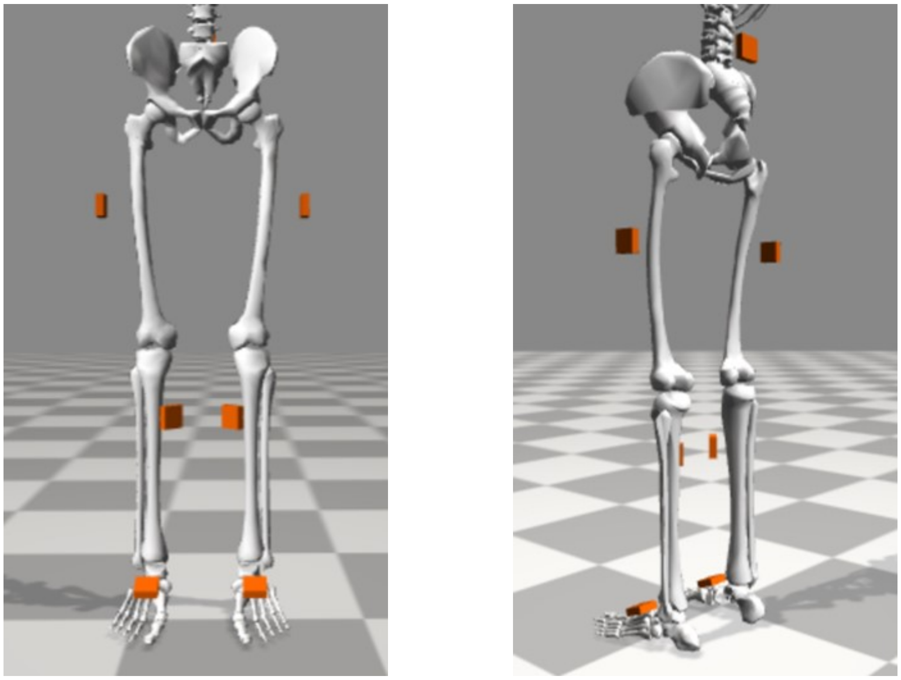

(A) (B)

Figure 4.1: Seven-body model of the lower limbs consisting of the pelvis, thighs, shanks, and feet; visualized using OpenSim. (A) Front and (B) back views. Orange boxes represent IMU locations. Note that while OpenSim's Gait2354 skeletal model is used here for visualization, the ErKF method treats each segment as an independent body possessing six degrees of freedom.

[11, 62], the method developed here exploits the fact that the knee predominantly acts like a hinge (i.e., small internal/external rotation and abduction/adduction) during normal gait. Unlike [11] where a hinge constraint is applied only during periods of detectable hinge-like knee movements, the present method assumes a ”soft” hinge constraint at all time steps, assuming the flexion/extension axes of the thigh and shank remain generally aligned. The same mathematical equations as in Section 3.2.2.3.4 are used to apply this measurement correction; however, because this constraint is an approximation, a higher measurement variance (see Tab. 4.1) is used rendering this a ”soft” constraint.

Another distinction between the three-body model of the walker and the seven-body model of the human derives from soft-tissue deformations of the lower limbs. In particular, soft tissue of the thigh allows significant relative motion between the thigh IMU and the underlying femur. When this movement is ignored (as in the ErKF formulation used here), the hip joint center measurement induces significant bias and/or drift in the estimated hip joint angles as described next, and particularly the internal/external rotation. Note that the joint center measurement correction relies on accurate estimates of the joint center locations in the IMU frames (obtained from the sensor to segment alignment) to accurately enforce the kinematic constraints. Additionally, we assume the sensor to segment alignment is constant; however, soft tissue motion causes the sensor to segment alignment to be time variant which leads to inaccurate corrections and thus the aforementioned bias or drift in hip joint angle estimates. To mitigate this effect, a joint axis correction measurement is employed at all times for the hip that mimics the ”soft” hinge constraint for the knee. However, because the hip exhibits full three degree of freedom rotations during gait, a much higher measurement variance is used (i.e., a ”softer” hinge constraint, see Tab. 4.1) for the hip joint axis correction compared to the knee. As with the knee, this measurement aids in constraining the estimated hip joint angles to anatomically realistic ranges while permitting three degree of freedom rotations. Note that no joint axis measurement corrections are used for the ankle, 1) because of the increased complexity of the ankle joint, and 2) because we observe that ankle joint angle estimates are typically constrained to anatomically realistic ranges with the joint center measurement corrections alone.

4.2.2 Human Subject Experiment

Human subject experiments were conducted previously by our collaborators in the M-Sense Research Group (directed by Dr. Ryan McGinnis) at the University of Vermont who permitted the use of their data for this study through an IRB-approved data sharing agreement with the University of Michigan. Those prior experiments performed by our collaborators are briefly reviewed here.

Twenty-three healthy adult subjects (inclusion: ability to perform basic tasks of daily living; exclusion: diagnosis of a balance or mobility impairment, inability to perform experimental tasks without assistance, opioid-dependence) participated in a University of

Vermont Institutional Review Board approved study. All subjects gave written informed consent before participating in the study. Subjects wore IMUs and motion capture (MOCAP) markers, as done for the stiff-legged walking experiment in Chapter 3 (refer to Fig. 3.2). Importantly, note that MOCAP markers are placed on bony landmarks as well as on the IMUs themselves, enabling two different methods for comparisons to MOCAP estimates (detailed later in Sec. 4.2.6). Subjects performed various activities of daily living in a laboratory including six walking gaits described below. MOCAP data and IMU data were collected synchronously at 100 Hz and 128 Hz, respectively. Data from these subjects was provided to the University of Michigan per the aforementioned data sharing agreement. Some data files from three subjects were either missing or created incorrectly, yielding data from twenty subjects analyzed in the present study (11 female, 9 male; mean (standard deviation) age 22.7 (±5.5), height 1.73(±0.09 m, height not available for one subject), mass 70.3 (±12.7) kg).

Of the many measurements in this large experiment, this chapter employs those occurring during: 1) the static standing calibrations (three seconds), 2) functional calibrations (set of movements including a modified version of the StarArc hip calibration movements [78, 91], knee flexions, and ankle flexions and rotations; performed for both sides), and 3) six constant-speed walking gaits on a treadmill. The treadmill walking gaits include separate trials of forward walking at three speeds (slow, normal, and fast), and backward walking, lateral left walking, and lateral right walking (all at self-selected speeds). Each of the walking trials is one minute. Additionally, for all trials, the subject began standing on the side rails of the treadmill and transitioned to the treadmill belt within the first five seconds. Only data after both feet left the railing is used to evaluate the performance of the ErKF method. For normal walking, only nineteen subjects are analyzed due to missing marker data for one subject. For fast and lateral left walking, only nineteen subjects are analyzed due to obvious belt speed changes during the trial for one subject each; thus these trials are not at constant speed as prescribed. For slow walking, only eighteen subjects are analyzed for reasons that follow. For one subject, the belt speed obviously changed during the trial. The other subject's data is excluded because they walked at a particularly slow speed (< 0.2 m/s), much slower than any other subject for that gait. This slower speed can yield a disproportionate impact on IMU-based kinematic estimates given the IMU specifications for this study because of low signal-to-noise ratio in IMU data and infrequent zero-velocity corrections (due to associated low stride frequency).

4.2.3 Kinematic Comparisons

To evaluate the performance of the ErKF method, we compare relevant kinematic measures estimated by the ErKF method to those estimated using two MOCAP-based methods. In particular, we compare three-dimensional joint angles for the hip, knee, and ankle as well as estimated stride length and step width. Note that we report differences in the estimation methods rather than accuracy since none of the methods measure ground truth skeletal motion. In order to facilitate direct comparison of the estimation methods, the same underlying skeletal model is used for both IMU-based and MOCAP-based methods. OpenSim's Gait2354 model [32, 92] is used as the base human skeletal model, but with the knee joint modified to allow three degrees of rotational freedom. This skeletal model is scaled for each subject using a procedure detailed later in Section 4.2.4. All joint angles are calculated according to the ISB recommended conventions [73, 93] with the modification proposed by Dabirrahmani and Hogg [94] and based on the anatomical frame conventions defined for the Gait2354 model.

In some trials, a simple offset (bias difference) is observed between the angles estimated from these two modalities (ErKF and MOCAP) despite otherwise highly consistent estimates of the underlying joint angle waveforms. Consequently, we also report the range of motion of the joint angles for each stride since 1) it is highly relevant for biomechanical studies, and 2) it is also a measure of consistency of the underlying waveforms. For each joint angle, the range of motion is calculated as the difference between the maximum and minimum value

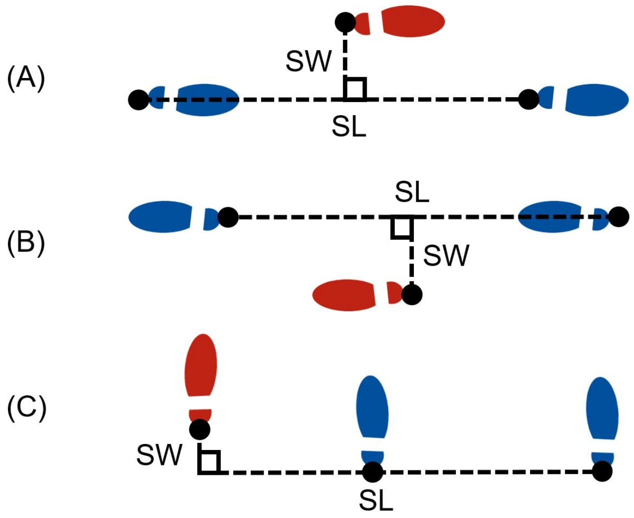

Figure 4.2: Stride length (SL) and step width (SW) definitions for forward walking (A), backward walking (B), and lateral walking (C). Shown in each subfigure are two consecutive right footfall locations (blue) with the intermediate left footfall location (red) for a subject traveling to the right. SL is the total horizontal displacement between consecutive footfalls of the same foot and SW is the orthogonal distance between the stride length vector and the intermediate footfall location of the opposite foot.

of the joint angle during that stride (i.e., between successive footfalls). Range of motion is not reported for any stride should any of the associated joint angle data be missing during that stride (e.g., due to marker occlusion). Additionally, if range of motion estimates are not reported for more than 30% of the strides during a trial, no summary statistics for range of motion are reported for that trial.

Stride length and step width are defined as in Section 3.2.3 and as illustrated in Figure 4.2 for forward, backward, and lateral walking. The first stride and last two strides represent transition strides during a trial, and they are not included in the reported stride length and step width results.

4.2.4 Calibration of ErKF and MOCAP Models

Both the IMU (ErKF) and MOCAP-based methods require determination of the mapping between the skeletal model and the IMUs and markers, respectively. MOCAP data during the static calibration and star calibration movements are used to determine both mappings as follows.

Joint centers of the hips, knees, and ankles are estimated during the static calibration as follows. Hip joint centers are calculated following Hara et al. [79] using the two ASIS and two PSIS markers to determine the pelvic frame and the average distance between the ASIS and medial malleoli to determine the leg length. The knee joint center is estimated following Davis et al. [89] as the midpoint of the lateral and medial femoral epicondyle markers. The ankle joint center is estimated following the recommendation of Siston et al. [95] as the midpoint of the lateral and medial malleoli markers.

OpenSim is then used to scale the model to each subject using marker data from the static calibration data, including the appended joint center estimates. OpenSim's scale tool also determines the location of each marker in its parent segment's frame using the same static calibration MOCAP data and the scaled skeletal model. Markers attached to each IMU (Fig. 3.2) are assigned to the IMU's respective parent segment. The rotation matrix from each segment's anatomical frame to the attached IMU's marker cluster frame, R_A^C, is determined from the marker locations in the parent segment's frame. To obtain the rotation matrix from the segment's anatomical frame to the IMU sense frame, the cluster to sensor frame rotation matrix for each segment, R_C^S, is calculated as detailed in [78] using data from the star calibration trial. The rotation matrix from the anatomical frame to the IMU sense frame, R_A^S, is then calculated as

$$R_A^S = R_C^S R_A^C \tag{4.1}$$

The location of each joint center in the IMU frame is determined from the static calibration trial as well as the location of heel markers in their respective foot IMU's frame. The rotation matrices between IMU and associated anatomical frames and the joint center locations in the IMU frames make up the sensor to segment calibration required for the seven-body ErKF method.

In summary, the calibration procedures described above establish the required mappings between sensors/markers and the underlying bones for both ErKF and MOCAP methods.

More precisely, for the ErKF method, these mappings are required inputs for the joint center and joint axis measurement corrections and critical to estimating segment poses (and thus the lower-limb kinematics) from the estimated IMU poses. In the MOCAP methods, these mappings are critical to estimating the skeletal poses from individually tracked markers.

4.2.5 Estimated Kinematics from the ErKF Method

The ErKF method yields estimates of major kinematical variables including the three-dimensional angles across all six skeletal joints as well as the stride length and step width. The method begins with estimating the positions and orientations of the IMUs (and thus the seven body segments) throughout each trial. MOCAP data is used to estimate the initial pose of each IMU (after both feet are off the rails) for establishing the initial states of the seven body segments for the ErKF. Still periods for all IMUs are determined using the same criteria as for the human subject attempting to walk with stiff legs in Chapter 3 (see Appendix B). Footfall instances are identified from IMU data during each detected stance. ZUPT and tilt measurement corrections are applied at identified footfall and still period instances, respectively. After IMU poses are estimated through the ErKF, the sensor to segment calibration is utilized to estimate the segment orientations from estimated IMU poses throughout the trial which are then used to estimate the three-dimensional joint angles across the hips, knees, and ankles. The joint angle estimates are then low-pass filtered using a zero-lag 4th order Butterworth filter at 6 Hz to parallel the filtering used for MOCAP estimates (described below), enabling direct comparison between the methods. To estimate stride metrics, each heel trajectory is estimated using its respective foot's estimated IMU pose combined with knowledge of the heel marker location with respect to the IMU frame (per the above calibration procedure). Estimated heel locations at identified footfalls are then used to calculate stride lengths and step widths as previously described in Section 4.2.3.

4.2.6 Estimated Kinematics from Two MOCAP Methods

In order to evaluate the success of ErKF method in estimating the aforementioned kinematical variables, we compare these estimates to those obtained from MOCAP. Estimates of stride length and step width are obtained from heel marker locations at IMU-identified footfall instances. To reduce noise in the measured trajectories, heel marker trajectories in the lab frame are low-pass filtered using a zero-lag 4^{th} order Butterworth filter at 6 Hz. Because some trajectories are missing data (i.e., due to marker occlusion), the filter is applied individually to each continuous segment of trajectory data. However, applying the filter to segments that are too short, may lead to erroneous results; thus, continuous segments shorter than 0.2 seconds are removed. Finally, short gaps in marker trajectories (less than 0.1 seconds) are filled with cubic splines. Recall that the ErKF method estimates positions relative to the treadmill belt frame (due to the ZUPT measurement model), whereas the MOCAP method estimates positions in the lab frame. To compare the results from these two measurement modalities, the MOCAP-based trajectories are converted to the treadmill frame as follows. The average velocity of the foot IMU markers during the first two stance phases is used as the estimated belt speed, which is assumed to remain constant. The distance the belt has traveled at each instant is then estimated by multiplying the estimated belt speed by time and that distance is added to the heel position (in the direction of travel) to estimate the heel trajectory in the belt frame. MOCAP estimates of stride length and step width are then estimated using the heel marker positions in the belt frame at the IMU-identified footfall instances.

Two different MOCAP-based methods are employed for estimating the joint angles during walking, using the markers shown in Figure 4.3. The first method, called the cluster method, provides estimates that more closely capture the motion of each IMU because it employs the marker data solely from the IMU-mounted markers (i.e., the marker clusters). In this method, the joint angles are estimated based solely on the estimated orientations of the IMU marker clusters. This method is expected to yield estimates nearer to the ErKF

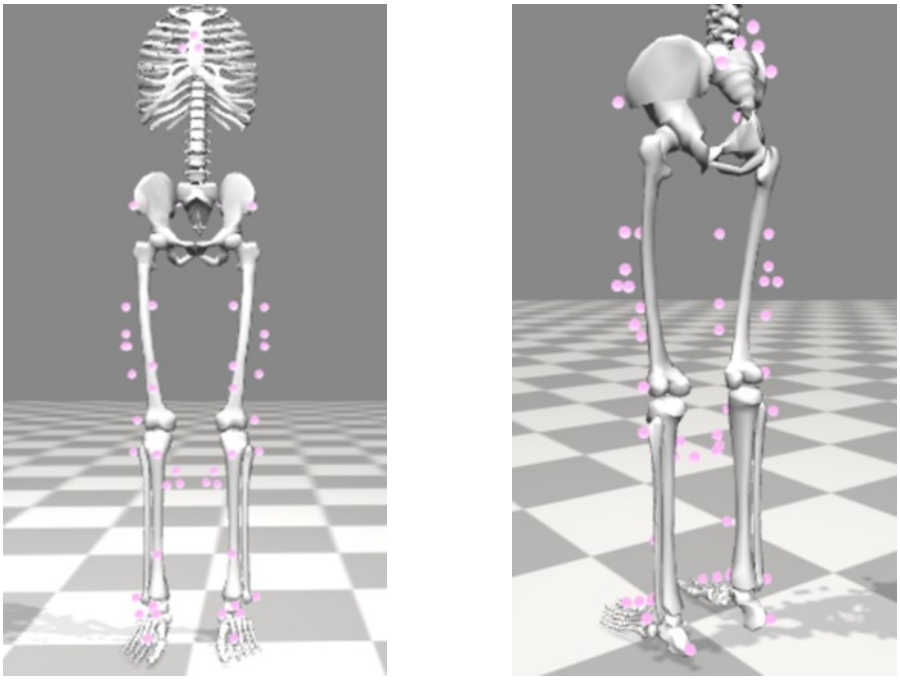
(A) (B)

Figure 4.3: Marker locations used for MOCAP comparisons ; visualized using OpenSim. (A) Front and (B) back views.

method because any soft tissue motion affects the motion of both the IMU and attached cluster markers equally. However, we do not expect them to be identical because this soft tissue motion does not affect each method's methodology equally (i.e., violations of rigid segment assumptions affect estimates differently in the two methods). The second method, called the inverse kinematics method, utilizes all marker locations shown in Figure 4.3 (i.e., both bony landmark and IMU markers) along with the scaled skeletal model (refer to Sec. 4.2.4) with its associated kinematic constraints to solve an inverse kinematics problem that estimates the lower-limb kinematics [32].

For both MOCAP-based methods, all IMU marker trajectories are low-pass filtered using a zero-lag 4^{th} order Butterworth filter at 6 Hz. Due to marker occlusion, segments of missing marker data are removed and repaired as described above for the heels. Individual details of these two MOCAP-based methods follow.

4.2.6.1. Cluster Method (Clust)

Whenever all three markers on an IMU are observable, their positions determine a cluster-based orientation of the IMU frame from which the corresponding body segment's orientation is estimated via the previously computed segment to cluster rotation matrix. Joint angles are then calculated from the estimated segment orientations. Note that if marker positional data of any of the six IMU markers adjacent a joint are missing, no angles across the intervening joint can be calculated at that time step.

4.2.6.2. Inverse Kinematics Method (IK)

The inverse kinematics tool within OpenSim is utilized to solve for all segment orientations using all markers. To ensure good inverse kinematics solutions, marker weightings are chosen such that marker errors generally remain below 1 cm RMS error and 4 cm maximum lower-limb marker error for each trial per recommendations in the OpenSim documentation [96]. Next, the joint angles are calculated from these segment orientations. Finally, the joint angle estimates are low-passed using a zero-lag 4^{th} order Butterworth filter at 6 Hz.

4.3 Results

We start by examining the results for a single representative subject during normal walking. This example is selected to highlight key points about the performance of the ErKF method. As done in Chapter 3 for the walker (Fig. 3.3 & 3.7), we compare the differences (compared to the cluster method) in joint angle estimates for one of the hips using raw integration of IMU data versus application of the ErKF method. The results in Figure 4.4 demonstrate no observable drift for the ErKF method in any of the three estimated joint angles (flexion/extension, FE; internal/external rotation, IE; abduction/adduction, AbAd; positive/negative reported values) for the left hip over the one minute trial while raw integration (i.e., without the ErKF) results in differences greater

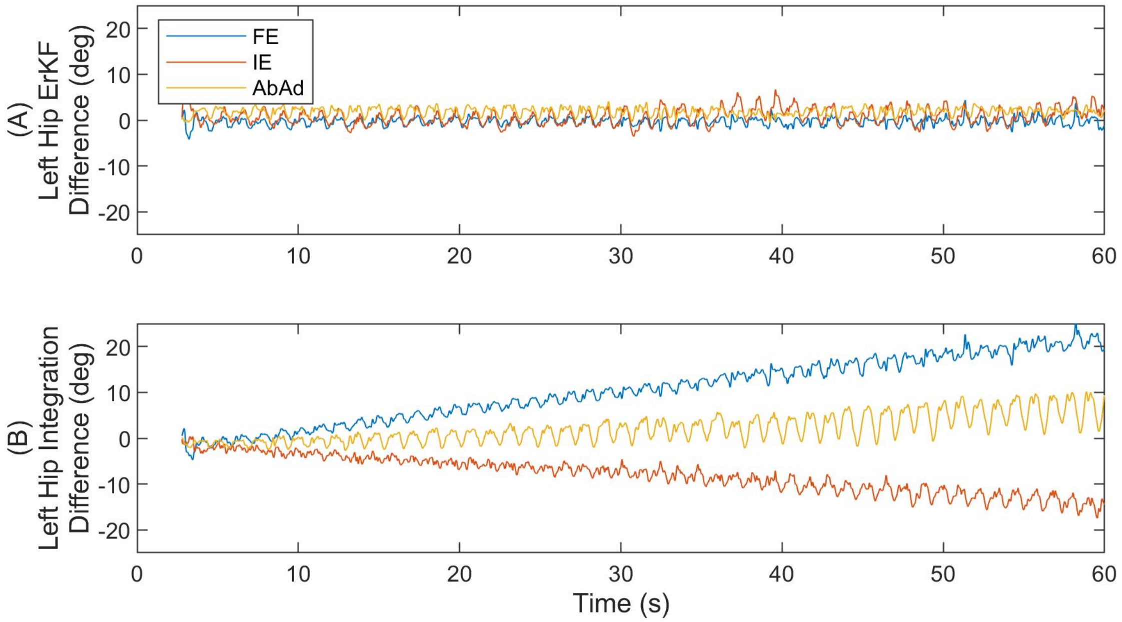

Figure 4.4: Representative left hip joint angle differences (IMU-cluster) versus time as estimated by (A) the ErKF method and (B) raw integration (no filtering). The three joint angles are flexion/extension (FE), internal/external rotation (IE), and abduction/adduction (AbAd)

than 20 deg over this same time due to drift. It is often recommended that a static period be utilized to correct for static bias in the angular rate signals [97], which would significantly reduce the rate of orientation drift due to raw integration. However, this strategy could not be employed in the present method because the validation data set does not include sufficiently long still periods to estimate the gyroscope bias. However, note the remarkable performance of the ErKF method in constraining integration drift despite not accounting for this gyroscope bias error.

We next more closely examine the estimated hip joint angles based on the ErKF (IMU) and cluster (MOCAP) based methods for this same subject and trial in Figure 4.5 but now for both the left (A) and right (B) hips. This figure provides evidence that errors in the sensor to segment alignment can significantly impact estimated joint angles; however, the ErKF method is still capable of overcoming such errors to estimate several key metrics. We arrive at this conclusion from the following observations. For the left hip (A), observe the excellent agreement between the ErKF and cluster method for all three joint angles over the entire trial (as expected from Fig. 4.4). However, for this very same subject and trial, the right hip (B) exhibits an offset between the two methods. This offset develops when the joint center measurement is utilized for a trial. Because: 1) this offset is influenced by the joint center measurement which relies on accurate estimates of the joint center locations in the IMU frames (obtained from the sensor to segment alignment) to accurately enforce the kinematic constraints, and 2) this offset can vary between hips for even the same subject and trial, it is likely that this offset originates from errors in the sensor to segment alignment parameters (determined using MOCAP data) as they are distinct for the two hips. To further support this claim (i.e., that the observable differences likely result from MOCAP-aided sensor to segment alignment rather than the ErKF method), note that the MOCAP-based FE estimates for the right hip appear to be qualitatively incorrect because they obviously oscillate between different extremes than the left hip and the peak extension for each stride (local minima in FE) is much larger than expected for healthy subjects in normal walking [20]. These obvious errors likely occur from errors in marker placement and model scaling assumptions, thus resulting in sensor to segment alignment errors. Because no sensor to segment alignment method is immune to errors (albeit to varying degrees), it is critical that the ErKF method still provide meaningful estimates even in the presence of such errors. Thus, we do not exclude any trials from our analysis for obvious errors in sensor to segment alignment. Additionally, observe that despite these errors, estimates from the ErKF method do not rapidly diverge like estimates from raw integration. Thus, errors in sensor to segment alignment may still lead to converged estimates, but with systematic offsets between methods due to the errors in sensor to segment alignment which affect both ErKF and MOCAP estimates (albeit affecting these methods differently).

Such offsets are commonly observed in this study, but vary in size depending on the subject and joint angle. Typically the offsets (when they do arise) are smaller for FE and AbAd angles (< 10 deg) than for IE angles (< 30 deg) as shown in Figure 4.5B. Importantly, such systematic offsets do not preclude meaningful and useful results. For example, Figure

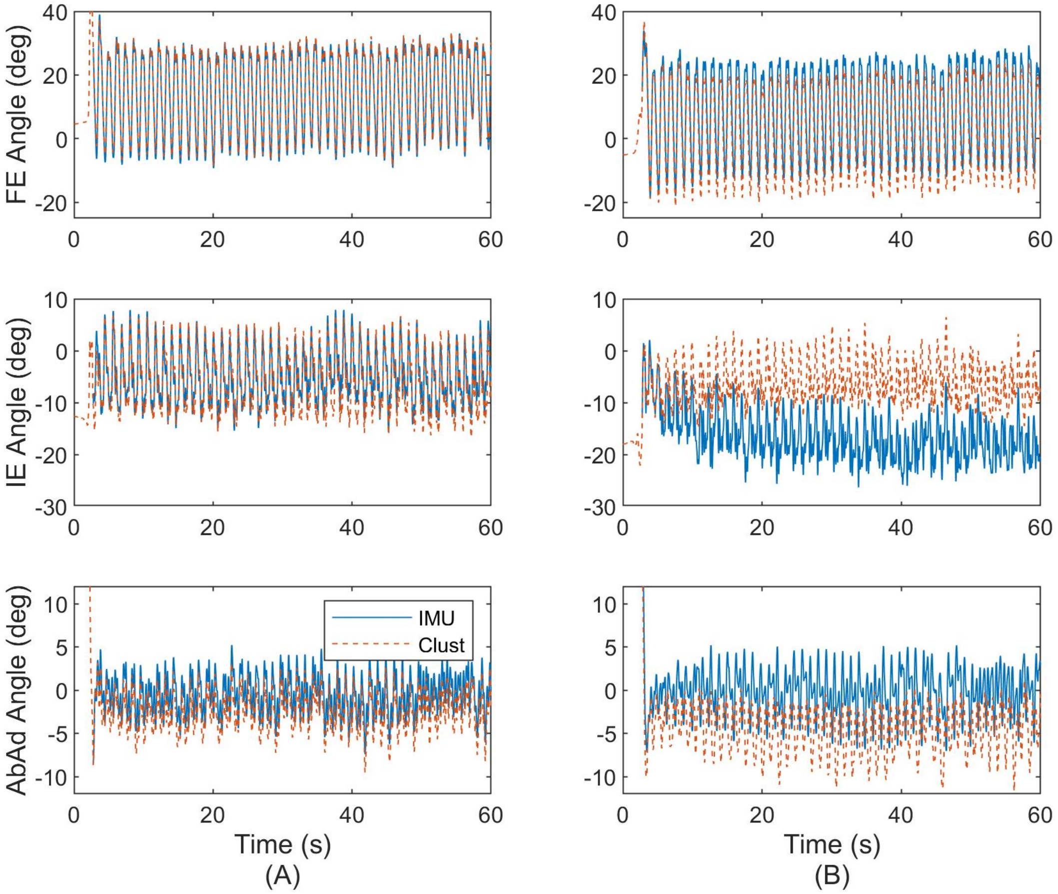

Figure 4.5: Comparison of estimated hip joint angles for representative subject using for the left (A) and right (B) hips. Comparison is between ErKF (IMU) and cluster (Clust) methods.

4.6, which shows the right hip's estimated IE angle over two stride cycles (zoom in from Fig. 4.5B), demonstrates that while an offset between the estimation methods develops, the same waveform for this joint angle is captured by the two methods. Thus, one can successfully estimate *range of motion* even in the cases where offsets arise due to poor MOCAP results. Consequently, we also report later the differences in (stride to stride) estimates of range of motion for each method as a measure of how well the captured waveforms compare between methods. Importantly, we emphasize that range of motion is a very useful kinematic measure by itself in many biomechanical contexts (e.g., [98–100]).

While we observe that the ErKF performs well for this representative subject for normal walking, it is also critical to evaluate the method's performance for the other types

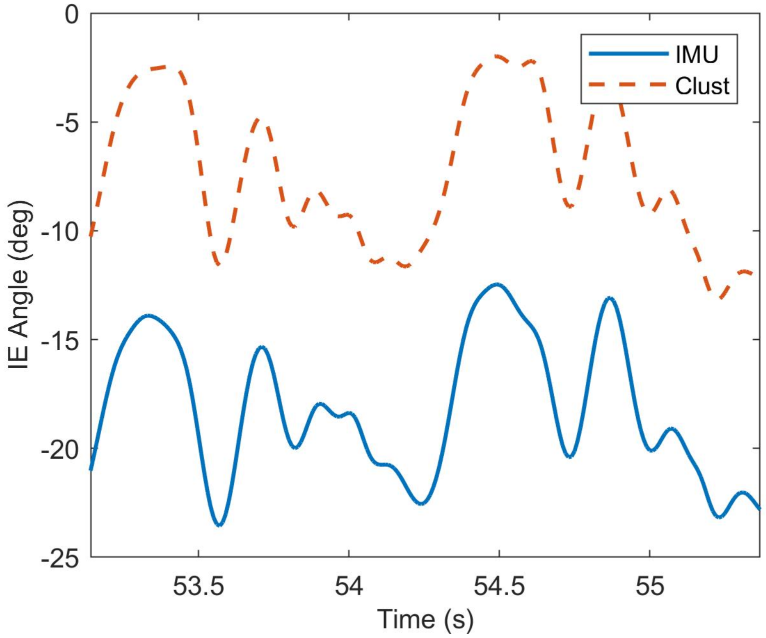

Figure 4.6: Magnified comparison of estimated right hip IE angle for representative subject in normal walking over two gait cycles.

of gait included in the experiments. Figure 4.7 illustrates the left hip joint angle trajectory estimates for two stride cycles of normal treadmill walking (A) and walking laterally left (B) using the three different estimation methods for the same representative subject. These two gaits represent limiting cases of gait types in this dataset where one (normal walking) is predominantly an FE motion for the hip and the other (lateral walking) is predominantly an AbAd motion for the hip. The left hip is chosen here because it enables direct evaluation of the performance of the ErKF without the confounding effects of likely sensor to segment alignment errors (per the previous results). Observe the remarkably close agreement between the ErKF and cluster methods for both types of gait, especially for FE and AbAd angles. Recall that for all types of gait, the ErKF method imposes a hinge-like measurement update on the hip at all time points, but with a large measurement uncertainty to acknowledge that the hip is often not acting like a hinge. These results confirm that with carefully chosen large measurement uncertainty (i.e., with a soft constraint), the hip joint angles are estimated similarly between the methods even for lateral walking gait where the hip rotation is not dominated by flexion and extension. Additionally, the inverse kinematics method yields a similar waveform compared to the other two estimation methods, especially for the degree of freedom that dominates each type of gait (FE for normal walking, AbAd for lateral walking). Consequently, the three estimation methods may yield consistent estimates of range of motion for many of the joint angles and across all types of gait; refer to Appendix C for example joint angle estimates over two stride cycles for all six gait types for this same representative subject. Again we emphasize the important role of quantifying range of motion for biomechanical studies. The residual offsets could be caused by soft tissue artefacts, sensor to segment alignment errors, MOCAP errors, and/or the imposition of the hinge-like joint measurement.

We next report the performance of the ErKF method across all joints (hips, knees, and ankles) and across all twenty subjects performing all six types of gait. First, we focus on the performance of the ErKF method compared to the cluster method for joint angles. The RMS difference between the ErKF and cluster estimate of each joint angle is calculated for each subject and trial. Table 4.2 reports the mean and standard deviation of the RMS differences across all subjects and separately for each type of gait. The green, yellow, and red highlighting denotes mean RMS differences less than 5 deg, less than 10 deg, and greater than 10 deg, respectively. Note that mean RMS differences are generally less than 5 degrees for FE (dorsiflexion/plantarflexion (DP) for ankle) and AbAd (inversion/eversion (InEv) for ankle) across all joints and across all types of gait. By contrast, mean RMS differences are typically higher for IE joint angles across all gait types, except for the ankle.

Next, we evaluate the performance of the ErKF method compared to the inverse kinematics method for joint angle estimates. Table 4.3 reports the RMS differences between the ErKF and inverse kinematics estimate of each joint angle across all subjects and separately for each type of gait. The same highlighting used previously enables quick assessment of the levels of agreement of these two estimation methods. Note that mean RMS differences generally remain less than 5 degrees for AbAd (InEv for ankle) across all

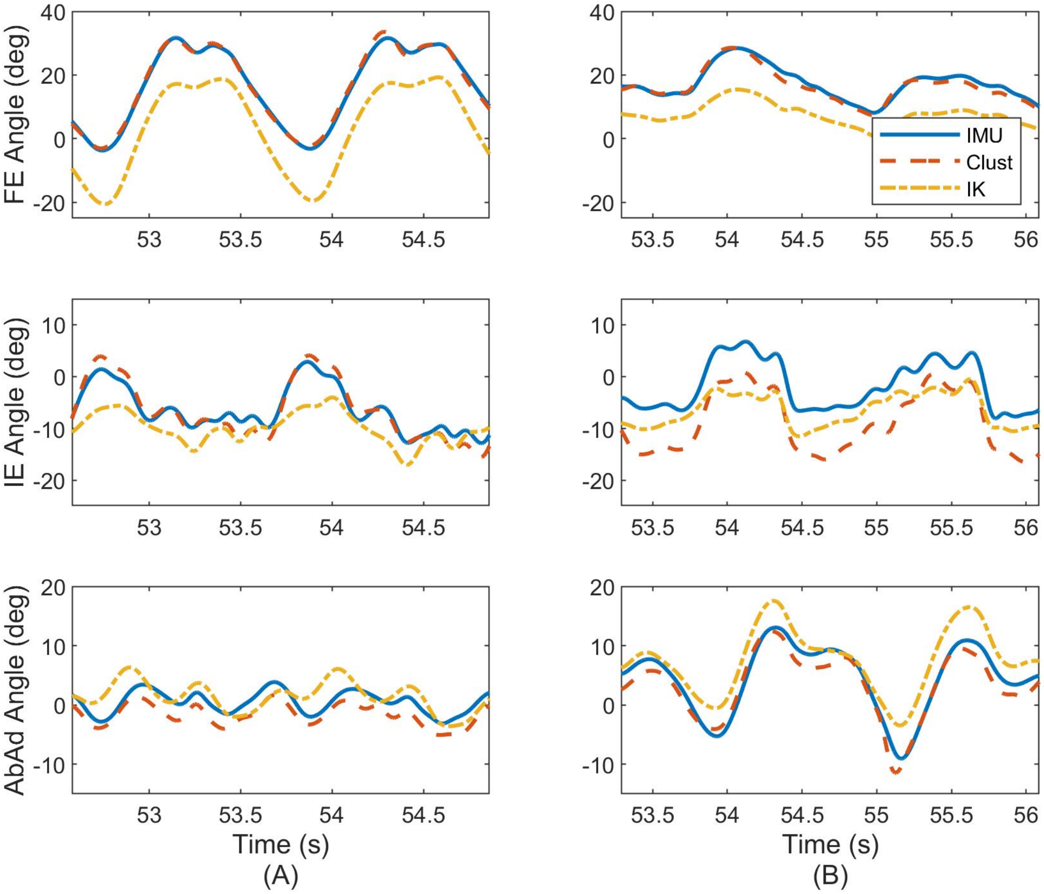

Figure 4.7: Representative hip joint angle estimates over two stride cycles for normal treadmill walking (A) and lateral left shuffle (B). Estimates are made utilizing ErKF (IMU), cluster (Clust), and inverse kinematics (IK) methods.

joints and across all types of gait. By contrast, mean RMS differences are typically higher for FE (DP for ankle) and IE joint angles across all gait types, except FE for the knee and IE for the ankle.

As previously mentioned, all three estimation methods are expected to yield comparable values for the range of motion across all angles, joints, subjects, and gait types, and even in cases where bias differences arise between methods. Evidence to support this claim is provided in the following two tables starting with Table 4.4 that compares the estimates from the IMU ErKF method and MOCAP cluster method. This table reports the mean (and standard deviation) of the (stride by stride) RMS differences in range of motion for

Table 4.2: Comparisons of joint angles with Cluster Method. Mean (Standard Deviation) of RMS difference (IMU-Cluster) in estimates for each joint angle. All angles in degrees. Green, yellow, and red highlights indicate mean values < 5 deg, < 10 deg, and ≥ 10 deg, respectively. Results segmented by type of walking gait; namely normal forward (Normal), fast forward (Fast), slow forward (Slow), backward (Back), lateral left (Left), and lateral right (Right). Joint angles are flexion/extension (FE), internal/external rotation (IE), abduction/adduction (AbAd), dorsiflexion/plantarflexion (DP), and inversion/eversion (InEv). R and L prepended to joint names indicate right and left side, respectively.

	Normal	Fast	Slow	Back	Left	Right
RHip FE	2.54(1.23)	2.28(0.86)	2.21(0.80)	2.34(1.18)	2.80(1.89)	2.94(1.94)
LHip FE	2.17(0.89)	2.25(0.83)	2.40(1.44)	2.61(1.22)	3.00(1.61)	2.63(1.41)
RKnee FE	3.13(1.06)	3.37(0.83)	3.07(1.21)	3.10(1.13)	3.77(1.96)	3.65(1.78)
LKnee FE	3.16(1.05)	3.52(1.37)	2.99(1.17)	3.07(1.33)	3.71(1.13)	3.05(1.18)
RAnkle DP	4.24(1.81)	3.99(1.70)	5.03(2.04)	5.50(1.80)	6.32(1.98)	6.00(1.89)
LAnkle DP	3.00(1.23)	3.13(1.15)	3.41(1.22)	2.87(1.51)	3.31(1.63)	3.02(1.53)
RHip IE	7.40(3.56)	6.08(3.00)	7.40(5.75)	10.55(9.44)	8.30(9.52)	9.44(8.45)
LHip IE	7.47(7.60)	6.57(4.68)	11.97(12.76)	11.45(10.89)	10.35(7.83)	8.17(7.89)
RKnee IE	8.83(3.88)	7.96(4.00)	8.21(3.60)	8.48(2.95)	6.87(3.28)	7.34(3.47)
LKnee IE	7.29(6.96)	6.74(6.59)	7.63(8.05)	8.29(7.27)	9.83(8.76)	9.38(8.12)
RAnkle IE	2.72(1.10)	2.40(0.85)	3.83(1.90)	2.81(1.38)	3.74(1.82)	4.15(1.79)
LAnkle IE	3.14(1.76)	2.58(1.35)	3.85(1.75)	3.10(1.75)	3.19(1.95)	3.29(1.77)
RHip AbAd	4.15(2.13)	3.49(1.69)	3.52(2.25)	3.85(3.02)	3.43(2.70)	4.04(3.36)
LHip AbAd	3.45(2.05)	3.40(1.66)	4.07(2.32)	3.67(1.76)	4.09(1.93)	2.92(1.28)
RKnee AbAd	4.62(3.40)	4.52(3.36)	4.24(3.70)	3.38(3.40)	3.16(2.91)	3.64(3.54)
LKnee AbAd	4.60(1.68)	4.46(1.84)	4.31(1.64)	3.85(1.74)	3.62(1.56)	3.62(1.64)
RAnkle InEv	2.61(0.79)	2.72(0.80)	2.70(1.00)	1.96(0.68)	2.42(0.66)	2.58(0.67)
LAnkle InEv	2.40(0.94)	2.35(1.16)	2.51(0.88)	2.00(1.07)	2.08(0.68)	2.27(0.89)

each joint angle across all subjects and separately for each type of gait. In the vast majority of trials, frequent marker occlusion (especially of shank IMU cluster markers) precluded estimates of knee and ankle range of motion using the cluster method. Thus, we only report range of motion differences for the hip joint angles here. Observe that mean RMS range of motion differences all remain below 5 degrees for all hip angles.

Next, we compare the range of motion estimates of the ErKF method and the inverse kinematics method in Table 4.5. This table reports the mean (and standard deviation) of the (stride by stride) RMS differences in range of motion for each joint angle across all subjects and separately for each type of gait. Unlike the cluster method, the inverse kinematics method is capable of estimating kinematics even when markers are occluded. Thus, range

Table 4.3: Comparisons of joint angles with Inverse Kinematics Method. Mean (Standard Deviation) of RMS difference (IMU-IK) in estimates for each joint angle. All angles in degrees. Green, yellow, and red highlights indicate mean values < 5 deg, < 10 deg, and ≥ 10 deg, respectively.Results segmented by type of walking gait; namely normal forward (Normal), fast forward (Fast), slow forward (Slow), backward (Back), lateral left (Left), and lateral right (Right). Joint angles are flexion/extension (FE), internal/external rotation (IE), abduction/adduction (AbAd), dorsiflexion/plantarflexion (DP), and inversion/eversion (InEv). R and L prepended to joint names indicate right and left side, respectively.

	Normal	Fast	Slow	Back	Left	Right
RHip FE	7.03(4.37)	7.16(4.21)	5.96(4.49)	6.33(4.53)	5.67(4.52)	6.03(4.73)
LHip FE	7.23(4.03)	7.00(3.71)	6.75(3.85)	6.97(4.55)	6.33(4.09)	6.73(4.46)
RKnee FE	4.36(2.14)	4.74(2.10)	4.16(2.26)	4.35(1.89)	4.50(2.14)	4.64(2.09)
LKnee FE	3.79(1.26)	4.14(1.26)	3.37(1.54)	4.18(1.48)	4.15(1.63)	3.84(1.70)
RAnkle DP	5.41(2.98)	5.48(3.07)	5.40(2.92)	5.20(2.64)	4.33(2.46)	4.92(2.61)
LAnkle DP	5.28(2.14)	5.64(2.22)	4.76(2.35)	3.52(1.87)	4.62(4.13)	3.59(1.77)
RHip IE	7.43(3.59)	6.19(2.55)	8.50(6.43)	11.26(10.24)	9.58(8.54)	11.03(9.44)
LHip IE	8.56(7.43)	7.21(4.95)	13.54(13.34)	12.67(11.30)	11.61(9.19)	9.28(8.41)
RKnee IE	5.91(2.71)	5.66(2.34)	5.98(3.01)	6.12(3.30)	5.81(3.27)	5.83(3.08)
LKnee IE	7.32(5.20)	7.70(5.11)	6.87(5.93)	7.43(5.94)	8.62(6.79)	7.66(6.01)
RAnkle IE	4.23(2.32)	4.49(1.28)	4.39(2.06)	3.90(2.49)	4.81(3.30)	3.89(2.55)
LAnkle IE	4.76(2.68)	5.35(2.72)	4.49(2.43)	3.73(2.30)	4.87(3.93)	4.17(1.82)
RHip AbAd	4.74(2.04)	4.53(1.77)	4.33(1.35)	3.88(1.96)	3.39(1.61)	4.51(1.79)
LHip AbAd	4.37(1.47)	4.44(1.47)	4.64(1.78)	4.00(1.41)	4.27(1.65)	3.52(1.63)
RKnee AbAd	3.99(1.53)	4.34(1.66)	3.17(1.22)	2.65(1.28)	2.65(1.63)	2.67(1.35)
LKnee AbAd	3.90(2.06)	3.72(1.81)	3.26(1.88)	3.73(1.97)	2.96(1.61)	3.55(2.06)
RAnkle InEv	4.56(1.32)	4.94(1.51)	4.88(1.32)	5.79(1.57)	6.27(1.22)	6.07(1.80)
LAnkle InEv	4.70(1.50)	5.16(1.72)	4.42(1.18)	4.71(1.68)	5.35(1.89)	5.48(2.11)

Table 4.4: Comparisons of range of motion with Cluster Method. Mean (Standard Deviation) of RMS difference (IMU-Cluster) in range of motion estimates. All angles in degrees. Green, yellow, and red highlights indicate mean values < 5 deg, < 10 deg, and ≥ 10 deg, respectively. No results reported for knees or ankles because frequent marker occlusion prevented Cluster estimates. Results segmented by type of walking gait; namely normal forward (Normal), fast forward (Fast), slow forward (Slow), backward (Back), lateral left (Left), and lateral right (Right). Joint angles are flexion/extension (FE), internal/external rotation (IE), abduction/adduction (AbAd), dorsiflexion/plantarflexion (DP), and inversion/eversion (InEv). R and L prepended to joint names indicate right and left side, respectively.

	Normal	Fast	Slow	Back	Left	Right
RHip FE	1.22(0.36)	1.60(0.69)	1.35(0.57)	2.26(0.85)	2.39(1.89)	1.58(0.58)
LHip FE	1.69(1.54)	1.69(1.32)	3.59(4.82)	2.74(2.31)	2.19(1.23)	1.86(1.20)
RHip IE	1.98(0.99)	1.98(0.71)	2.41(0.87)	2.53(1.06)	3.28(1.60)	3.22(1.53)
LHip IE	2.15(0.80)	2.10(0.64)	2.41(0.92)	3.15(1.04)	2.92(1.22)	2.54(1.04)
RHip AbAd	3.14(1.84)	2.98(2.08)	2.51(1.61)	2.27(0.98)	2.97(1.22)	2.26(0.96)
LHip AbAd	3.29(3.19)	2.24(1.75)	4.24(4.99)	3.02(3.27)	2.58(1.97)	2.77(1.21)

Table 4.5: Comparisons of range of motion with Inverse Kinematics Method. Mean (Standard Deviation) of RMS difference (IMU-IK) in range of motion estimates. All angles in degrees. Green, yellow, and red highlights indicate mean values < 5 deg, < 10 deg, and ≥ 10 deg, respectively. Results segmented by type of walking gait; namely normal forward (Normal), fast forward (Fast), slow forward (Slow), backward (Back), lateral left (Left), and lateral right (Right). Joint angles are flexion/extension (FE), internal/external rotation (IE), abduction/adduction (AbAd), dorsiflexion/plantarflexion (DP), and inversion/eversion (InEv). R and L prepended to joint names indicate right and left side, respectively.

	Normal	Fast	Slow	Back	Left	Right
RHip FE	4.17(2.40)	4.61(2.72)	3.26(1.85)	3.70(2.38)	2.13(0.88)	2.44(0.90)
LHip FE	4.14(2.07)	4.56(2.33)	4.59(4.25)	2.94(1.99)	2.33(0.99)	2.21(1.02)
RHip IE	5.22(2.75)	5.53(2.50)	4.84(2.89)	4.05(2.17)	5.92(3.58)	4.20(2.26)
LHip IE	4.77(2.71)	5.28(2.21)	4.49(2.77)	4.13(2.42)	3.69(1.43)	5.93(2.82)
RHip AbAd	3.48(2.20)	4.40(2.66)	3.29(2.30)	3.28(1.58)	2.43(1.51)	2.36(1.45)
LHip AbAd	4.30(1.88)	5.71(2.42)	4.41(2.42)	4.00(2.43)	2.74(2.40)	2.69(1.39)
RKnee FE	4.62(2.65)	4.37(2.65)	4.53(2.71)	3.01(1.88)	2.94(1.84)	2.88(1.08)
LKnee FE	3.44(2.22)	2.89(2.18)	3.61(2.12)	2.92(1.50)	3.14(1.10)	2.57(0.98)
RKneeIE	4.88(2.60)	5.43(3.41)	3.14(2.15)	3.61(1.74)	4.21(1.44)	3.90(1.61)
LKnee IE	4.71(2.05)	5.16(1.74)	3.16(1.43)	3.28(1.39)	4.85(2.06)	4.61(1.64)
RKnee AbAd	5.77(4.36)	6.85(5.11)	4.00(2.66)	2.35(1.52)	1.51(0.87)	1.89(0.80)
LKnee AbAd	3.70(3.01)	3.81(2.69)	3.66(2.67)	2.71(1.47)	2.05(1.09)	1.99(0.82)
RAnkle DP	4.49(2.29)	5.38(2.26)	3.63(2.10)	2.50(1.23)	2.33(0.65)	2.51(1.54)
LAnkle DP	5.26(2.80)	6.21(2.93)	3.05(1.71)	1.84(0.87)	5.36(11.45)	2.14(1.07)
RAnkle IE	8.21(3.18)	9.33(2.78)	6.71(2.77)	4.05(1.39)	3.71(1.59)	3.15(1.81)
LAnkle IE	8.90(3.89)	10.57(3.05)	6.86(3.01)	3.33(1.74)	5.69(11.62)	2.76(1.76)
RAnkle InEv	3.79(1.72)	3.22(1.16)	4.89(1.99)	5.65(2.49)	6.10(2.73)	7.21(3.22)
LAnkle InEv	5.27(2.75)	4.52(2.57)	5.77(3.27)	5.62(2.45)	7.57(3.45)	5.66(2.31)

of motion is successfully estimated for all joint angles in each trial as reflected in Table 4.5. From this table, observe that the mean RMS range of motion differences generally remain below 5 degrees for the hip and knee across all types of gait. Importantly, also note that generally larger differences in Table 4.5 (comparison to inverse kinematics method) versus those of Table 4.4 (comparison to cluster method) result from differences between the two MOCAP-based methods themselves (e.g., as observed in offsets between Clust and IK estimates in Fig. 4.7). Additionally, the larger differences in ranges of motion for the ankle angles versus those for the knee and hip may derive from increased complexity of the ankle joint in the Gait2354 model used for the IK estimates versus the simpler model used in the ErKF and cluster methods.

Table 4.6: Comparisons of stride parameters with MOCAP. Mean (standard deviation) of RMS difference (IMU-MOCAP) in estimates of stride length (SL) and step width (SW). Additionally, mean (standard deviation) of the mean SL, SW, and belt speed (all estimated by MOCAP) across all subjects. Finally, mean RMS differences as percentage of the mean SL and SW (% Diff). All distances in m, speeds in m/s. Results segmented by type of walking gait; namely normal forward (Normal), fast forward (Fast), slow forward (Slow), backward (Back), lateral left (Left), and lateral right (Right). NA indicates not applicable because mean value near zero.

	Normal	Fast	Slow	Back	Left	Right
SL RMS Diff	0.07(0.03)	0.05(0.02)	0.16(0.05)	0.11(0.05)	0.07(0.03)	0.06(0.02)
Mean SL	1.09(0.15)	1.40(0.17)	0.84(0.15)	0.62(0.15)	0.48(0.08)	0.46(0.08)
% Diff SL	6.0%	3.4%	19.1%	17.6%	15.5%	13.3%
SW RMS Diff	0.05(0.02)	0.05(0.02)	0.07(0.04)	0.12(0.06)	0.10(0.08)	0.09(0.05)
Mean SW	0.12(0.03)	0.11(0.03)	0.13(0.03)	0.15(0.03)	0.01(0.02)	0.00(0.02)
% Diff SW	40.4%	43.1%	57.4%	80.8%	NA	NA
Belt Speed	0.86(0.17)	1.32(0.21)	0.47(0.09)	0.43(0.08)	0.39(0.07)	0.38(0.08)

Finally, we compare key stride metrics, namely stride length (SL) and step width (SW) by the ErKF method to those estimated using the MOCAP heel trajectories. Table 4.6 reports both the mean (and standard deviation) SL and SW from MOCAP as well as the mean (and standard deviations) of the RMS differences in SL and SW between the two methods across all subjects and separately for each gait type. Mean RMS differences in stride length are 0.07 and 0.05 m (6% and 3.4% of the mean), respectively for normal and fast walking. Mean RMS differences in stride length for both lateral walks also remain below 0.08 meters (below 16% of the mean), noting the mean stride length is much lower than for the forward walks. For normal and fast walking, mean RMS differences in step width are 0.05 meters (~ 45% of the mean). Note that for both stride length and step width, mean RMS differences for forward and backward walking are much lower for the faster gait speeds (> 0.8 m/s) compared to the slower speeds (< 0.5 m/s).

4.4 Discussion

This chapter extends the ErKF method developed in Chapter 3 to a full (seven-body) model of the human lower limbs and evaluates its performance on a variety of gait types. The results demonstrate that the ErKF method estimates important kinematic parameters comparable to those estimated using two different MOCAP methods across six different walking gaits. In general, the method yields small RMS differences (< 5 deg) in estimates of FE and AbAd joint angles (DP and InEv for ankle) across all joints and gait types with low offsets between the ErKF and cluster methods (refer to Tab. 4.2). Higher offsets typically occur in IE joint angle estimates; however, these higher IE offsets vary greatly between subjects as evidenced by the high standard deviations reported in Table 4.2 for IE angles compared to the other joint angles. Additionally, over these one minute trials, these higher IE offsets generally stabilize to be near-constant and with the joint angle's waveform still estimated similarly (for example, Fig. 4.6) as evidenced by the relatively small (generally < 5 deg) range of motion differences (between ErKF and both MOCAP methods) for these same IE angles, especially for the hips and knees (refer to Tabs. 4.4 & 4.5). Additionally, note that while RMS differences in IE joint angle estimates are generally higher than other degrees of freedom for the ErKF method (refer to Tab. 4.2), this trend is typical of IMU-based lower-limb kinematic estimation methods, likely due (at least in part) to low signal-to-noise ratio in the transverse plane kinematics [101]. Thus, researchers must exercise caution when interpreting IE estimates obtained from IMU-based methods (including the method presented in this chapter), especially where RMS differences (or errors) in these estimates are large compared to the expected ranges of motion. Comparison of joint angle estimates obtained via the ErKF method to estimates obtained via inverse kinematics (MOCAP) generally yields greater RMS differences than comparison to the cluster method (refer to Tab. 4.3). These larger differences are likely driven by several factors including systematic differences due to movement of the underlying bones relative to the sensors/markers. RMS differences in stride length remain below 0.08 m for normal, fast, and both lateral walking gaits with mean RMS differences in step width of 0.05 m for normal and fast walking (refer to Tab. 4.6). Importantly, recall that MOCAP estimates of stride length for this study rely on accurate estimates of belt speed. While not reported here, we observe that differences between belt speeds estimated via MOCAP (as used in this chapter) and those reported by the treadmill (which were not available for all trials) are often on the order of 0.03 m/s. Thus errors in MOCAP-estimated belt speed may account for a significant portion of differences in estimated stride length between the ErKF method and MOCAP in this study. In rare cases, joint angle waveforms between different methods did not clearly converge to a steady offset over the one minute trials. However, while not reported in the results, we observe these cases of large drift arise for particular subjects rather than to gait types, indicating that poor sensor to segment alignment may be primarily responsible. Additionally, we observe that trials with low offsets in joint angles typically exhibited smaller differences in stride metric estimates.

In addition to comparing joint angle estimates, we also compare joint angle range of motion estimates between the ErKF and MOCAP methods. Range of motion, and particularly changes in range of motion, have demonstrated significance in biomechanical studies in a variety of contexts as emphasized by a few examples. Devita and Hortobagyi [102] evaluate hip and ankle flexion range of motion during stance for walking and find significant differences between elderly and young populations (3.3 deg for hip and -2.7 for ankle, elderly-young). For their experiment, all subjects walked at approximately 1.5 m/s which is closest to the fast walking trials in the present study. Qu and Yeo [100] assess kinematic differences due to fatigue with and without load. They find that fatigue increases range of motion in the hip and knee by 1.3 and 1.9 deg, respectively. Sofuwa et al [103] examine differences in various kinematic parameters between a healthy group and Parkinsons's disease patients during gait. They find that the healthy group exhibits 4.8 and 4.0 deg greater ankle DP range of motion during the pushoff and swing phases, respectively. Carmo et al. [104] evaluate range of motion for post-stroke patients and healthy controls during self-selected gait and find many statistically significant differences between affected sides, unaffected sides, and healthy controls. For example, they find that knee flexion range of motion is 17.4 and 20.0 degrees lower for stroke patient's affected side compared to the unaffected side and healthy controls, respectively. Because of the demonstrated usefulness in measuring range of motion for biomechanical studies using MOCAP methods highlighted above, we can expect that the ErKF method will prove valuable for similar studies if it can estimate range of motion and also changes in range of motion with sufficient resolution. While the present study did not directly measure resolution in range of motion estimates, the favorable comparisons between ErKF and MOCAP estimates of range of motion suggest the ErKF may indeed have sufficient resolution as explained next.

The ErKF method demonstrates average RMS differences for hip FE, IE, and AbAd range of motion less than 2, 3, and 4 deg, respectively compared to the cluster method during normal walking (refer to Tab. 4.4; recall cluster estimates of range of motion are not available for comparison on the knees and ankles due to frequent marker occlusion). Compared to the inverse kinematics method, range of motion differences are slightly higher, but still generally below 5 degrees across joints and gait types (refer to Tab. 4.5). These findings establish that the ErKF method yields very similar estimates of range of motion compared to MOCAP. Importantly, note also that the differences between the ErKF and MOCAP methods in this study are similar to and often smaller than the changes in range of motion observed in the studies highlighted. This fact supports the claim that the ErKF method should also possess sufficient resolution in range of motion estimates to support future studies. In other words, the ErKF method shows great promise for detecting meaningful biomechanical differences in range of motion for future studies outside (and within) the laboratory.

The differences between ErKF and MOCAP-based estimates of joint angles and ranges of motion in this study are comparable to prior IMU-based methods that primarily focused on normal walking. Importantly though, the present method advances well beyond the prior methods in: 1) estimating three-dimensional joint angles across all lower-limb joints, 2) succeeding over a wide variety of gait types (beyond normal walking), and/or 3) eliminating reliance on prior assumptions. For example, Adamowicz et al. [78], whose data come from the same experiments summarized here, present a method specific for the hip joint and observe mean RMS differences in hip FE, IE, and AbAd of 8.6, 10.0, and 8.0 deg, respectively during normal walking when compared to a similar cluster-based MOCAP method. However, the present ErKF method demonstrates superior mean RMS differences for hip FE, IE, and AbAd of 2.4, 7.4, and 3.8 deg, respectively for normal walking (refer to Tab. 4.2). Weygers et al. [105] develop a method specific for the knee joint and observe RMS differences from MOCAP less than 5 deg during walking for knee Euler angles (as opposed to anatomical angles). While acknowledging differences in using Euler angles versus anatomical angles, similar differences (< 5 deg) arise in the ErKF method for the knee during normal walking for FE and AbAd, but not for IE (6.6 deg); refer to Table 4.3. Importantly, these prior studies offer ”single-joint” methods as opposed to the multi-joint method developed herein.

The performance of the present ErKF method also compares well to that of prior multi-joint methods, but also removes assumptions employed in those prior methods and/or reliance on magnetometer data. Teufl et al. develop a seven-body model of the lower limbs and compare IMU-derived results with those from MOCAP using both cluster and inverse kinematics methods for overground walking [16, 67] and for short dynamic movements [85]. For normal walking, they observe smaller RMS differences in joint angles than reported in this study. For example, they observe RMS differences in FE (or DP), IE, and AbAd (or InEv) across all joints up to 1.6, 2.3, and 1.6 deg, respectively compared to a similar cluster method and up to 5.4, 5.5, and 4.2 deg, respectively compared to a MOCAP method relying on bony landmarks. In the current study, RMS differences are up to 4.2, 8.8, and 4.6, deg, respectively compared to the cluster method (Tab. 4.2) and up to 7.2, 8.6, and 4.7 deg, respectively compared to the inverse kinematics method which primarily relies on bony landmarks (Tab. 4.3). They also report stride length and step width estimates during walking [67], having RMS differences of 0.04 m and 0.03 m, respectively. In the present ErKF study for normal walking SL and SW differences are 0.07 and 0.05 m, respectively; refer to Table 4.6. However, for these stride metric estimates, their study is conducted overground and thus their comparisons are not affected by potential errors in MOCAP-estimated belt speed like this ErKF study. While the differences in joint angle and stride metric estimates reported by Teufl et al. are somewhat smaller than those observed in this ErKF study, their method also relies critically on a level ground assumption (for both footfall identification and to correct drift errors) which is not assumed in the present ErKF method. Thus, while the present method can be used on level or uneven terrain (i.e., outdoor environments), the method of [16] is restricted to level terrain (i.e., likely restricted to indoor, single-level environments). Additionally, their process model assumes constant linear acceleration and angular velocity (with IMU measurements being used in the measurement model) and thus it may not be suited for more dynamic movements. Finally, this prior method is not evaluated for any gait types other than normal speed walking. McGrath and Stirling [86] develop a seven-body method for lower-limb kinematic estimation. However, they evaluate it solely for knee FE yielding mean RMS differences of 4.3 deg compared to a MOCAP-based inverse kinematics method and using a specific set of calibration motions designed to excite all lower-limb degrees of freedom (i.e., different than the walking gaits in this chapter for the ErKF method). As shown in Table 4.3, the ErKF method yields similar differences with MOCAP for the knee FE (4.1 deg), although for a different set of movements. Zhang et al. [65] validate the performance of a commercial Xsens system for walking and stair ascent/descent. They report mean and standard deviation joint angle differences up to 5.1 and 4.2 degrees, respectively for walking (depending on the joint). However, they do not report RMS differences and so direct comparisons cannot be made to this study. Nüesch et al. [106] validate the commercial RehaGait system for treadmill walking and report RMS differences of 9.6, 7.6, and 4.5 deg for FE of the hip, knee, and ankle, respectively. Compared to this study, the ErKF method demonstrates superior or comparable FE estimates for all joints with RMS differences of 7.1, 4.1, and 5.3 deg for the hip, knee, and ankle, respectively (refer to Tab. 4.3). In comparing to these commercial systems, we also note that such systems generally also employ magnetometer data (not used for the ErKF) and rely on proprietary algorithms; thus, it is difficult to know their limitations.

We duly note that a minority of the kinematic estimates are prone to be exceptionally poor during certain gaits. For example, while we observe overall excellent estimates of ankle, knee, and hip joint angles across gait types, the hip IE estimates exhibit much higher differences for slow, backward, and lateral walking than for the faster (> 0.8 m/s) forward walking trials (refer to Tabs. 4.2 & 4.3). We also observe this same trend for estimates of stride length and step width (i.e., smaller differences for the two faster forward walks than for the other gaits; refer to Tab. 4.6). However, while not reported here, we observe that the differences in estimates appear to be subject dependent (i.e., certain subjects consistently exhibited higher differences in estimated joint angles and stride metrics across gait types while other subjects consistently exhibit low differences in these estimates across all gait types). This suggests that subject-specific systematic errors (i.e., in sensor to segment alignment, marker placement, joint center locations) may be the primary cause behind these rare but poor kinematic estimates. Thus, better methods for sensor to segment alignment may yield significant improvements to the results presented here. We also note the poorer stride metric estimates for slow walking compared to the other gaits; refer to Table 4.6. While further investigation is required to determine the source of these differences, note that this gait is much slower (< 0.5 m/s) than is typical of most populations. Additionally, such slower gaits are typically associated with lower signal-to-noise ratios in IMU data (assuming the same sensor hardware selection) which may negatively impact estimates from the ErKF method.

Despite the exceptions duly noted above, the ERKF method provides kinematic estimates that closely replicate those from MOCAP and across a broad range of gait types. Additionally, the method does not rely on ”laboratory-like” assumptions (e.g., level ground) nor does it rely on magnetometer data (susceptible to pollution by magnetic interferences in both indoor and outdoor environments).

4.4.1 Limitations

Several limitations also exist with the current method. First MOCAP data is used to determine sensor to segment alignment; thus, it is not yet an ”IMU-only” method. However, sensor to segment alignment for wearable IMUs is a major topic of research in itself [83] and promising existing methods could be incorporated in the ErKF method. As described in the Discussion (Sec. 4.4), while this study does not assume laboratory-like conditions (e.g., level ground), the method is evaluated only on data from treadmill walking trials. Future studies should examine the accuracy of the method on uneven terrain including outdoor environments. In the present study, trials are only one minute in length. Future work should evaluate the method on longer trials to ensure that drift errors remain constrained over long times (e.g., hours). The accuracy of joint angle estimates are compared to two different MOCAP-based methods to evaluate the performance of the ErKF method. Comparison against the MOCAP cluster method enables evaluation of the ErKF method without some of the soft tissue artefacts. However, we emphasize that errors in sensor to segment calibration (including those due to marker misplacement and inaccurate joint center location estimates) and movement of the IMU relative to the underlying bone all affect the method’s performance. Thus, errors in MOCAP marker placement will critically affect all three estimation methods used in this study. Similarly, the current methods rely on static estimates of joint centers (i.e., estimation from marker locations and anthropometrics). These methods rely on new subjects having similar characteristics to those used to determine the estimation equations and then on accurate marker placement (as emphasized above). While not reported in the results, we often observe that estimated IMU velocities are frequently offset compared to MOCAP estimates of the IMU velocities. Nevertheless, position metrics (i.e., stride length and step width) demonstrate good accuracy despite the velocity offsets. Future studies should assess the accuracy of velocities estimated through the ErKF method to better understand the sources of these offsets. Finally, note that comparisons between this study and other methods are inherently difficult due to a multitude of differences including in marker placement, recruited subject populations, MOCAP reference systems used, IMU hardware selection (see Ch. 2), tasks performed, study design, and data processing techniques. Thus, future comparison of filtering methods alone will require commonly shared data sets, including highly accurate ground truth data for reference.

4.5 Conclusions

In this study, the novel ErKF method is extended to a full (seven-body) model of the lower limbs for human subjects. Doing so brings new challenges including: 1) increasing the degrees of freedom, 2) characterizing complex biological (versus mechanical) joints (e.g., joint center location and sensor to segment alignment), and 3) soft tissue artefacts. Importantly, this chapter contributes a novel application of the joint axis measurement correction in the ErKF for the hip and knee to reduce angle drift errors. In contrast to previous IMU-based joint axis correction methods (specific to the knee), it reduces these drift errors without assumptions of strict hinge-like behavior during certain times. Thus, the correction contributed in this chapter is also suitable for application to the hip (but with different measurement noise parameters). Significantly, this work validates the ErKF method on human subjects walking with six different gait types including forward walking (at slow, normal, and fast speeds), backward walking, and lateral walking (both left and right). The method also shows great promise for evaluating abnormal gaits (e.g., due to injury and/or disease) due to its demonstrated agreement (compared to MOCAP) in estimating joint angles, joint angle range of motion, stride length, and step width across all six gait types studied. In particular, for all gait types studied, RMS differences between ErKF and MOCAP cluster-based joint angle estimates generally remain below 5 degrees for all three ankle joint angles and for flexion/extension and abduction/adduction of the hips and knees. Additionally, RMS differences between ErKF and MOCAP inverse kinematics estimates in (stride to stride) range of motion generally remain below 5 degrees for all hip and knee joint angles (with slightly higher differences for the ankle joint angles) and across all gait types. Finally, mean RMS differences between ErKF and MOCAP estimates for both stride length and step width remain below 0.13 meters across all gait types (except stride length for slow forward walking) and below 0.07 meters for the two fastest walking gaits (> 0.8 m/s). The success of this method in estimating key kinematic measures comparably to MOCAP over a broad range of walking gaits confirm the significant promise of this novel ErKF method as a research strategy for non-laboratory based biomechanical studies of the human lower limbs and in broad contexts.

Chapter 5

Major Contributions and Future Research Directions

5.1 Major Contributions

Advancements in wearable sensor-based methods for measuring human kinematics outside traditional laboratory environments will foster advancements across biomechanical research and clinical practice. This dissertation advances the ability to use body-worn IMUs to estimate human lower-limb kinematics in broad contexts. In particular, this dissertation culminates in a novel IMU-based method for estimating lower-limb kinematics without traditional laboratory constraints and movement assumptions. The estimation method also demonstrates good agreement between IMU-based estimates of major kinematic variables (i.e., 3D joint angles, joint angle range of motion, stride length, and step width) and MOCAP-based estimates and across a wide variety of gait types. The major contributions of each chapter are summarized as follows

Chapter 2 lays a critical foundation for the full lower-limb model by exploring the limiting case of a single foot-mounted IMU to estimate foot trajectories. This work reveals that the well-known ZUPT method (developed for walking) still yields accurate kinematic estimates for highly dynamic gaits including fast walking and running, given proper IMU sensor hardware selection. This result supports the application of a zero-velocity measurement correction for the feet in the lower-limb method developed in Chapter 3 (for a mechanical walker) and Chapter 4 (for a human subject), even for highly dynamic movements. This first study also contributes the requirements for the IMU sensor hardware needed for accurate estimates under highly dynamic conditions, like those experienced during competitive distance running. The requirements offer researchers the knowledge needed to optimize IMU sensor selection for study needs.

Following this foundation, a novel ErKF kinematic estimation method is developed for the lower limbs. This method relies on kinematic constraints to reduce or eliminate relative integration drift errors between segments. In contrast to most other IMU-based methods for estimating full lower-limb kinematics, this new method does not rely on data from magnetometers (and is thus immune to magnetic field disturbances) nor does it rely on the assumption of level ground. This estimation method is developed in two stages; a simplified three-body model for a walker and then a full seven-body model for a human.

The method specialized for a three-body model of a walker is contributed in Chapter 3. Estimates of key kinematic variables are validated through simulation and through experiments on a mechanical "walker" and on a human subject (trying to walk with stiff legs). The results of this study reveal that the ErKF method accurately estimates joint angles and stride metrics when the kinematic constraints (i.e., joint center locations, joint axes, and IMU still times) are well-characterized. For example, experimental RMS differences (between ErKF and MOCAP estimates) of the hip joint angles remain below 1.5 deg for the mechanical walker across all three angular degrees of freedom for the joints, and with RMS differences in estimated stride length and step width of 0.03 and 0.07 meters, respectively.

The success of the ErKF method for the three-body model (Ch. 3) foretells its extension to the full seven-body model of the lower limbs for human subjects in Chapter 4. Doing so brings new challenges including: 1) increasing the degrees of freedom, 2) characterizing complex biological (versus mechanical) joints (e.g., joint center location and sensor to segment alignment), and 3) soft tissue artefacts. Importantly, this chapter contributes a novel application of the joint axis measurement in the ErKF method for the hip and knee to reduce angle drift errors. In contrast to previous IMU-based joint axis correction methods (specific to the knee), it reduces these drift errors without assumptions of strict hinge-like behavior during certain times. Thus, the correction contributed in Chapter 4 is also suitable for application to the hip (but with different measurement noise parameters). Significantly, this work validates the ErKF method on human subjects walking with six different gait types including forward walking (at slow, normal, and fast speeds), backward walking, and lateral walking (both left and right). The method also shows great promise for evaluating abnormal gaits (e.g., due to injury and/or disease) due to its demonstrated agreement (compared to MOCAP) in estimating joint angles, joint angle range of motion, stride length, and step width across all six gait types studied. In particular, for all gait types studied, RMS differences between ErKF and MOCAP cluster-based joint angle estimates generally remain below 5 degrees for all three ankle joint angles and for flexion/extension and abduction/adduction of the hips and knees. Additionally, RMS differences between ErKF and MOCAP inverse kinematics estimates in (stride to stride) range of motion generally remain below 5 degrees for all hip and knee joint angles (with slightly higher differences for the ankle joint angles) and across all gait types. Finally, mean RMS differences between ErKF and MOCAP estimates for both stride length and step width remain below 0.12 meters across all gait types (except stride length for slow forward walking) and below 0.07 meters for the two fastest walking gaits (> 0.8 m/s).

5.2 Future Research Directions

The contributions of this dissertation represent a significant stride forward in using body-worn IMUs to evaluate human movement outside of the laboratory. However, additional advancements are still necessary to fully meet this challenge. For example, the present method relies on MOCAP data for determining the sensor to segment alignment. Incorporation of existing IMU-based sensor to segment alignment methods (or the development of new methods) will yield a method that is truly ”laboratory free”. Further, additional measurements (including those from additional sensors) should be incorporated within the ErKF method to further improve estimation of joint angles and stride metrics, particularly for internal/external rotation across all gait types and for stride metrics in slower walking gaits (i.e., < 0.5 m/s). Note that the present method can readily incorporate such additional measurements.

At present, direct comparisons between published IMU-based methods (including the one presented here) are inherently difficult to make due to a multitude of differences between studies. Major differences arise in marker placement, recruited subject populations, MOCAP reference systems used, IMU hardware selection, tasks performed, study design, and data processing techniques. This is especially pertinent because the accuracy of various IMU-based methods may be dependent on any number of these factors. Thus, robust comparisons of IMU-based methods now being developed will ultimately require commonly shared data sets (simulated and experimental), including highly accurate data for ground truth reference. Simulated IMU data sets (such as that used in Chapter 3) have many advantages including providing exact ground truth reference and enabling evaluation of different IMU hardware characteristics (see Chapter 2). Additionally, such data sets may be created from existing data sets obtained through other motion capture methods (e.g., marker-based MOCAP) to analyze broad types of realistic movements. However, for simulated data sets to provide the greatest benefit for validation and comparison of IMU-based estimation methods, sensor hardware characteristics and motions of the IMU due to soft tissue movement must be well characterized so that simulated IMU data accurately represents ”real-world” experimental data. Shared experimental data sets ensure that methods are evaluated using real data and motions. Such data sets should include well-characterized sensor and reference measurement error models. Additionally, these data sets should span broad applications and target populations including diversity in motion types, demographics, anthropometric measurements, and movement pathology levels. Importantly, to effectively evaluate and compare the accuracy of IMU-based methods with experimental data sets, accurate ground truth data will require highly accurate motion capture methods such as stereo radiography or other advancements in motion capture.

In addition to estimating kinematical quantities, continuing advances in estimating other biomechanical quantities add to the future utility of wearable sensor networks. For example, additional sensors could be incorporated to estimate kinetic quantities (e.g., ground reaction forces, energy) and relevant biomechanical processes (e.g., muscle activity, respiration, heart rate) for holistic representations of human activity and performance. Additional benefits could arise from studying human movement without the need for visual observation or reliance on subjects following strict protocols. However, doing so would then also require means to interpret the data for context (e.g., task being performed, environment in which it is performed). Consequently, future work should also advance methods using wearable sensors to estimate contextual information.

Appendix A

Full Statistical Results from Linear Mixed-Effects Models

We report results for four statistical analyses that reveal the effects of accelerometer range, gyro range, and downsampling by two methods. For each of the four analyses, we utilize a linear mixed-effects model to test the effects of speed, sensor parameter (sensor range or sampling frequency), and the combination of speed and sensor parameter on the cumulative distance error. In each model, we remove subject effects by treating the subject as a random effect. Because we are interested in the effect of mean speed on the cumulative distance error without saturation, we treat mean speed as a continuous variable and fixed effect. We are also interested in the interaction of mean speed and the sensor parameter (i.e., how speed affects the cumulative distance error for a change in the sensor parameter versus that effect for the baseline sensor parameter) and include this interaction as a fixed effect. The model also calculates the effects of the sensor parameter alone (effect of only sensor parameter independent of speed) and a y-axis intercept (cumulative distance error with a mean speed of 0 m/s) for the baseline sensor condition; however, we do not include those additional findings as they do not add to the conclusions or the interpretation of the presented results. In each analysis, we use estimates obtained from the original (non-truncated or non-downsampled) IMU data as the baseline. All statistical analyses are run in R statistical software using lme4 and lmerTest packages [107–109]. The function *lmer* is used to fit the models and the function *confint* is used to compute 95% confidence intervals for all estimates.

The four tables below present results from this model for each of the four analyses. The first (shaded) row in each table reports the effect of speed only on the cumulative distance error for the baseline sensor condition. This includes an estimated linear slope for the cumulative distance error versus speed (i.e., an estimated slope of 1%/(m/s) would indicate that the cumulative distance error increases by an estimated 1% for each 1 m/s increase in mean speed) for the baseline sensor condition where a negative value means that the error is negative as defined in Chapter 2 (i.e., underprediction of cumulative distance). This slope also represents the sensitivity of the cumulative distance error to mean speed. In the remaining (unshaded) rows, we report the interactions of mean speed and the sensor parameter (i.e., how a change to sensor parameters compared to the baseline sensor condition impacts the sensitivity of the cumulative distance error to mean speed). The estimated slopes in these rows denote the estimated *difference* in the slope of the cumulative distance error versus speed over that for the baseline condition. Thus, these entries report the additional error sensitivity to speed for the specified change in the sensor parameter relative to the baseline. For example, in Table A.1, the estimated cumulative distance speed error is negative and it grows by -0.39%/(m/s) for the baseline sensor. The error sensitivity then grows (i.e., worsens) by an additional -0.57%/(m/s) for a sensor employing an accelerometer with a 24 g range. The third and fourth columns report the significance (p-value) and the 95% confidence interval for the estimated slope/error sensitivity.

Table A.1: Effect of speed on the cumulative distance versus accelerometer range. First (shaded) row reports the estimated slope of the cumulative distance versus mean speed using the baseline sensor (100 g range accelerometer). Remaining (unshaded) rows report estimated differences in this slope for IMUs with indicated acceleration ranges compared to the baseline IMU (i.e., the increased error sensitivity to speed with the indicated reductions in acceleration range relative to the baseline range).

Speed Effect	**Estimated Slope (%/(m/s))**	***p*-value**	**95% Conf. Int.**
Baseline (100g)	-0.39	<0.01	(-0.65,-0.13)
75 g vs. Baseline	0.00	0.99	(-0.37,0.37)
50 g vs. Baseline	-0.03	0.88	(-0.39,0.34)
24 g vs. Baseline	-0.57	<0.01	(-0.94,-0.21)
16 g vs. Baseline	-1.08	<0.001	(-1.45,-0.72)
10 g vs. Baseline	-2.24	<0.001	(-2.60,-1.87)
6 g vs. Baseline	-5.70	<0.001	(-6.06,-5.33)

Table A.2: Effect of speed on the cumulative distance versus gyro range. First (shaded) row reports the estimated slope of cumulative distance versus mean speed using the baseline sensor (2000 deg/s gyro). Remaining (unshaded) rows report estimated differences in this slope for IMUs with indicated angular velocity ranges compared to the baseline IMU (i.e., the increased error sensitivity to speed following the indicated reductions in angular velocity range relative to the baseline range).

Speed Effect	**Estimated Slope (%/(m/s))**	***p*-value**	**95% Conf. Int.**
Baseline (2000 deg/s)	-0.41	<0.01	(-0.68,-0.13)
1500 deg/s vs. Baseline	0.00	0.99	(-0.39,0.39)
1000 deg/s vs. Baseline	0.05	0.81	(-0.34,0.44)
750 deg/s vs. Baseline	-0.40	<0.05	(-0.80,-0.01)
500 deg/s vs. Baseline	-3.08	<0.001	(-3.47,-2.69)

Table A.3: Effect of speed on the cumulative distance versus sampling frequency for Method 1 (downsample). First (shaded) row reports the estimated slope of the cumulative distance traveled versus mean speed using the baseline sensor (1000 Hz). Remaining (unshaded) rows report the estimated differences in this slope for IMUs with the indicated sampling frequency compared to the baseline IMU (i.e., the increased error sensitivity to speed following the indicated reductions in sampling frequency relative to the baseline sampling frequency).

Speed Effect	**Estimated Slope (%/(m/s))**	***p*-value**	**95% Conf. Int.**
Baseline (1000 Hz)	-1.12	<0.001	(-1.48,-0.77)
500 Hz vs. Baseline	-0.09	0.73	(-0.59,0.41)
250 Hz vs. Baseline	-0.13	0.63	(-0.63,0.38)
125 Hz vs. Baseline	-0.26	0.32	(-0.76,0.24)
62.5 Hz g vs. Baseline	0.94	<0.001	(0.44,1.44)

Table A.4: Effect of speed on the cumulative distance versus sampling frequency for Method 2 (decimation). First (shaded) row reports the estimated slope of the cumulative distance traveled versus mean speed using the baseline sensor (1000 Hz). Remaining (unshaded) rows report the estimated differences in this slope for IMUs with the indicated sampling frequency compared to the baseline IMU (i.e., the increased error sensitivity to speed following the indicated reductions in sampling frequency relative to the baseline sampling frequency).

Speed Effect	**Estimated Slope (%/(m/s))**	***p*-value**	**95% Conf. Int.**
Baseline (1000 Hz)	-1.17	<0.001	(-1.50,-0.85)
500 Hz vs. Baseline	-0.01	0.96	(-0.47,0.45)
250 Hz vs. Baseline	-0.03	0.90	(-0.49,0.43)
125 Hz vs. Baseline	0.08	0.74	(-0.38,0.54)
62.5 Hz g vs. Baseline	0.12	0.60	(-0.33,0.58)

Appendix B

Identification of Footfalls, Still Periods, and Straight-leg Instances

Here, we detail how footfalls, still periods, and straight-leg instances are determined for the study. Footfalls and still periods are times when the foot is assumed to be still, with only one footfall being identified per stride. Straight-leg instances are times when the human subject's leg is assumed to be in a repeatable and identifiable configuration (once per stride).

Using the methods outlined below, success in identifying a footfall compared to the reference measurement system (simulation or MOCAP) is $> 99\%$ for the model and $> 93\%$ for the human stiff-legged walk. We manually correct missing and misidentified footfalls (using velocity estimates from the reference system) so that our results are not impacted by errors in footfall identification. We note that these specialized methods are specifically developed for the current application and may not translate well to more common human gait patterns.

Reference Data Set 1: Model Estimates for Walker Compared to Simulation

Footfalls are identified exactly in the middle of the prescribed 0.1 second still periods at the beginning of the stance phase. Still periods are identified as all instances where the entire model was still (0.1 seconds following each heel contact).

Reference Data Set 2: Model IMU Estimates for Walker Compared to MOCAP

Still periods and foot impacts are estimated as follows. For each foot IMU, angular velocity data is filtered using a 4th order low-pass Butterworth filter at 6 Hz. Angular acceleration is then calculated from the filtered angular velocity using finite differentiation. Still periods are determined when three criteria were simultaneously satisfied:

1. $Angular\,acceleration\,magnitude < 115\,deg/s^2$
2. $Angular\,velocity\,magnitude < 45\,deg/s$
3. $|(Linear\,acceleration\,magnitude - 1g)| < 0.2g$

where $|x|$ denotes the absolute value of x and g denotes the gravitational acceleration. Foot impacts are identified as peaks in angular velocity magnitude that is high-pass filtered at 20 Hz with a 4^{th} order Butterworth filter.

Next, strides are segmented using the filtered angular velocity data. Specifically, peaks associated primarily with the internal rotation axis greater than 3 seconds apart identify when the subject is turning while peaks associated with the flexion axis greater than 1 second apart segment individual strides during walking. The footfall in each stride is then identified from still periods following the associated stride's foot impact. Specifically, the footfall is specified in the middle of the longest continuous series of still periods (excluding gaps 1 sample in length) that is within 0.3 seconds of a foot impact during that stride.

Reference Data Set 3: Model Estimates for Human Stiff-legged Walk Compared to MOCAP

Differences in the dynamics of the 3-body model's foot during stance compared to a human foot necessitate a different approach for still and footfall instance detection. Still periods are determined using the same criteria as for the 3-body model, but with the angular velocity magnitude threshold being 60 deg/s. We separately define a low motion instance as one where the acceleration and angular velocity thresholds are met, but not necessarily the angular acceleration. Stance phases are identified as all series of consecutive low motion periods that are at least 0.5 seconds in length. Footfalls are then identified as the instance of the lowest angular velocity magnitude within these stance phases.

For straight-leg instances, we identify times where the leg is in a repeatable and identifiable configuration (i.e., set of joint angles). Specifically, we identify when the leg is fully extended during the transition from forward swing to terminal swing as follows. We again take advantage of the known approximate alignment between the IMU and foot to identify the IMU axis that is most nearly in the medial/lateral direction. For illustration, we will proceed as if the IMU y-axis is pointing to the subject's left (as was done in our study), but note that the following logic can be readily applied by substituting a different axis. Between each set of footfalls, we identify the forward swing of the leg using the peak negative y-axis angular velocity. The straight-leg instance is then identified as the first zero crossing of the y-axis angular velocity following the identified forward swing (approximately the transition from forward to terminal swing). The accuracy of straight-leg instance detection was not quantitatively assessed and no manual corrections were made.

Appendix C

Example Trajectories for Six Walking Gaits

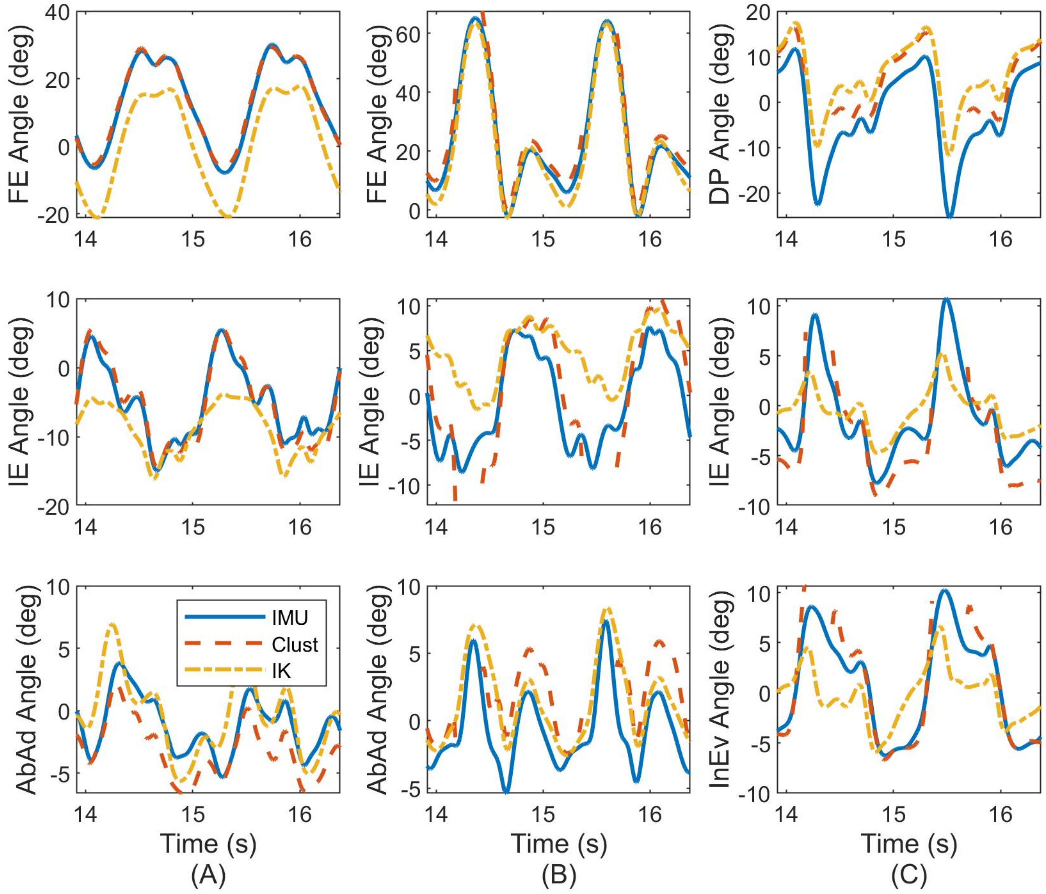

Figure C.1: Example joint angle estimates over two stride cycles for normal treadmill walking. Plots show the three anatomical angles for (A) left hip, (B) left knee, and (C) left ankle. Estimates are also compared between ErKF (IMU), cluster (Clust), and inverse kinematics (IK) methods.

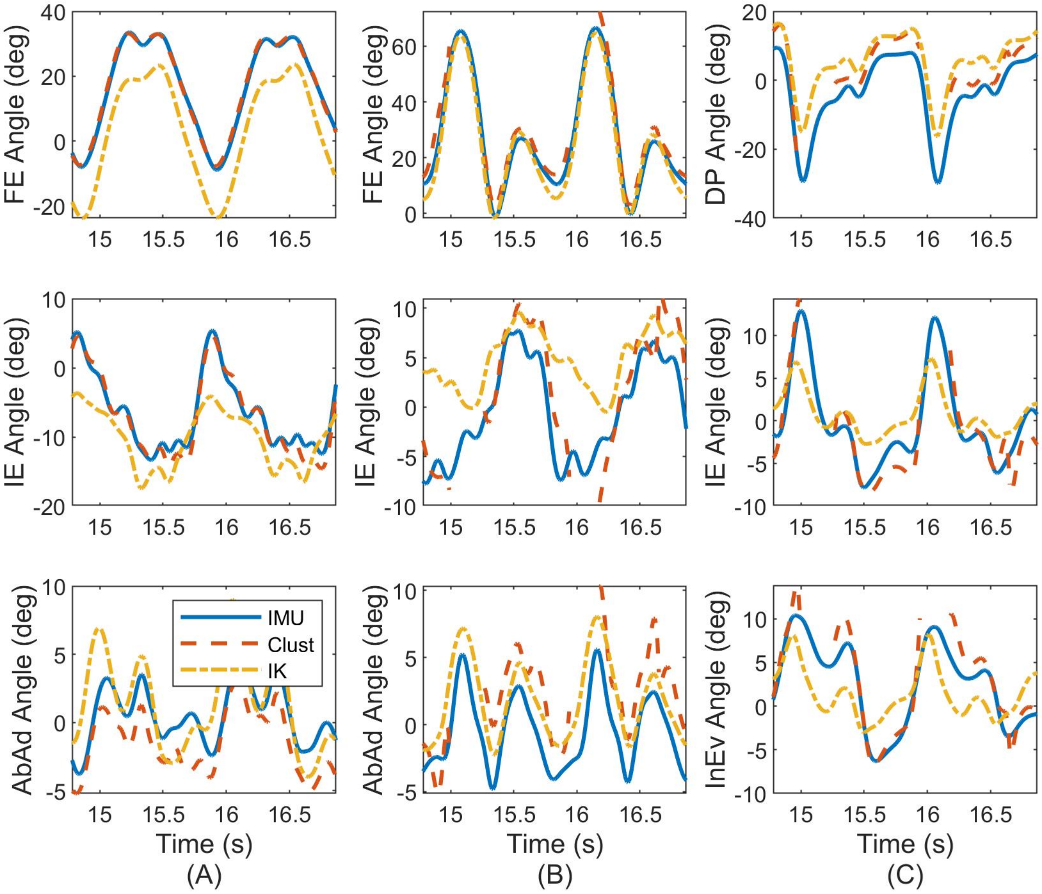

Figure C.2: Example joint angle estimates over two stride cycles for fast treadmill walking. Plots show the three anatomical angles for (A) left hip, (B) left knee, and (C) left ankle. Estimates are also compared between ErKF (IMU), cluster (Clust), and inverse kinematics (IK) methods.

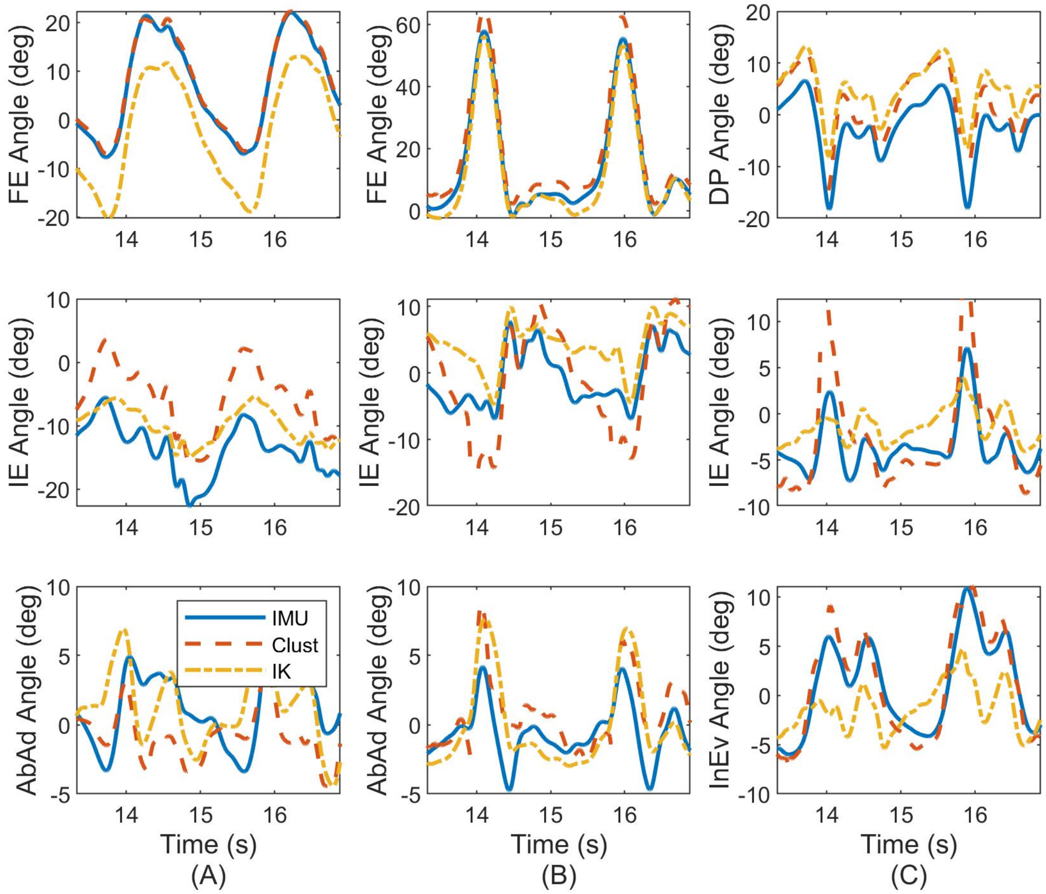

Figure C.3: Example joint angle estimates over two stride cycles for slow treadmill walking. Plots show the three anatomical angles for (A) left hip, (B) left knee, and (C) left ankle. Estimates are also compared between ErKF (IMU), cluster (Clust), and inverse kinematics (IK) methods.

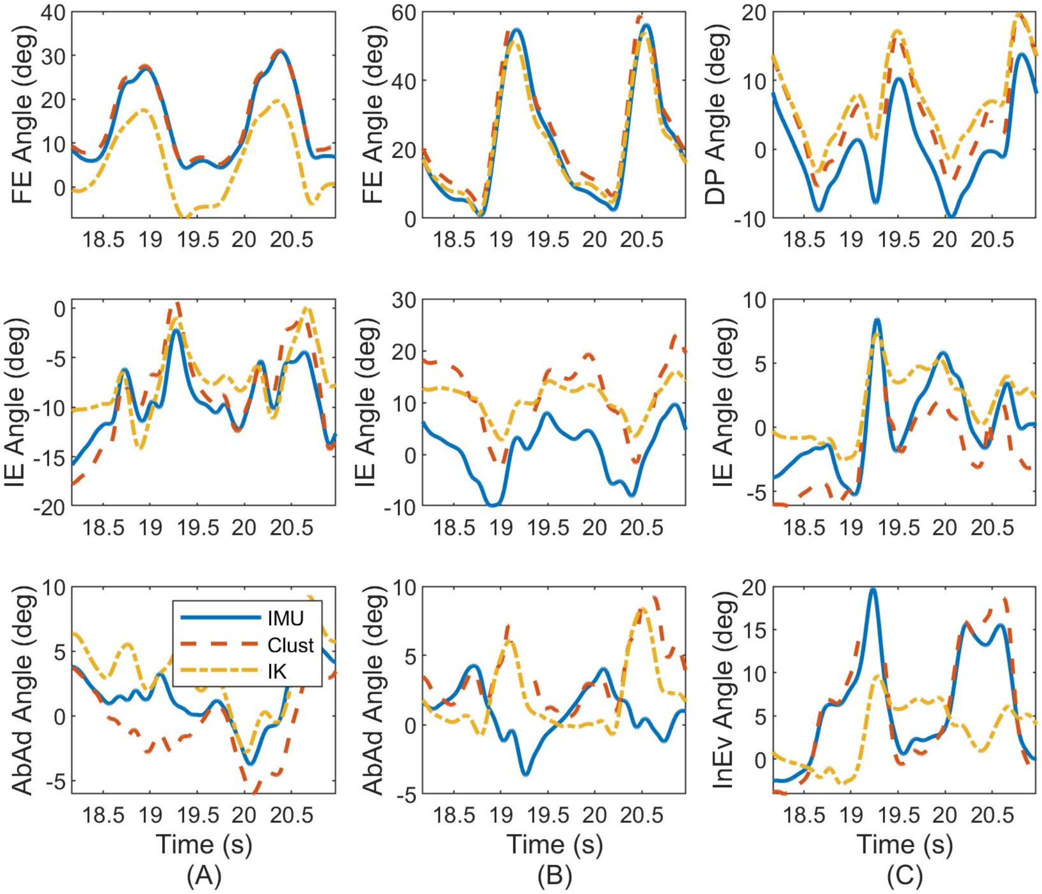

Figure C.4: Example joint angle estimates over two stride cycles for backwards treadmill walking. Plots show the three anatomical angles for (A) left hip, (B) left knee, and (C) left ankle. Estimates are also compared between ErKF (IMU), cluster (Clust), and inverse kinematics (IK) methods.

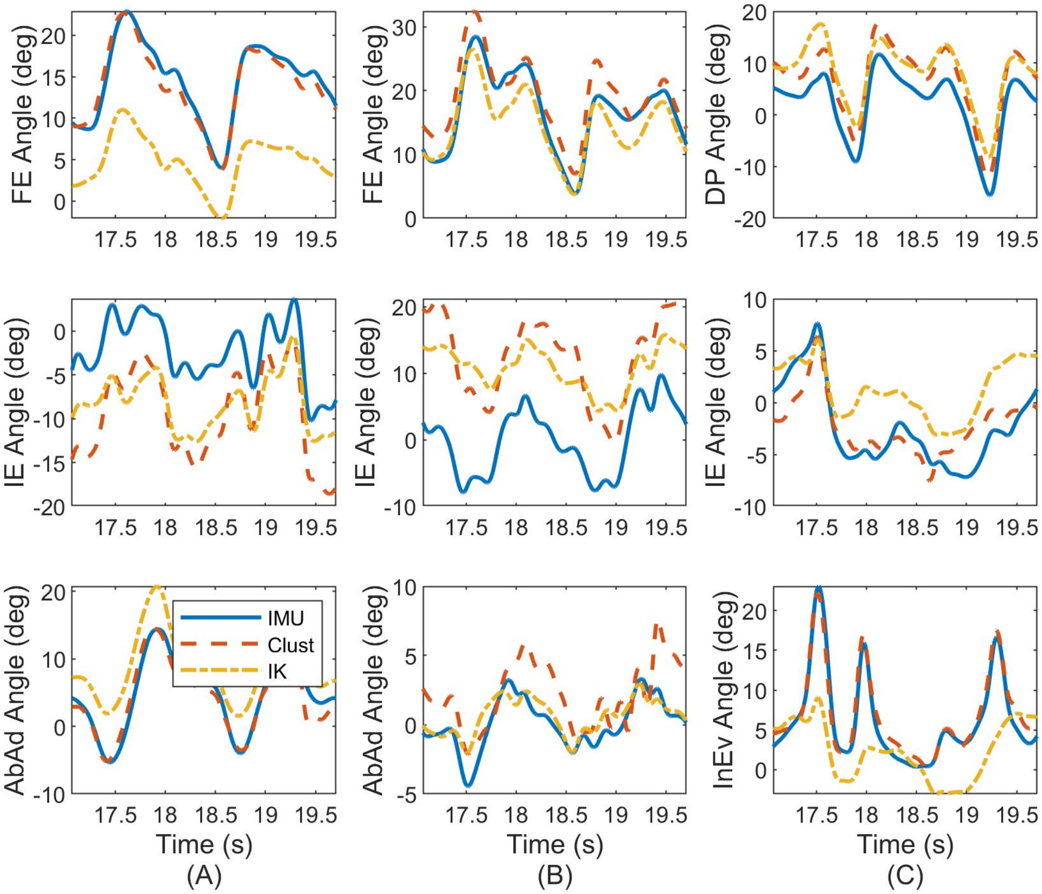

Figure C.5: Example joint angle estimates over two stride cycles for lateral left treadmill walking. Plots show the three anatomical angles for (A) left hip, (B) left knee, and (C) left ankle. Estimates are also compared between ErKF (IMU), cluster (Clust), and inverse kinematics (IK) methods.

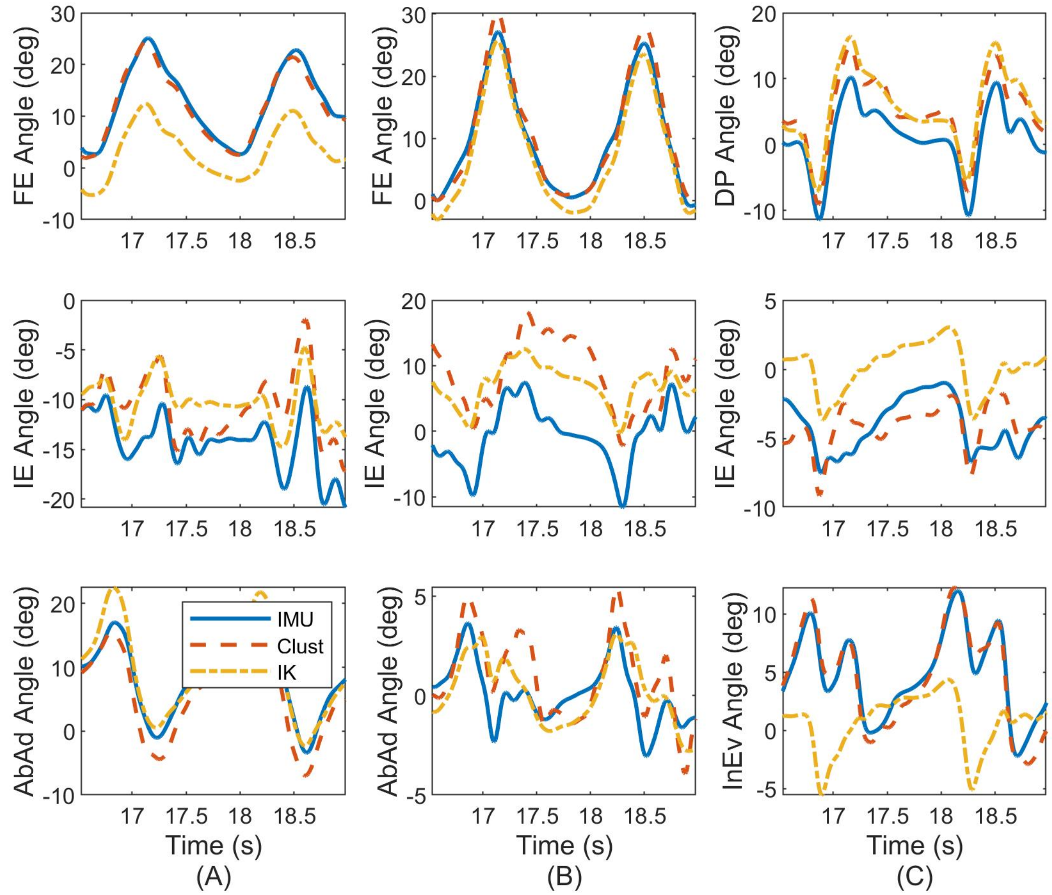

Figure C.6: Example joint angle estimates over two stride cycles for lateral right treadmill walking. Plots show the three anatomical angles for (A) left hip, (B) left knee, and (C) left ankle. Estimates are also compared between ErKF (IMU), cluster (Clust), and inverse kinematics (IK) methods.

Bibliography

[1] Song Joo Lee and Joseph Hidler. Biomechanics of overground vs. treadmill walking in healthy individuals. *Journal of Applied Physiology*, 104(3):747–755, 2008. doi: 10.1152/japplphysiol.01380.2006.

[2] Lauro V. Ojeda, John R. Rebula, Arthur D. Kuo, and Peter G. Adamczyk. Influence of contextual task constraints on preferred stride parameters and their variabilities during human walking. *Medical Engineering & Physics*, 37(10):929 – 936, 2015. doi: 10.1016/j.medengphy.2015.06.010.

[3] Rosaria Rucco, Antonietta Sorriso, Marianna Liparoti, Giampaolo Ferraioli, Pierpaolo Sorrentino, Michele Ambrosanio, and Fabio Baselice. Type and location of wearable sensors for monitoring falls during static and dynamic tasks in healthy elderly: A review. *Sensors*, 18:1613, 05 2018. doi: 10.3390/s18051613.

[4] Luis Montesinos, Rossana Castaldo, and Leandro Pecchia. Wearable inertial sensors for fall risk assessment and prediction in older adults: A systematic review and meta-analysis. *IEEE Transactions on Neural Systems and Rehabilitation Engineering*, 26(3):573–582, 2018. doi: 10.1109/TNSRE.2017.2771383.

[5] Ping Li, Ramy Meziane, Martin J.-D. Otis, Hassan Ezzaidi, and Philippe Cardou. A smart safety helmet using IMU and EEG sensors for worker fatigue detection. In *ROSE 2014 - 2014 IEEE International Symposium on RObotic and SEnsors Environments, Proceedings*, 10 2014. doi: 10.1109/ROSE.2014.6952983.

[6] Pitre C. Bourdon, Marco Cardinale, Andrew Murray, Paul Gastin, Michael Kellmann, Matthew C. Varley, Tim J. Gabbett, Aaron J. Coutts, Darren J. Burgess, Warren Gregson, and N. Timothy Cable. Monitoring athlete training loads: Consensus statement. *International Journal of Sports Physiology and Performance*, 12:S2–161–S2–170, 2017. doi: 10.1123/IJSPP.2017-0208.

[7] Michelle Norris, Ross Anderson, and Ian C. Kenny. Method analysis of accelerometers and gyroscopes in running gait: A systematic review. *Proceedings of the Institution of Mechanical Engineers Part P Journal of Sports Engineering and Technology*, 228:3–15, 03 2014. doi: 10.1177/1754337113502472.

[8] Angelo M. Sabatini, Chiara Martelloni, Sergio Scapellato, and Filippo Cavallo. Assessment of walking features from foot inertial sensing. *IEEE Transactions on Biomedical Engineering*, 52(3):486–494, March 2005. doi: 10.1109/TBME.2004.840727.

[9] David Titterton and John Weston. *Strapdown Inertial Navigation Technology.* Radar, Sonar &, Navigation. Institution of Engineering and Technology, 2004.

[10] Rita Stagni, Silvia Fantozzi, Angelo Cappello, and Alberto Leardini. Quantification of soft tissue artefact in motion analysis by combining 3D fluoroscopy and stereophotogrammetry: a study on two subjects. *Clinical Biomechanics*, 20(3):320 – 329, 2005. doi: 10.1016/j.clinbiomech.2004.11.012.

[11] Rachel V. Vitali, Stephen M. Cain, Ryan S. McGinnis, Antonia M. Zaferiou, Lauro V. Ojeda, Steven P. Davidson, and Noel C. Perkins. Method for estimating three-dimensional knee rotations using two inertial measurement units: Validation with a coordinate measurement machine. *Sensors*, 17(9):1970, 2017. doi: 10.3390/s17091970.

[12] M.J. Pearcy. Stereo radiography of lumbar spine motion. *Acta Orthopaedica Scandinavica*, 56(212): 1–45, 1985. doi: 10.3109/17453678509154154.

[13] Johan Kärrholm, Göran Selvik, Lars-Gunnar Elmqvist, and Lars Ingvar Hansson. Active knee motion after cruciate ligament rupture. *Acta Orthopaedica Scandinavica*, 59(2):158–164, 1988. doi: 10.1080/17453678809169699.

[14] Christine E. Draper, Thor F. Besier, Juan M. Santos, Fabio Jennings, Michael Fredericson, Garry E. Gold, Gary S. Beaupre, and Scott L. Delp. Using real-time MRI to quantify altered joint kinematics in subjects with patellofemoral pain and to evaluate the effects of a patellar brace or sleeve on joint motion. *Journal of Orthopaedic Research*, 27(5):571–577, 2009. doi: 10.1002/jor.20790.

[15] S. Corazza, L. Mündermann, A.M. Chaudhari, T. Demattio, C. Cobelli, and T.P. Andriacchi. A markerless motion capture system to study musculoskeletal biomechanics: Visual hull and simulated annealing approach. *Annals of Biomedical Engineering*, 34(6):1019–1029, 2006. doi: 10.1007/s10439-006-9122-8.

[16] Wolfgang Teufl, Markus Miezal, Bertram Taetz, Michael Fröhlich, and Gabriele Bleser. Validity, test-retest reliability and long-term stability of magnetometer free inertial sensor based 3D joint kinematics. *Sensors*, 18(7):1980, 2018. doi: 10.3390/s18071980.

[17] Rachel V. Vitali, Stephen M. Cain, Lauro V. Ojeda, Michael V. Potter, Antonia M. Zaferiou, Steven P. Davidson, Megan E. Coyne, Clifford L. Hancock, Alyssa Mendoza, Leia A. Stirling, and Noel C. Perkins. Body-worn IMU array reveals effects of load on performance in an outdoor obstacle course. *PLoS ONE*, 14(3):e0214008, 2019. doi: 10.1371/journal.pone.0214008.

[18] Thomas P. Andriacchi and Eugene J. Alexander. Studies of human locomotion: Past, present and future. *Journal of Biomechanics*, 33(10):1217–1224, 2000. doi: 10.1016/S0021-9290(00)00061-0.

[19] Peter R. Cavanagh and Rodger Kram. Stride length in distance running: velocity, body dimensions, and added mass effects. *Medicine & Science in Sports & Exercise*, 21(4):467–479, 1989. doi: 10.1249/00005768-198908000-00020.

[20] Tom F. Novacheck. The biomechanics of running. *Gait & Posture*, 7(1):77–95, 1998. doi: 10.1016/S0966-6362(97)00038-6.

[21] Jennifer S. Brach, Jaime E. Berlin, Jessie M. Vanswearingen, Anne B. Newman, and Stephanie A. Studenski. Too much or too little step width variability is associated with a fall history in older persons who walk at or near normal gait speed. *Journal of Neuroengineering and Rehabilitation*, 2:21, 2005. doi: 10.1186/1743-0003-2-21.

[22] Thomas Schmalz, Siegmar Blumentritt, and Rolf Jarasch. Energy expenditure and biomechanical characteristics of lower limb amputee gait: The influence of prosthetic alignment and different prosthetic components. *Gait & Posture*, 16(3):255–63, 2002. doi: 10.1016/S0966-6362(02)00008-5.

[23] Lauro Ojeda and Johann Borenstein. Non-GPS navigation for security personnel and first responders. *The Journal of Navigation*, 60(3):391–407, 2007. doi: 10.1017/S0373463307004286.

[24] John R. Rebula, Lauro V. Ojeda, Peter G. Adamczyk, and Arthur D. Kuo. Measurement of foot placement and its variability with inertial sensors. *Gait & Posture*, 38(4):974 – 980, 2013. doi: 10.1016/j.gaitpost.2013.05.012.

[25] Eric Foxlin. Pedestrian tracking with shoe-mounted inertial sensors. *IEEE Computer Graphics and Applications*, 25(6):38–46, Nov.-Dec. 2005. doi: 10.1109/MCG.2005.140.

[26] Jasper Reenalda, Erik Maartens, Lotte Homan, and J.H. (Jaap) Buurke. Continuous three dimensional analysis of running mechanics during a marathon by means of inertial magnetic measurement units to objectify changes in running mechanics. *Journal of Biomechanics*, 49(14):3362 – 3367, 2016. doi: 10.1016/j.jbiomech.2016.08.032.

[27] John H. Hollman, Molly K. Watkins, Angela C. Imhoff, Carly E. Braun, Kristen A. Akervik, and Debra K. Ness. A comparison of variability in spatiotemporal gait parameters between treadmill and overground walking conditions. *Gait & Posture*, 43:204 – 209, 2016. doi: 10.1016/j.gaitpost.2015.09.024.

[28] Michael V. Potter, Lauro V. Ojeda, Noel C. Perkins, and Stephen M. Cain. Effect of IMU design on IMU-derived stride metrics for running. *Sensors*, 19(11):2601, 2019. doi: 10.3390/s19112601.

[29] Nikolas Trawny and Stergios Roumeliotis. Indirect kalman filter for 3D attitude estimation. Technical Report 2005-002, Multiple Autonomous Robotic Systems Laboratory, Mar 2005.

[30] Joan Sola. Quaternion kinematics for the error-state Kalman filter. *arXiv preprint arXiv:1711.02508*, 2017.

[31] Ajay Seth, Jennifer L. Hicks, Thomas K. Uchida, Ayman Habib, Christopher L. Dembia, James J. Dunne, Carmichael F. Ong, Matthew S. DeMers, Apoorva Rajagopal, Matthew Millard, Samuel R. Hamner, Edith M. Arnold, Jennifer R. Yong, Shrinidhi K. Lakshmikanth, Michael A. Sherman, Joy P. Ku, and Scott L. Delp. OpenSim: Simulating musculoskeletal dynamics and neuromuscular control to study human and animal movement. *PLOS Computational Biology*, 14(7):e1006223, 2018. doi: 10.1371/journal.pcbi.1006223.

[32] Scott L. Delp, Frank C. Anderson, Allison S. Arnold, Peter Loan, Ayman Habib, Chand T. John, Eran Guendelman, and Darryl G. Thelen. OpenSim: Open-source software to create and analyze dynamic simulations of movement. *IEEE Transactions on Biomedical Engineering*, 54(11):1940–1950, 2007. doi: 10.1109/TBME.2007.901024.

[33] Haifeng Xing, Jinglong Li, Bo Hou, Yongjian Zhang, and Meifeng Guo. Pedestrian stride length estimation from IMU measurements and ANN based algorithm. *Journal of Sensors*, page 06091261, 2017. doi: 10.1155/2017/6091261.

[34] John Elwell. Inertial navigation for the urban warrior. In *Proc. SPIE 3709, Digitization of the Battlespace IV (9 July 1999)*, 1999. doi: 10.1117/12.351609.

[35] Lauro Ojeda, John R. Rebula, Peter G. Adamczyk, and Arthur D. Kuo. Mobile platform for motion capture of locomotion over long distances. *Journal of Biomechanics*, 46(13):2316 – 2319, 2013. doi: 10.1016/j.jbiomech.2013.06.002.

[36] Naoki Kitagawa and Naomichi Ogihara. Estimation of foot trajectory during human walking by a wearable inertial measurement unit mounted to the foot. *Gait & Posture*, 45:110–114, 2016. doi: 10.1016/j.gaitpost.2016.01.014.

[37] C. Markus Brahms, Yang Zhao, David Gerhard, and John M. Barden. Stride length determination during overground running using a single foot-mounted inertial measurement unit. *Journal of Biomechanics*, 71:302–305, 2018. doi: 10.1016/j.jbiomech.2018.02.003.

[38] Antti Leskinen, Keijo Häkkinen, Mikko Virmavirta, Juha Isolehto, and Heikki Kyröläinen. Comparison of running kinematics between elite and national-standard 1500-m runners. *Sports Biomechanics*, 8:1–9, 2009. doi: 10.1080/14763140802632382.

[39] Brian Hanley. Pacing, packing and sex-based differences in Olympic and IAAF World Championship marathons. *Journal of Sports Sciences*, 34(17):1675–1681, 2016. doi: 10.1080/02640414.2015.1132841.

[40] Wouter Hoogkamer, Rodger Kram, and Christopher J. Arellano. How biomechanical improvements in running economy could break the 2-hour marathon barrier. *Sports Medicine*, 47(9):1739–1750, 2017. doi: 10.1007/s40279-017-0708-0.

[41] A. Peruzzi, U. Della Croce, and A. Cereatti. Estimation of stride length in level walking using an inertial measurement unit attached to the foot: A validation of the zero velocity assumption during stance. *Journal of Biomechanics*, 44(10):1991 – 1994, 2011. doi: 10.1016/j.jbiomech.2011.04.035.

[42] G.P. Bailey and R.K. Harle. Investigation of sensor parameters for kinematic assessment of steady state running using foot mounted IMUs. In *2nd International Congress on Sports Sciences Research and Technology Support*, pages 154–161, Rome, Italy, October 2014.

[43] Michael V. Potter, Lauro V. Ojeda, Noel C. Perkins, and Stephen M. Cain. Influence of accelerometer range on accuracy of foot-mounted IMU based running velocity estimation. In *41st Annual Meeting of the American Society of Biomechanics*, pages 1133–1134, Boulder, CO, August 2017.

[44] Christian Mitschke, Pierre Kiesewetter, and Thomas L. Milani. The effect of the accelerometer operating range on biomechanical parameters: Stride length, velocity, and peak tibial acceleration during running. *Sensors*, 18(1):130, 2018. doi: 10.3390/s18010130.

[45] Lauro V. Ojeda, Antonia M. Zaferiou, Stephen M. Cain, Rachel V. Vitali, Steven P. Davidson, Leia A. Stirling, and Noel C. Perkins. Estimating stair running performance using inertial sensors. *Sensors*, 17(11):2647, 2017. doi: 10.3390/s17112647.

[46] G.P. Bailey and R. Harle. Assessment of foot kinematics during steady state running using a foot-mounted IMU. *Procedia Engineering*, 72:32 – 37, 2014. doi: 10.1016/j.proeng.2014.06.009.

[47] Douglas Bates, Martin Mächler, Ben Bolker, and Steve Walker. Fitting linear mixed-effects models using lme4. *Journal of Statistical Software, Articles*, 67(1):1–48, 2015. doi: 10.18637/jss.v067.i01.

[48] H. Nyquist. Certain topics in telegraph transmission theory. *Transactions of the American Institute of Electrical Engineers*, 47(2):617–644, April 1928. doi: 10.1109/T-AIEE.1928.5055024.

[49] Claude E. Shannon. Communication in the presence of noise. *Proceedings of the IRE*, 37(1):10–21, Jan 1949. doi: 10.1109/JRPROC.1949.232969.

[50] Andreas Antoniou. *Digital Signal Processing: Signals, Systems, and Filters.* McGraw-Hill Education, New York, NY, 2006. ISBN 0-07-145424-1.

[51] Richard G. Lyons. *Understanding Digital Signal Processing.* Prentice Hall, Upper Saddle River, NJ, USA, 2011. ISBN 0-13-702741-9.

[52] MATLAB. Decimate. URL `https://www.mathworks.com/help/signal/ref/decimate.html`. accessed on 25 July 2018.

[53] David H. Sutherland. The evolution of clinical gait analysis: Part II kinematics. *Gait & posture*, 16 (2):159–179, 2002. doi: 10.1016/s0966-6362(02)00004-8.

[54] Kevin R. Ford, Gregory D. Myer, Harrison E. Toms, and Timothy E. Hewett. Gender differences in the kinematics of unanticipated cutting in young athletes. *Medicine & Science in Sports & Exercise*, 37(1):124–129, 2005. doi: 10.1249/01.MSS.0000150087.95953.C3.

[55] D. Hamacher, N.B. Singh, J.H. Van Dieën, M.O. Heller, and W.R. Taylor. Kinematic measures for assessing gait stability in elderly individuals: A systematic review. *Journal of The Royal Society Interface*, 8(65):1682–1698, 2011. doi: 10.1098/rsif.2011.0416.

[56] Weixin Wang and Peter Gabriel Adamczyk. Analyzing gait in the real world using wearable movement sensors and frequently repeated movement paths. *Sensors*, 19(8):1925, 2019. doi: 10.3390/s19081925.

[57] Alberto Ranavolo, Francesco Draicchio, Tiwana Varrecchia, Alessio Silvetti, and Sergio Iavicoli. Wearable monitoring devices for biomechanical risk assessment at work: Current status and future challenges—a systematic review. *International Journal of Environmental Research and Public Health*, 15(9):2001, 2018. doi: 10.3390/ijerph15092001.

[58] Natthapon Pannurat, Surapa Thiemjarus, and Ekawit Nantajeewarawat. Automatic fall monitoring: A review. *Sensors*, 14(7):12900–12936, 2014. doi: 10.3390/s140712900.

[59] Charence Wong, Zhi-Qiang Zhang, Benny Lo, and Guang-Zhong Yang. Wearable sensing for solid biomechanics: A review. *IEEE Sensors Journal*, 15(5):2747–2760, 2015. doi: 10.1109/JSEN.2015.2393883.

[60] Gamini Dissanayake, Salah Sukkarieh, Eduardo Nebot, and Hugh Durrant-Whyte. The aiding of a low-cost strapdown inertial measurement unit using vehicle model constraints for land vehicle applications. *IEEE Transactions on Robotics and Automation*, 17(5):731–747, 2001. doi: 10.1109/70.964672.

[61] Ive Weygers, Manon Kok, Marco Konings, Hans Hallez, Henri De Vroey, and Kurt Claeys. Inertial sensor-based lower limb joint kinematics: A methodological systematic review. *Sensors*, 20(3):673, 2020. doi: 10.3390/s20030673.

[62] Thomas Seel, Jörg Raisch, and Thomas Schauer. IMU-based joint angle measurement for gait analysis. *Sensors*, 14(4):6891–6909, 2014. doi: 10.3390/s140406891.

[63] Xavier Robert-Lachaine, Hakim Mecheri, Christian Larue, and André Plamondon. Validation of inertial measurement units with an optoelectronic system for whole-body motion analysis. *Medical & Biological Engineering & Computing*, 55(4):609–619, 2017. doi: 10.1007/s11517-016-1537-2.

[64] Stephanie Blair, Grant Duthie, Sam Robertson, William Hopkins, and Kevin Ball. Concurrent validation of an inertial measurement system to quantify kicking biomechanics in four football codes. *Journal of Biomechanics*, 73:24–32, 2018. doi: 10.1016/j.jbiomech.2018.03.031.

[65] Jun-Tian Zhang, Alison C Novak, Brenda Brouwer, and Qingguo Li. Concurrent validation of Xsens MVN measurement of lower limb joint angular kinematics. *Physiological Measurement*, 34(8):N63–9, 2013. doi: 10.1088/0967-3334/34/8/N63.

[66] Amin Ahmadi, François Destelle, Luis Unzueta, David S. Monaghan, Maria Teresa Linaza, Kieran Moran, and Noel E. O'Connor. 3D human gait reconstruction and monitoring using body-worn inertial sensors and kinematic modeling. *IEEE Sensors Journal*, 16(24):8823–8831, 2016. doi: 10.1109/JSEN.2016.2593011.

[67] Wolfgang Teufl, Michael Lorenz, Markus Miezal, Bertram Taetz, Michael Fröhlich, and Gabriele Bleser. Towards inertial sensor based mobile gait analysis: Event-detection and spatio-temporal parameters. *Sensors*, 19(1):38, 2019. doi: 10.3390/s19010038.

[68] Daniel A. Jacobs and Ajay Seth. Dynamic walking challenge: Go the distance! URL `https://simtk-confluence.stanford.edu:8443/pages/viewpage.action?pageId=28777060`. accessed on 10 Mar 2021.

[69] Venkatesh K. Madyastha, Vishal C. Ravindra, Srinath Mallikarjunan, and Anup Goyal. Extended Kalman filter vs. error state Kalman filter for aircraft attitude estimation. In *AIAA Guidance, Navigation, and Control Conference*, page 6615, 2011. doi: 10.2514/6.2011-6615.

[70] Ross Hartley, Maani Ghaffari, Ryan M. Eustice, and Jessy W. Grizzle. Contact-aided invariant extended Kalman filtering for robot state estimation. *The International Journal of Robotics Research*, 39(4):402–430, 2020. doi: 10.1177/0278364919894385.

[71] Rachel V. Vitali, Ryan S. McGinnis, and Noel C. Perkins. Robust error-state Kalman filter for estimating IMU orientation. *IEEE Sensors Journal*, 21(3):3561–3569, 2020. doi: 10.1109/JSEN.2020.3026895.

[72] Markus Miezal, Bertram Taetz, and Gabriele Bleser. On inertial body tracking in the presence of model calibration errors. *Sensors*, 16(7):1132, 2016. doi: 10.3390/s16071132.

[73] Ge Wu, Sorin Siegler, Paul Allard, Chris Kirtley, Alberto Leardini, Dieter Rosenbaum, Mike Whittle, Darryl D D'Lima, Luca Cristofolini, Hartmut Witte, Oskar Schmid, and Ian Stokes. ISB recommendation on definitions of joint coordinate system of various joints for the reporting of human joint motion—part I: ankle, hip, and spine. *Journal of Biomechanics*, 35(4):543 – 548, 2002. doi: 10.1016/S0021-9290(01)00222-6.

[74] Mariano Garcia, Anindya Chatterjee, Andy Ruina, and Michael Coleman. The simplest walking model: Stability, complexity, and scaling. *Journal of Biomechanical Engineering*, 120(2):281–288, 1998. doi: 10.1115/1.2798313.

[75] M.D. Shuster and S.D. Oh. Three-axis attitude determination from vector observations. *Journal of Guidance and Control*, 4(1):70–77, 1981.

[76] Manolis Lourakis. Absolute orientation with the quest algorithm. `https://www.mathworks.com/matlabcentral/fileexchange/65173-absolute-orientation-with-the-quest-algorithm`, 2020. accessed on 5 May 2020.

[77] John H. Challis. A procedure for determining rigid body transformation parameters. *Journal of Biomechanics*, 28(6):733–737, 1995. doi: 10.1016/0021-9290(94)00116-L.

[78] Lukas Adamowicz, Reed D. Gurchiek, Jonathan Ferri, Anna T. Ursiny, Niccolo Fiorentino, and Ryan S. McGinnis. Validation of novel relative orientation and inertial sensor-to-segment alignment algorithms for estimating 3D hip joint angles. *Sensors*, 19(23):5143, 2019. doi: 10.3390/s19235143.

[79] Reiko Hara, Jennifer McGinley, Chris Briggs, Richard Baker, and Morgan Sangeux. Predicting the location of the hip joint centres, impact of age group and sex. *Scientific Reports*, 6:37707, 2016. doi: 10.1038/srep37707.

[80] J. Martin Bland and Douglas G. Altman. Measuring agreement in method comparison studies. *Statistical Methods in Medical Research*, 8(2):135–160, 1999. doi: 10.1177/096228029900800204.

[81] Giulia Pacini Panebianco, Maria Cristina Bisi, Rita Stagni, and Silvia Fantozzi. Analysis of the performance of 17 algorithms from a systematic review: Influence of sensor position, analysed variable and computational approach in gait timing estimation from IMU measurements. *Gait & Posture*, 66: 76–82, 2018. doi: 10.1016/j.gaitpost.2018.08.025.

[82] Brice Bouvier, Sonia Duprey, Laurent Claudon, Raphaël Dumas, and Adriana Savescu. Upper limb kinematics using inertial and magnetic sensors: Comparison of sensor-to-segment calibrations. *Sensors*, 15(8):18813–18833, 2015. doi: 10.3390/s150818813.

[83] Rachel V. Vitali and Noel C. Perkins. Determining anatomical frames via inertial motion capture: A survey of methods. *Journal of Biomechanics*, 106:109832, 2020. doi: 10.1016/j.jbiomech.2020.109832.

[84] Jeffrey M. Hausdorff. Gait variability: Methods, modeling and meaning. *Journal of NeuroEngineering and Rehabilitation*, 2(19):1–9, 2005. doi: 10.1186/1743-0003-2-19.

[85] Wolfgang Teufl, Markus Miezal, Bertram Taetz, Michael Fröhlich, and Gabriele Bleser. Validity of inertial sensor based 3D joint kinematics of static and dynamic sport and physiotherapy specific movements. *PloS ONE*, 14(2):e0213064, 2019. doi: 10.1371/journal.pone.0213064.

[86] Timothy McGrath and Leia Stirling. Body-worn IMU human skeletal pose estimation using a factor graph-based optimization framework. *Sensors*, 20(23):6887, 2020. doi: 10.3390/s20236887.

[87] Matthew P. Mavor, Gwyneth B. Ross, Allison L. Clouthier, Thomas Karakolis, and Ryan B. Graham. Validation of an IMU suit for military-based tasks. *Sensors*, 20(15):4280, 2020. doi: 10.3390/s20154280.

[88] Benedikt Fasel, Jörg Spörri, Pascal Schütz, Silvio Lorenzetti, and Kamiar Aminian. Validation of functional calibration and strap-down joint drift correction for computing 3D joint angles of knee, hip, and trunk in alpine skiing. *PloS ONE*, 12(7):e0181446, 2017. doi: 10.1371/journal.pone.0181446.

[89] Roy B. Davis III, Sylvia Õunpuu, Dennis Tyburski, and James R. Gage. A gait analysis data collection and reduction technique. *Human Movement Science*, 10:575 – 587, 1991. doi: 10.1016/0167-9457(91) 90046-Z.

[90] Veronica Cimolin and Manuela Galli. Summary measures for clinical gait analysis: A literature review. *Gait & Posture*, 39(4):1005–1010, 2014. doi: 10.1016/j.gaitpost.2014.02.001.

[91] Valentina Camomilla, Andrea Cereatti, Giuseppe Vannozzi, and Aurelio Cappozzo. An optimized protocol for hip joint centre determination using the functional method. *Journal of Biomechanics*, 39 (6):1096–1106, 2006. doi: 10.1016/j.jbiomech.2005.02.008.

[92] Scott L. Delp, J. Peter Loan, Melissa G. Hoy, Felix E. Zajac, Eric L. Topp, and Joseph M. Rosen. An interactive graphics-based model of the lower extremity to study orthopaedic surgical procedures. *IEEE Transactions on Biomedical Engineering*, 37(8):757–767, 1990. doi: 10.1109/10.102791.

[93] E.S. Grood and W.J. Suntay. A joint coordinate system for the clinical description of three-dimensional motions: Application to the knee. *Journal of Biomechanical Engineering*, 105(2):136–144, May 1983. doi: 10.1115/1.3138397.

[94] Danè Dabirrahmani and Michael Hogg. Modification of the Grood and Suntay joint coordinate system equations for knee joint flexion. *Medical Engineering & Physics*, 39:113 – 116, Jan 2017. doi: 10.1016/ j.medengphy.2016.10.006.

[95] Robert A. Siston, Aaron C. Daub, Nicholas J. Giori, Stuart B. Goodman, and Scott L. Delp. Evaluation of methods that locate the center of the ankle for computer-assisted total knee arthroplasty. *Clinical Orthopaedics and Related Research*, 439:129–135, 2005. doi: 10.1097/01.blo.0000170873.88306.56.

[96] National Center for Simulation in Rehabilitation Research. Opensim documentation - getting started with inverse kinematics. URL `https://simtk-confluence.stanford.edu/display/OpenSim/Getting+Started+with+Inverse+Kinematics#GettingStartedwithInverseKinematics-BestPracticesandTroubleshooting`. accessed on 2 Feb 2021.

[97] Elena Bergamini, Gabriele Ligorio, Aurora Summa, Giuseppe Vannozzi, Aurelio Cappozzo, and Angelo Sabatini. Estimating orientation using magnetic and inertial sensors and different sensor fusion approaches: Accuracy assessment in manual and locomotion tasks. *Sensors*, 14(10):18625–18649, Oct 2014. doi: 10.3390/s141018625.

[98] Kathryn E. Roach and Toni P. Miles. Normal hip and knee active range of motion: The relationship to age. *Physical Therapy*, 71(9):656—665, September 1991. doi: 10.1093/ptj/71.9.656.

[99] Geoffrey M. Verrall, John P. Slavotinek, Peter G. Barnes, Adrian Esterman, Roger D. Oakeshott, and Anthony J. Spriggins. Hip joint range of motion restriction precedes athletic chronic groin injury. *Journal of Science and Medicine in Sport*, 10(6):463 – 466, 2007. doi: 10.1016/j.jsams.2006.11.006.

[100] Xingda Qu and Joo Chuan Yeo. Effects of load carriage and fatigue on gait characteristics. *Journal of Biomechanics*, 44(7):1259–1263, 2011. doi: 10.1016/j.jbiomech.2011.02.016.

[101] Pietro Picerno. 25 years of lower limb joint kinematics by using inertial and magnetic sensors: A review of methodological approaches. *Gait & Posture*, 51:239–246, 2017. doi: 10.1016/j.gaitpost.2016.11.008.

[102] Paul DeVita and Tibor Hortobagyi. Age causes a redistribution of joint torques and powers during gait. *Journal of Applied Physiology*, 88(5):1804–1811, 2000. doi: 10.1152/jappl.2000.88.5.1804.

[103] Olumide Sofuwa, Alice Nieuwboer, Kaat Desloovere, Anne-Marie Willems, Fabienne Chavret, and Ilse Jonkers. Quantitative gait analysis in parkinson's disease: Comparison with a healthy control group. *Archives of Physical Medicine and Rehabilitation*, 86(5):1007–1013, 2005. doi: 10.1016/j.apmr.2004.08.012.

[104] AA Carmo, AFR Kleiner, PH Costa, and RML Barros. Three-dimensional kinematic analysis of upper and lower limb motion during gait of post-stroke patients. *Brazilian Journal of Medical and Biological Research*, 45(6):537–545, 2012. doi: 10.1590/s0100-879x2012007500051.

[105] Ive Weygers, Manon Kok, Henri De Vroey, Tommy Verbeerst, Mark Versteyhe, Hans Hallez, and Kurt Claeys. Drift-free inertial sensor-based joint kinematics for long-term arbitrary movements. *IEEE Sensors Journal*, 20(14):7969–7979, 2020. doi: 10.1109/JSEN.2020.2982459.

[106] Corina Nüesch, Elena Roos, Geert Pagenstert, and Annegret Mündermann. Measuring joint kinematics of treadmill walking and running: Comparison between an inertial sensor based system and a camera-based system. *Journal of Biomechanics*, 57:32–38, 2017. doi: 10.1016/j.jbiomech.2017.03.015.

[107] R Core Team. *R: A Language and Environment for Statistical Computing*. R Foundation for Statistical Computing, Vienna, Austria, 2013. URL `http://www.R-project.org/`.

[108] Douglas Bates, Martin Mächler, Ben Bolker, and Steve Walker. Fitting linear mixed-effects models using lme4. *Journal of Statistical Software, Articles*, 67(1):1–48, 2015. doi: 10.18637/jss.v067.i01.

[109] Alexandra Kuznetsova, Per Brockhoff, and Rune Christensen. lmertest package: Tests in linear mixed effects models. *Journal of Statistical Software, Articles*, 82(13):1–26, 2017. doi: 10.18637/jss.v082.i13.